DISCLAIMER:

This document does not meet the
current format guidelines of
the Graduate School at
The University of Texas at Austin.

It has been published for
informational use only.

The Dissertation Committee for Christopher Allen Johnson Blyton Certifies that this is the approved version of the following dissertation:

Proppant Transport in Complex Fracture Networks

Committee:

Mukul M. Sharma, Supervisor

Jon E. Olson

Steven L. Bryant

Larry W. Lake

Roger T. Bonnecaze

Proppant Transport in Complex Fracture Networks

by

Christopher Allen Johnson Blyton, B.E., M.S.E.

Dissertation

Presented to the Faculty of the Graduate School of

The University of Texas at Austin

in Partial Fulfillment

of the Requirements

for the Degree of

Doctor of Philosophy

The University of Texas at Austin

May 2016

Acknowledgements

I would like to thank my supervisor, Dr. Mukul M. Sharma, who has guided me through this research work. Several years ago, when I approached Dr. Sharma regarding research projects of potential mutual interest, I had little experience with numerical simulation beyond small assignments required by various classes. Despite this, he was willing to supervise my work in this area with full knowledge that there would likely be a considerable learning curve to overcome prior to real progress. I appreciate this and hope that along the way I may have picked up some of his insight, practicality and ability to make research truly engaging for an audience.

All committee members, Drs. Jon E. Olson, Steven L. Bryant, Larry W. Lake and Roger T. Bonnecaze, have contributed to this work through its thorough review and I would like to thank them for their time and effort in doing so. During my time in graduate school at The University of Texas at Austin, I have also taken several very useful classes taught by committee members. In particular, I would like to mention *Numerical Simulation of Reservoirs*, taught by Dr. Lake, which proved invaluable to this work. Earlier in my time in graduate school, I completed an MS thesis under the supervision of Dr. Bryant and I appreciate his contribution to my education.

Over the years, department staff including Jin Lee, Glen Baum, John Cassibry, Roger Terzian and Frankie Hart have made my graduate level studies easier through assistance with various issues from administrative to laboratory setup. Fellow students and friends have assisted with aspects of this work. In particular, Roman Shor has spent considerable time assisting with code compilation issues. Collaboration with Deepen Gala has enabled significant improvement of an existing simulator. I am grateful to both.

Friends from the program and outside of it have made living in Austin a great experience. I have experienced much more with Ale Carlos than I would have otherwise, her energy for life is incomparable. Involvement with a running group has kept me fit enough for a few races. My family, at home in Australia, have always been supportive and I thank them for visiting me here several times.

Financial support for this work has been provided through the Joint Industry Project on *Hydraulic Fracturing and Sand Control* coordinated by Dr. Sharma. The Texas Advanced Computing Center (TACC) at The University of Texas at Austin provided HPC resources that have contributed to the research results reported within this dissertation. URL: http://www.tacc.utexas.edu.

Proppant Transport in Complex Fracture Networks

Christopher Allen Johnson Blyton, Ph.D.

The University of Texas at Austin, 2016

Supervisor: Mukul M. Sharma

Current hydraulic fracturing practice in unconventional resource development typically involves multiple fracturing stages, each consisting of the simultaneous creation of several fractures from a horizontal well. A large mass of proppant, often millions of pounds per well, is injected with the fluid to provide post-closure conductivity. Despite the large quantity of proppant used and its critical importance to well productivity, simple models are often applied to determine its placement in fractures. Propped or effective fracture lengths indicated by modeling may be 100 to 300% larger than the lengths inferred from production data. A common assumption is that the average proppant velocity due to pressure driven flow is equal to the average carrier fluid velocity, while the settling velocity calculation uses Stokes' law. To more accurately determine the placement of proppant in a fracture, it is necessary to rigorously account for many effects not included in the above assumptions.

In this study, the motion of particles flowing with a fluid between fracture walls has been simulated using a coupled computational fluid dynamics and discrete element method (CFD-DEM) that rigorously accounts for both aspects of the problem. These simulations determine individual particle trajectories as particle to particle and particle to wall collisions occur and include the effect of fluid flow. The results show that the proppant concentration and the ratio of proppant diameter to fracture width govern the

relative velocity of proppant and fluid. Proppant settling velocity has been examined for small fracture widths to delineate the effect of several independent variables, including concentration. Simulations demonstrate that larger concentration increases the average settling velocity, in apparent contrast with the available literature, which indicates that increased concentration reduces settling velocity. However, the observed increase in settling velocity is due to the absence of displacement driven counter current fluid flow. In a hydraulic fracture, counter current fluid flow is expected but its magnitude may be different to that produced by the advance of a step change concentration front, as occurs in experiments reported in the available literature. This demonstrates that proppant settling in a hydraulic fracture is more complex than usually considered.

A proppant transport model, developed from the results of the direct numerical simulations and existing correlations for particle settling velocity, has been incorporated into a fully three-dimensional hydraulic fracturing simulator. This simulator couples fracture geomechanics with fluid flow and proppant transport considerations to enable the fracture geometry and proppant distribution to be determined rigorously. Injection rate, which is an engineering fracture design parameter, has been varied to show the effect on proppant placement. This allows for an understanding of the relative importance of different aspects of proppant transport and optimization of the treatment to a particular application.

The presence of natural fractures in unconventional reservoirs can significantly contribute to well productivity. As proppant is transported along a hydraulic fracture, the presence of a dilated natural fracture forms a fluid accepting branch and may result in proppant entry. The proportion of proppant transported into a branch at steady state has been determined using the CFD-DEM approach and is presented via a dimensionless 'particle transport coefficient' through normalization by the proportion of fluid flowing

into the branch. Reynolds number at the inlet, branch aperture and the angle of orientation between the main slot and branch, particle size and concentration each affect the transport coefficient. A very different physical process, which controls particle transport into a branch under certain conditions, is the formation of a stable particle bridge preventing subsequent particle transport into the branch. This phenomenon was observed in several simulation cases.

The complete set of equations for a three-dimensional formulation of rectangular displacement discontinuity elements has been used to determine the width distribution of a hydraulic fracture and dilated natural fracture. The widths have been determined for several combinations of stress anisotropy, net pressure, hydraulic fracture height and length. The effect of the length, height and orientation of the natural fracture and the elastic moduli of the rock have also been examined. Of the cases examined, many show that natural fracture dilation does not occur. Further, of those cases where dilation is apparent, the proppant transport efficiency corresponding to the natural fracture width is significantly less than one and in many cases zero due to size exclusion. The natural fracture location and orientation do not significantly affect its width, while its length and the elastic moduli of the rock substantially change its width.

Table of Contents

List of Tables

List of Figures

Chapter 1: Introduction

The proppant mass included in hydraulic fracture treatments has increased substantially as well stimulation practices have been optimized for unconventional resource development. The increased fracturing activity associated with an increase in production of tight oil and shale gas, primarily in the U.S., can benefit from an improved understanding of proppant transport.

1.1 Context of the Study

1.1.1 Recent U.S. Unconventional Oil and Gas Production

Production of tight oil and shale gas has increased dramatically in the U.S. over the past decade. The U.S. Energy Information Administration (EIA) has collated state administrative production data and provided estimates based on each shale play, shown in Figure 1.1.

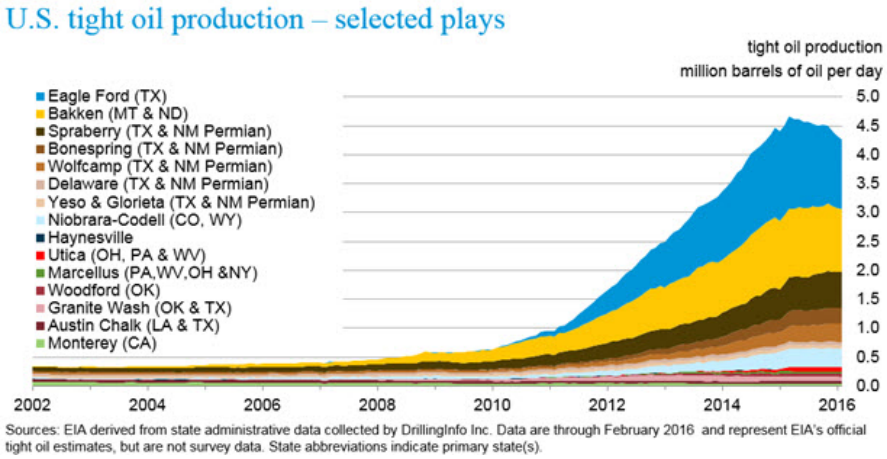

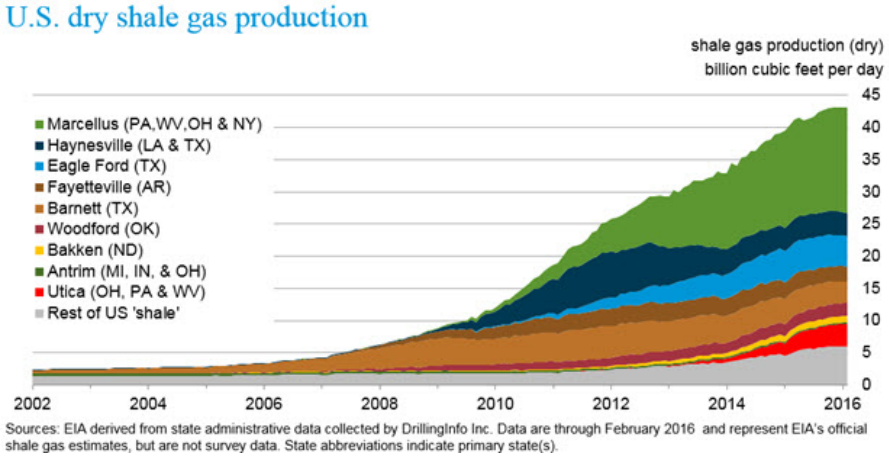

Figure 1.1. Top: U.S. tight oil production from 2002 to 2016. Bottom: U.S. shale gas production from 2002 to 2016. (EIA Shale in the United States http://www.eia.gov/energy_in_brief/article/shale_in_the_united_states.cfm#tightoil)

Recent decreases in the oil price have resulted in a decrease in production of tight oil from the peak observed in 2015, through to the latest data shown in Figure 1.1, which is for 2016. However, at approximately 4.25 million barrels per day, more than 45% of the current U.S. total daily crude oil production of 9.179 million barrels per day (as of January 2016) is supplied by tight oil (EIA Crude Oil Production Data http://www.eia.gov/dnav/pet/pet_crd_crpdn_adc_mbblpd_m.htm). Similarly, of the 91.135 billion cubic feet of natural gas produced per day in the U.S. (as of January 2016), 43 billion is produced from shale (EIA Natural Gas Production Data http://www.eia.gov/dnav/ng/ng_prod_sum_a_EPG0_FGW_mmcfpd_m.htm), which represents a 47% share.

1.1.2 Global Unconventional Oil and Gas Resources

While recent production growth of tight oil and shale gas has been the largest in the U.S., there are significant unconventional oil and gas resources across the world. The EIA has compiled estimates of unproved technically recoverable shale gas and tight oil

resources (EIA Technically Recoverable Shale Oil and Shale Gas Resources https://www.eia.gov/analysis/studies/worldshalegas/archive/2013/pdf/fullreport_2013.pdf). While such estimates are always subject to considerable revision, they indicate that China, Argentina, Algeria, U.S. and Canada have the largest resources of shale gas, of 1115.2, 801.5, 706.9, 622.5 and 572.9 trillion cubic feet respectively. The U.S., Russia, China, Argentina and Libya are believed to have the most significant shale oil resources at 78.2, 74.6, 32.2, 27.0 and 26.1 billion barrels respectively. Clearly, the resource base is significant and there is potential for increased production worldwide when and where economic conditions prove favorable.

1.2 KEY TECHNOLOGIES

One significant characteristic of formations holding unconventional oil and gas is very low permeability. As a result, a large area of wellbore contact with the reservoir must be created in order to attain economic production rates. This objective is achieved through horizontal drilling and multi-stage hydraulic fracturing. Horizontal drilling involves controlled diversion of the drillstring from its initial vertical trajectory by means of a motor or rotary steerable system. The inclination of the wellbore is increased over the build section to target and then follow the productive interval for, typically, thousands of feet. A fluid mixture is subsequently pumped at high pressure into the wellbore, with the goal of initiating and extending several hydraulic fractures simultaneously during each stage. To provide conductivity of the created fractures, proppant is added at various concentrations over the course of injection, which typically lasts for tens of minutes. Firstly, a volume of proppant-free fluid in injected to initiate the hydraulic fractures and ensure sufficient width for subsequent entry of proppant. Secondly, proppant-laden fluid

at steadily increasing concentration is injected. Finally, more proppant-free fluid is injected to displace remaining proppant from the wellbore.

1.3 Hydraulic Fracturing Techniques

Hydraulic fracturing has been used to increase well productivity for many decades. However, the fluid and proppant volumes and types used have changed significantly over time, as treatments have been adapted and optimized for particular reservoirs. Data compiled by IHS Energy and analyzed by Gallegos and Varela (2015) show that between 1953 and 1999 the average fluid volume used in horizontal gas wells was 6,026 barrels. For the period 2000 to 2010, the average for this well type was 71,654 barrels, an increase of more than ten fold. There was a smaller increase in the average fluid volume used to hydraulically fracture horizontal oil wells, nonetheless more than twice the volume has been applied, on average, in the more recent period. Figure 1.2 shows hydraulic fracturing records from Gallegos and Varela (2015).

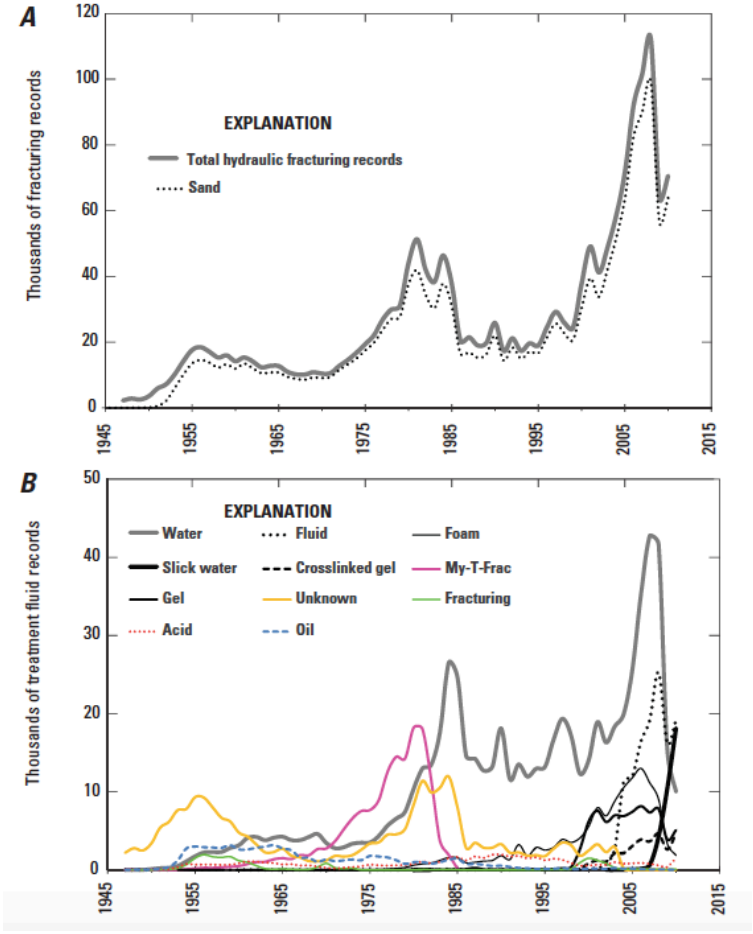

Figure 1.2. Top: Total hydraulic fracturing records and use of sand reported. Bottom: Fluid type reported for each hydraulic fracturing record. (Gallegos and Varela (2015)).

Gallegos and Varela (2015) report than proppant has been used in 84% of hydraulic fracturing treatments between 1947 and 2010, determined from the data presented in the top pane of Figure 1.2. Of the treatments where proppant was included, 99% of these used sand with only 1% consisting of engineered materials such as ceramic or resin coated materials. Over the course of optimizing hydraulic fracturing treatments for unconventional reservoirs, the average mass of proppant used has increased. One example, provided by Beckwith (2011), is applications in the Bakken formation, where it

was reported that 300,000lbs per well was typically used in the early 2000s and that 3 to 5 million pounds per well were used at the time of writing. As an approximate, fluid and proppant volumes have increased together.

The bottom pane of Figure 1.2 presents a breakdown of the fluid type used, with water being the most common until recently, when slickwater and 'fluid' became the most common. Obviously 'fluid' is a poor description, however it is assumed that this category covers primarily water based fluids. Slickwater is also a water-based fluid, though one with friction reducers added to reduce the pressure loss incurred during turbulent flow down the wellbore. These three categories do not make mention of additives that significantly increase viscosity, such as cross-linked gels, and may reasonably be described as low viscosity Newtonian fluids.

1.4 Research Objectives

The primary objective of this research is the accurate quantification of proppant transport in simple and complex hydraulic fracture networks. Numerical simulation has been used to determine transport at the granular scale and full fracture scale. Specifically, the work consists of:

i. Application of a three-dimensional, coupled computational fluid dynamics and discrete element (CFD-DEM) code to quantify the relative phase velocities for pressure driven particle transport.

ii. Use of the CFD-DEM code to study particle settling.

iii. Improvement of an existing single planar hydraulic fracturing simulator, UTEFRAC-3D, which couples slurry flow and solid mechanics considerations, by inclusion of the results from step i).

iv. Application of the CFD-DEM code to determine particle transport in a branched fracture.

v. Development of a multiple fracture simulator using a three-dimensional displacement discontinuity formulation. Subsequent examination of natural fracture dilation using the simulator. Discussion of results with respect to those found in step iv).

1.5 Structure of the Dissertation

The work has been divided into the following chapters:

Chapter 2 presents the formulation of a three-dimensional CFD-DEM code used in much of this research. The equations solved in each representation of the system are provided. Further, a discussion of simulation considerations including dynamic mesh refinement is provided.

Chapter 3 covers application of the CFD-DEM code to the problem of pressure driven particle transport with fluid flow between parallel walls. Results are presented as a function of the independent variables of interest.

Chapter 4 details use of the CFD-DEM code to study particle settling in a fluid between parallel walls. The results are normalized as appropriate and the dependency upon the independent variables of interest examined.

Chapter 5 includes the improvement of UTEFRAC-3D to include a new model for proppant transport, based on the results of Chapter 3. The impact of this model upon propped fracture lengths, when compared to existing models, is determined.

Chapter 6 examines particle transport into a branched fracture by means of the CFD-DEM code. The results are presented by means of the dimensionless transport efficiency, which depends upon many independent variables.

Chapter 7 presents the development of a three-dimensional multiple fracture model. The equations solved and application to the dilation of a natural fracture are included, as are the results as a function of the independent variables considered.

Chapter 8 draws conclusions from the work and provides directions for future study.

Chapter 2: Coupled Computational Fluid Dynamics and Discrete Element Method Simulation

A completely general theoretical analysis of the motion of solid bodies in a fluid consists of determining the velocity and pressure across the fluid domain by solution of conservation of mass and momentum for the fluid and calculating the forces and torques exerted by the fluid on the solid bodies and their resultant motion. The boundary conditions applied to the fluid domain and the constitutive equation used for the fluid rheology allows any arbitrary fluid flow to be analyzed, including those in laminar and turbulent flow regimes. Multiple solid bodies can be included, with the contact forces arising due to collisions between them and any solid domain boundaries calculated rigorously. As a result, these methods can be applied to a broad range of practical applications.

2.1 INTRODUCTION

The general approach may be solved numerically by several different methods. One of the earliest applications of this type of simulation was that of Hu *et al*. (1992), where a finite-element solution was employed. The simplified problem solved was that of the motion of two cylinders settling in a quiescent incompressible Newtonian fluid in a rectangular domain. Despite the simplification of the physical system to two dimensions, Hu *et al*. (1992) successfully qualitatively reproduced the scenario of 'drafting, kissing and tumbling' observed in physical experiments concerning spheres falling through a fluid conducted by Fortes *et al*. (1987).

Feng *et al*. (1994) applied the approach of Hu *et al*. (1992) to the motion of solid cylinders in two dimensional slot Poiseuille flow. They determined the equilibrium

position of the cylinders in the slot, where the sum of lateral forces is zero. They also demonstrated that the equilibrium position is shifted closer to the wall for a larger Reynolds number. Yang *et al*. (2005) determined the lift force, slip velocities and equilibrium position of a solid spherical particle in tube Poiseuille flow. They validated their solution by comparison to the migration trajectories recorded in physical experiments conducted by Karnis *et al*. (1966). The work demonstrated that the equilibrium position in the slot moves closer to the wall with increasing Reynolds number, qualitatively in agreement with the results of the two dimensional simulations of Feng *et al*. (1994), despite the different geometry examined.

It should be noted that all the studies included above solve the fluid flow field around each individual solid body, a numerically expensive process. Adopting the terminology used by Shirgaonkar *et al*. (2009) in the development of a method to calculate the force imposed by a fluid on an immersed body, this method is 'fully resolved'. Previous work, such as that of Hu *et al*. (1992), refers to this approach as 'direct numerical simulation' (DNS). However, this work includes turbulence modeling which introduces a context where DNS is used to specify solution of the flow field at a scale sufficient to capture the smallest fluctuations, which is not undertaken in this research. As a result the term 'fully resolved' is used in lieu of 'direct'. The fully resolved approach is distinctly different to the commonly used 'unresolved' approach in that the latter utilizes drag (and other) force models for the solid-fluid coupling, where in the former it arises from the solution. The unresolved approach is suitable for larger systems of particles where the domain geometry is on a much larger scale than the particles. Recent work using reduced order force models has investigated particle transport with turbulent fluid flow and been applied to bed load transport and saltation. See Duran *et al*. (2012) and Maurin *et al*. (2015) for examples of this approach. Since this research

includes simulation cases where the particle diameter is only slightly smaller than the wall spacing, resolution of the fluid flow around particles is necessary for accurate calculation of particle transport. As such, a fully resolved computational fluid dynamics and discrete element method (CFD-DEM) approach has been applied.

The open source CFD library OpenFoam was used to solve the time-varying governing equations for the fluid in a Cartesian coordinate system using a finite-volume spatial discretization approach on an Eulerian grid, see Weller *et al*. (1998). The particle motion was solved using a Lagrangian approach with LIGGGHTs, an open source DEM software package, see Kloss *et al*. (2012). The coupling between the CFD and DEM solutions was achieved through the fluid force acting on each particle, through a method proposed by Shirgaonkar *et al*. (2009) and implemented by Hager *et al*. (2011) using an immersed boundary approach. The details of this approach are presented below.

2.2 CFD SIMULATION

OpenFoam (Open Source Field Operation and Manipulation) was used to solve the velocity and pressure of the fluid across the domain. The mass and momentum conservation equations, respectively, which govern the flow of any incompressible fluid are:

$$\nabla \cdot \mathbf{u}_f = 0 \qquad (2.1)$$

and

$$\rho_f \frac{\partial \mathbf{u}_f}{\partial t} + \rho_f \mathbf{u}_f \cdot \nabla \mathbf{u}_f = -\nabla \mathrm{p} + \nabla \cdot \boldsymbol{\tau} \qquad (2.2)$$

where $\boldsymbol{u}_f$ is the fluid velocity vector (m/s), ρ_f is the fluid density (kg/m^3), t is time (s), p is the pressure (Pa) and $\boldsymbol{\tau}$ is the deviatoric stress tensor (Pa). It should be noted that the momentum conservation equation, (2.2), does not include the body force term from which the hydrostatic pressure gradient arises. The hydrostatic pressure gradient, in turn,

produces the buoyancy force on an immersed particle. While the body force term is omitted, the fluid-particle force that arises as a result is included rigorously in the DEM simulation, as discussed below. The deviatoric stress tensor is given by:

$$\tau = \eta \mathbf{e} \quad (2.3)$$

where ***e*** is the strain rate tensor (1/s), given by:

$$\mathbf{e} = \nabla \mathbf{u}_f + \left(\nabla \mathbf{u}_f\right)^T \quad (2.4)$$

and η is the dynamic viscosity (Pa-s), which for a Newtonian fluid is independent of ***e*** and assumed constant for this work. Fluids with different rheological properties, following Newtonian and shear thinning Power-law behavior, were included in the study. For a Power-law fluid η is not constant but defined by the function:

$$\eta = \eta_c \gamma^n \quad (2.5)$$

where η_c is the fluid consistency index (Pa-s^n), γ is the shear rate (1/s) and n is the fluid behavior index. For a shear-dominated flow, such as the applications studied in this work, the shear rate is a function of II_e, the second invariant of the rate of strain tensor given by:

$$\gamma = \sqrt{II_e} \quad (2.6)$$

$$II_e = \frac{1}{2}\left[tr\left(\mathbf{e}^2\right) - \left(tr\left(\mathbf{e}\right)\right)^2\right] \quad (2.7)$$

In the case of turbulent flow, the above conservation equations can be used for the resolution of fluid flow down to the smallest length scale through the use of very fine spatial discretization, the DNS approach, see texts such as Versteeg and Malalasekera (1998). However, the DNS of turbulent flow structures is computationally very expensive and impractical for this application where considerable numerical expense is already incurred. There are many models available for modeling turbulent flow, allowing for sub grid scale physics to be effectively captured, see texts such as Wilcox (1997). One of the most widely used models is the k – ε model, which is used in this work and requires the

solution of two additional conservation equations for turbulence kinetic energy and its dissipation, respectively, see Jones and Launder (1972).

2.3 DEM SIMULATION

Cundall and Strack (1979) originally introduced the discrete element method (DEM). Significant theoretical developments related to contact physics and advances in parallel computing have been made since the original work. The latter allows for efficient application to large-scale engineering problems, while the former is reviewed comprehensively in Zhu *et al*. (2007) and will not be included in detail in this work.

The DEM procedure involves determining the sum of forces and torques on each individual particle in the system. Subsequently, integration of Newton's second law of motion twice with respect to time allows for solution of the velocity and position of the particle. The equations of motion may be expressed as follows:

$$m_i \frac{\mathrm{d}^2 \mathbf{x}_i}{\mathrm{d}t^2} = \mathbf{F}_{itotal} \quad (2.8)$$

$$I_i \frac{\mathrm{d}^2 \boldsymbol{\theta}_i}{\mathrm{d}t^2} = \mathbf{M}_{itotal} \quad (2.9)$$

where m_i is the mass of particle i (kg), $\boldsymbol{x}_i = (x_i, y_i, z_i)$ is the coordinates its center of gravity (m) and $\boldsymbol{F}_{i\,total}$ is the total force acting upon the particle (N). Considering rotation, I_i is the moment of inertia (kg-m^2), $\boldsymbol{\theta}_i$ is the angular position (rad) and $\boldsymbol{M}_i$ total is the total moment acting on the particle (N-m). In the case of a granular only simulation, the total force acting on a particle is due to contact forces, due to both particle to particle collisions and particle to wall collisions. In this particular application, in addition to the contact forces calculated, the only non-contact force present is that exerted by the fluid surrounding the particles.

Particles are modeled as elastically isotropic homogeneous spheres, neglecting surface roughness. Hertz (1882) developed a non-linear force-displacement law for the normal component of contact between such spheres, while later Mindlin and Derieswicz (1953) provided a solution for the tangential component. The DEM code used, LIGGGHTs ('LAMMPS Improved for General Granular and Granular Heat Transfer Simulations') is based on LAMMPS ('Large Atomic and Molecular Massively Parallel Simulator'). This code includes an implementation of these models with sliding assumed to occur if the tangential component of the inter-particle force exceeds the Coulomb frictional force. Combining normal and tangential components, the inter-particle force can be written as:

$$\mathbf{F}_{ij} = \left(k_n \delta \mathbf{n}_{ij} - \gamma_n \Delta u_p \mathbf{n}_{ij}\right) + \left(k_t \delta \mathbf{t}_{ij} - \gamma_t \Delta u_p \mathbf{t}_{ij}\right) \quad (2.10)$$

where $\boldsymbol{F}_{ij}$ is the inter-particle force (N), k is the spring coefficient (N/m), δ is the overlap (m), γ is the damping coefficient (N-s/m) and Δu_p is the relative speed (m/s). Symbols $\boldsymbol{n}_{ij}$ and $\boldsymbol{t}_{ij}$ are used to denote unit vectors in the normal and tangential directions considering a Langrangian coordinate system. The subscripts n and t are used to denote the normal and tangential directions. Finally, subscript ij is applied to the interaction of particle i with particle j. The same law applies for collisions between particles and walls, where the wall is assumed to have an infinite mass and size. For more detail on the calculation of the spring and damping coefficients from the particle material properties, see Kloss *et al*. (2012).

There are additional non-contact forces applied to each particle as a result of the body force acting (gravity) and due to immersion in a fluid, either static or dynamic. These forces are discussed in the following section.

2.4 COUPLING CFD AND DEM SIMULATIONS

Determining the buoyant force on a particle immersed in a compressible fluid requires integration of the hydrostatic pressure distribution across its surface. As noted above, the form of the Navier-Stokes equation applied does not produce a hydrostatic pressure distribution. However, for an incompressible fluid, the buoyant force is given simply by the weight of displaced fluid. The gravitational force on a particle is its weight. The difference between these two forces is rigorously given by:

$$\mathbf{F}_{Archimedes} = \frac{1}{6}\pi d^3 \left(\rho_p - \rho_f\right)\mathbf{g} \quad (2.11)$$

where $\boldsymbol{F}_{Archimedes}$ is the difference in forces from gravity and buoyancy (N). In addition to this force, which arises in both static and dynamic fluids, fluid motion leads to an additional pressure and viscous force applied to each particle.

Shirgaonkar *et al*. (2009) proposed an algorithm to solve the motion of rigid or flexible bodies immersed in a fluid. This algorithm treats the solid phase as subject to the governing equations of the fluid phase with an additional constraint imposed, similarly to the approach adopted by Patankar *et al*. (2000) for rigid bodies. The complete rigid body constraint is:

$$\mathbf{u}_{p\,point} = \mathbf{u}_p + \omega \times \mathbf{r} \quad (2.12)$$

where $\boldsymbol{u}_{p\ point}$ (m/s) is the velocity of a point on the particle at position vector $\boldsymbol{r}$ (m) with respect to the particle centroid, while $\boldsymbol{u}_p$ (m/s) and ω (rad/s) are the translational and angular velocities of the particle, respectively. The interface conditions between the fluid and each solid particle are given by:

$$\mathbf{u}_f = \mathbf{u}_p \ \text{ and } \ tr_{\Gamma_s} = \sigma \cdot \mathbf{n} \ \text{ on } \ \Gamma_s \quad (2.13)$$

where tr (Pa) is the traction, σ (Pa) is the stress tensor and $\boldsymbol{n}$ is the outward normal unit vector to the surface Γ_s. The stress tensor for an elastic fluid is:

$$\sigma = -p\mathbf{I} + \tau \quad (2.14)$$

There is a surface Γ_s for each particle in the entire domain Ω (fluid and solid particles), with Ω_s denoting the solid domain, which is shown shaded grey in Figure 2.1.

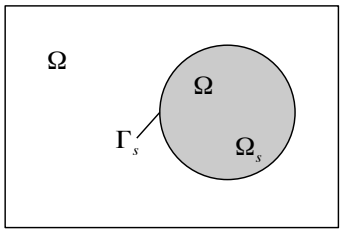

Figure 2.1. CFD-DEM simulation domain, adapted from Hager *et al*. (2012).

The second interface condition (provided in (2.13)), combined with the rigid body constraint, which requires the deformation rate tensor to be zero in each solid domain, produces a stress field in the solid domain. The implementation of Hager *et al*. (2011) uses a volumetric integration of the stress field across each discrete particle to determine the fluid to particle force applied. This is as follows:

$$\int_{\Omega_s} \alpha(x,y,z,t)\,dV = \int_{\Omega} \alpha(x,y,z,t)\,\xi(x,y,z,t)\,dV \quad (2.15)$$

where the function ξ is a scalar marker function that takes the value of unity across the solid domain and zero in the fluid domain. Hence:

$$\xi = \begin{cases} 1 & \text{if } (x,y,z) \in \Omega_s \\ 0 & \text{else} \end{cases} \quad (2.16)$$

Finally:

$$\alpha = -\nabla p + \nu\nabla^2 \mathbf{u}_{p\,point} \quad (2.17)$$

The specific implementation used in this work uses a simplification of the rigid body constraint, which neglects the rotational component:

$$\mathbf{u}_{p\,point} = \mathbf{u}_p \quad (2.18)$$

This limits application of the method to cases where particle rotation is not crucial to the accuracy of the calculations. For example, the case of dilute concentration at sufficiently large Reynolds number to observe lateral migration to the Segre and Silberberg equilibrium position may not be captured accurately. However, particle rotation is assumed to be less important to the application of interest to this study, those of cases of non-dilute concentration.

2.5 Implementation and Simulation Considerations

2.5.1 Method Implementation

The implementation of the method is detailed in Goniva *et al*. (2011) and Hager *et al*. (2011). It consists of the following steps:

i. Calculation of the particle positions and velocities by the DEM solver.

ii. An initial solution of the velocity and pressure of the fluid across the entire domain by the CFD solver, neglecting the presence of solid particles.

iii. Imposition of the particle velocities from the DEM solver upon portions of the domain covered by the solids in the CFD representation of the system.

iv. Calculation of the fluid force upon each particle.

v. Correction of the initial fluid velocity and pressure solution by the CFD solver to satisfy a 'divergence free' condition (the divergence free condition is a consequence of the conservation of mass for an incompressible fluid, see (2.1)).

vi. Repeat from step i).

The two codes, OpenFoam and LIGGGHTs, are run independently with a particular coupling interval at which time the required data exchange is completed.

2.5.2 Simulation Considerations

2.5.2.1 Time Step for DEM Simulation

The time step required for numerical stability of the DEM solver is smaller than that of the CFD solver. There are two criteria necessary for DEM simulation stability, use of a time step smaller than both the Raleigh and Hertz times. Both criteria are functions of particle size and elastic moduli, while the former also depends upon density and the latter includes a relative velocity term. Precisely how much smaller than the two criteria the time step needs to be for stability is a function of coordination number, see O'Sullivan and Bray (2004). Due to the nature of the applications of interest, *a priori* knowledge of the particle positions and hence the coordination number is both unavailable and dynamic and as such a conservative value of 0.2 has been used in this work. For the majority of simulations, with a particle diameter of 0.0004m, the DEM time step used was $3x10^{-8}$s. Simulations with larger particle sizes of 0.00055, 0.0007 and 0.001m diameter enabled use of a larger time steps, $4x10^{-8}$, $5x10^{-8}$ and $7x10^{-8}$s, respectively. The simulations of particles with larger elastic moduli required a smaller time step of $2x10^{-8}$s.

2.5.2.2 Time Step for CFD Simulation

The Courant number, a measure of the magnitude of the local fluid velocity relative to the size of the grid-block for a particular time step, is the relevant criteria for CFD simulation stability. Considering a fluid flow only simulation, a Courant number limit of approximately 0.5 is common practice. In the case of the coupled simulation approach used in this research, a coupling interval is required. This determines a particular number of smaller DEM time steps taken before a larger CFD time step is made. In the absence of a rigorous method of selecting an appropriate coupling interval, a

trial and error approach has been adopted. A result of the smaller DEM time step and the necessary coupling interval selected is that the CFD time step used produces a Courant number much smaller than 0.5.

Due to the considerable numerical expense of the method and constraints upon run times, a large coupling interval is necessary to produce sufficient simulation data for non-dilute cases. For example, simulation of a system with many particles using a coupling interval of only one or two would not reach steady state before the run time limit set for the hardware used. The run time required for several simulation cases is included in Appendix A. Confirmation that the accuracy of the calculations is maintained with a large coupling interval was investigated by means of less computationally expensive single particle cases in slot Poiseuille flow. The smallest slot width considered in the study presented in Chapters 3, 4 and 6 requires a particle diameter to slot width ratio of 0.95. This geometry was used to make two comparisons of the calculated translational velocity of a single particle in the center of a slot at Reynolds numbers of one and one thousand, which place the flow in the creeping and laminar flow regimes, respectively. The results determined from comparing simulations using coupling intervals of one and 20 were found to be in agreement to ~2%. For the majority of simulations presented in Chapter 3, the coupling interval used was 20. The exception is cases with a particle diameter to slot width ratio of 0.1, for which a coupling interval of 40 was used. This is by necessity given the relatively large number of particles simulated in these cases, but acceptable given the smaller fluid and particle velocities apparent. The expense of a relatively large domain used in the simulation cases examined in Chapter 4 and the large amount of simulation data required for analysis of the cases presented in Chapter 6 required use of a coupling interval of 100 for the majority of cases. The exception is the simulation cases at larger Reynolds number presented in Chapter 6, where a smaller

coupling interval was necessary. A coupling interval of 60 was used for a Reynolds number of 4000 and a coupling interval of 30 or 40 (as necessary for stability) for the Reynolds number of 8000 cases.

The coupled approach is explicit in that step iii) uses the particle velocities from the previous time step to complete the fluid to particle force on each particle and solution of the fluid flow field, steps iv) and v). The approach has been successfully verified by comparison to analytical solutions, as discussed in Chapters 3 and 4.

2.5.2.3 CFD Simulation Mesh

Domains of relatively simple geometry, rectangular boxes, have been used for the studies presented in Chapter 3 and Chapter 4. For the study of particle transport in slot Poiseuille flow, the x and z coordinate directions (both not cross-slot directions) as defined in Chapter 3, use a less refined original static mesh used when compared to the cross-slot direction. The width of the grid-blocks used is half the particle diameter. For slot Poiseuille flow, across the slot there is zero pressure gradient but large velocity gradients, especially close to the walls. For cases with a larger slot width and hence smaller velocity gradients, a mesh of grid-blocks of width half the particle diameter has been used, the same as used in the other two coordinate directions. For cases with a smaller slot width, grid-blocks with a width less than half a particle diameter have been used to adequately resolve the velocity profile. In addition to these considerations for the original static mesh, dynamic mesh refinement has been used for greater resolution of particles and the fluid flow around them, while using less computational resources in regions of the domain where a fine mesh is not required. Two refinement steps, each of which split a grid-block in two in each of the three Cartesian coordinate directions has been employed. The same grid has been used for the particle settling study presented in

Chapter 4, with the exception of the grid blocks used in the *x* coordinate direction, where three grid blocks per particle diameter was used in place of two. The grid used for the study of particle transport in a branched slot, presented in Chapter 6, uses a more sophisticated grid, which is discussed in detail in that chapter.

2.6 LUBRICATION FORCES

The force upon each particle resulting from the surrounding fluid flow and the forces arising from particle to particle and particle to wall collisions are all captured by the method as detailed above. However, simulation approaches such as this may produce an error in the calculation of the force exerted by the fluid on a particle just prior to a collision. This is a result of the thin film of fluid between particles and the grid used for the CFD simulation. One approach to improving the accuracy of these simulations, without refining the grid, is to use a lubrication force correction for particles within a particular proximity. Lambert *et al*. (2013) implemented such a solution two particles in squeezing motion, finding that it was not required for shearing motion. Since the dominant motion of particles in this work is with flow parallel to walls, resulting in shearing motion, a lubrication correction has not been applied in this work. It is interesting to note that Lambert *et al*. (2013) conducted simulations over a range of volumetric concentration from 7.8% to 24%, with and without lubrication corrections applied, finding that the results showed no appreciable difference. A similar concentration range for multi-particle simulations has been considered in this work, 5% to 25%, suggesting that neglecting a lubrication correction is acceptable.

Chapter 3: Pressure Driven Flow of Non-Dilute Suspensions in Slots

The simulation approach detailed in Chapter 2 has been used to complete a comprehensive study of the transport of spherical solid particles with pressure driven fluid flow in a slot. The average velocity of particles has been determined relative to the average velocity of fluid.

3.1 INTRODUCTION

In general, transport of solid particles with fluid flow results from the macroscopic pressure gradient driving flow and the density difference between the particles and the surrounding fluid, in the case of non-neutrally buoyant particles. The fully developed velocity profile across a slot that arises from the pressure driven laminar flow of a Newtonian fluid between two parallel plates follows a parabolic expression, termed slot Poiseuille flow in this research. Flow in a tube of circular cross-section is referred to as tube Poiseuille flow to denote the difference in geometry. When particles are introduced into slot or tube Poiseuille flows, many similarities exist in the motion observed and as such the literature pertaining to both is reviewed here. To the authors' knowledge, there is not a reduced order model available for the cross-slot average velocity of particles transported in slot Poiseuille flow at non-dilute concentration and moderate Reynolds number, which is a range of considerable practical interest in engineering applications. However, a solution to the cross-slot average particle velocity can be constructed from *i)* the particle concentration distribution and *ii)* the particle velocity in the direction of flow as a function of position in the slot. A solution of this type clearly requires knowledge of both these functions.

Segre and Silberberg (1962) published early research into the particle concentration distribution in tube Poiseuille flow. They were the first to observe particles accumulating at a lateral position of approximately 0.6 tube radii. This is the result of equilibrium of lateral forces at this position, often termed the 'tubular pinch' effect. Their experiments were conducted at dilute concentrations (the maximum tested was approximately one percent by volume) and at a maximum Reynolds number of 520. The tubular pinch effect was most clearly defined when the Reynolds number was less than 30. At larger Reynolds number, a wider distribution of particles was observed. The authors also note that while the results were shown to be concentration independent within the dilute range examined, concentration dependence would be expected to arise with increased concentration. For example, when there is a larger concentration present, it is simply not possible for all particles to be accommodated at 0.6 tube radii.

Altobelli *et al*. (1991) conducted physical experiments investigating large concentrations of solid spheres, up to 39% by volume fraction, transported by tube Poiseuille flow. Nuclear resonance magnetic imaging was used to determine the particle concentration and fluid velocity distribution. The experiments exhibited a greater concentration of particles at the center of the tube and a 'blunted' fluid velocity profile was observed, whereby the maximum fluid velocity relative to the cross-slot average was reduced with increasing particle concentration. Koh *et al*. (1994) conducted experiments examining the fluid velocity profile and particle concentration distribution in a rectangular slot using laser-Doppler anemometry, considering particle concentrations up to 30% at very small Reynolds number. Similarly to Altobelli *et al*. (1991), a greater particle concentration at the center of the slot and a blunted fluid velocity profile was evident. A significant observation made was that when comparing experiments at a particle concentration of 30% to that of 10%, there was a sharp reduction in the

maximum particle velocity. A significant slip velocity exists between the particles and the fluid, which increases with increasing particle concentration.

Ho and Leal (1974) presented a theoretical study of lateral migration effects for a single solid sphere in slot Poiseuille flow, which produce the concentration distribution recorded by Segre and Silberberg (1962). They also include a solution to the particle velocity in the direction of flow as a function of position in the slot. Their solution used an approximate treatment, the method of reflections. The authors note that the solution presented is accurate when the particle is not located in close proximity to a wall. When the slot width is not significantly larger than the particle diameter, a particle is necessarily in close proximity to a wall. In this case it follows that the method is less accurate. Another restriction of the method is that it applies only at small Reynolds number. With these restrictions, they determined the equilibrium position in the slot, which was in agreement with the experimental results of Segre and Silberberg (1962), despite the difference in geometry between a slot and a tube. The translational and rotational slip velocities were also provided, which demonstrates that the particle velocity lags the undisturbed fluid velocity at all positions in the slot. It should be noted that this slip velocity is not the same as the concentration effect reported by Koh *et al*. (1994), as it is apparent for a single particle in slot Poiseuille flow. That is, there are two separate mechanisms by which particles are transported more slowly than the surrounding fluid. Ho and Leal (1974) also demonstrated that the center of the slot is an unstable equilibrium position.

Staben *et al*. (2003) utilized a boundary-integral algorithm to examine the particle velocity in the direction of flow as a function of position in the slot and wall spacing for a single neutrally buoyant sphere in slot Poiseuille flow. Jones (2004) applied a Fourier transform technique to the same problem. The approaches of both Staben *et al*. (2003)

and Jones (2004) provide highly accurate results for larger particle diameter to slot width ratios and for a particle in close proximity to the wall. As such, these solutions overcome the limitations of the solution provided by Ho and Leal (1974). Staben *et al*. (2003) and Jones (2004) demonstrate that the particle velocity is always lower than the local undisturbed fluid velocity and is a function of wall spacing.

As noted above, the cross-slot average velocity for particle transport by slot Poiseuille flow can be determined from *i)* the particle concentration distribution and *ii)* the particle velocity in the direction of flow as a function of position in the slot. Physical experiments have demonstrated the existence of equilibrium positions at which dilute concentrations of particles accumulate and non-uniform concentration distributions in the case of large particle concentration. These studies present data for tubes across a wide range of Reynolds numbers and for slots at small Reynolds number. The single particle velocity in the direction of flow has been determined theoretically and shown to lag the local undisturbed fluid velocity at all positions in the slot and wall spacing. Physical experiments have shown that the particle velocity in slot Poiseuille flow exhibits strong concentration dependence. The particle velocity results for both a single particle and concentrated flows were obtained at very small Reynolds number.

Data on both the particle concentration distribution and particle velocity in the direction of flow for slot Poiseuille flow is unavailable for moderate Reynolds number and non-dilute concentration. This study presents the cross-slot average particle velocity for spheres in slot Poiseuille flow as determined by numerical simulation. Similarly to the general approach pioneered by Hu *et al*. (1992), the motion of solid bodies in a fluid are calculated via the forces exerted by the surrounding fluid, for which the velocity and pressure across the fluid domain is determined from conservation of mass and momentum for the fluid, subject to appropriate boundary and initial conditions. Cases with different

fluid rheology and at different Reynolds number have been examined. An extension of slot Poiseuille flow to include the effect of fluid loss through porous walls has been included. Further, simulations with different solid particle material properties and size have been conducted.

3.2 VERIFICATION

3.2.1 Verification Overview

Verification of the method for the application of interest has been completed by comparison to the results of Staben *et al*. (2003) for the translational velocity of a single particle in low Reynolds number slot Poiseuille flow. Staben *et al*. (2003) provided results for a single particle transported at several different positions in slots of various widths. Considering the symmetry of the flow field about the centerline, the two limits of particle position in the slot, next to a wall and at the center, have been used for comparison. Since the Reynolds number is low, lateral migration is negligible and the simplification made in imposing the particle velocity on the CFD representation of the system without inclusion of the rotational component is acceptable. Of course, limiting comparison to single particle cases does not enable verification of the macroscopic properties of a multi-particle system, such as the concentration distribution. However, it does confirm that the resolution of the fluid force upon each particle is sufficiently accurate, including any effect of the numerical parameters used.

3.2.2 Simulation Domain and Boundary Conditions

Due to the considerable numerical expense of the method and constraints upon run times, a small domain is necessary. The simulation domain used is shown in Figure 3.1.

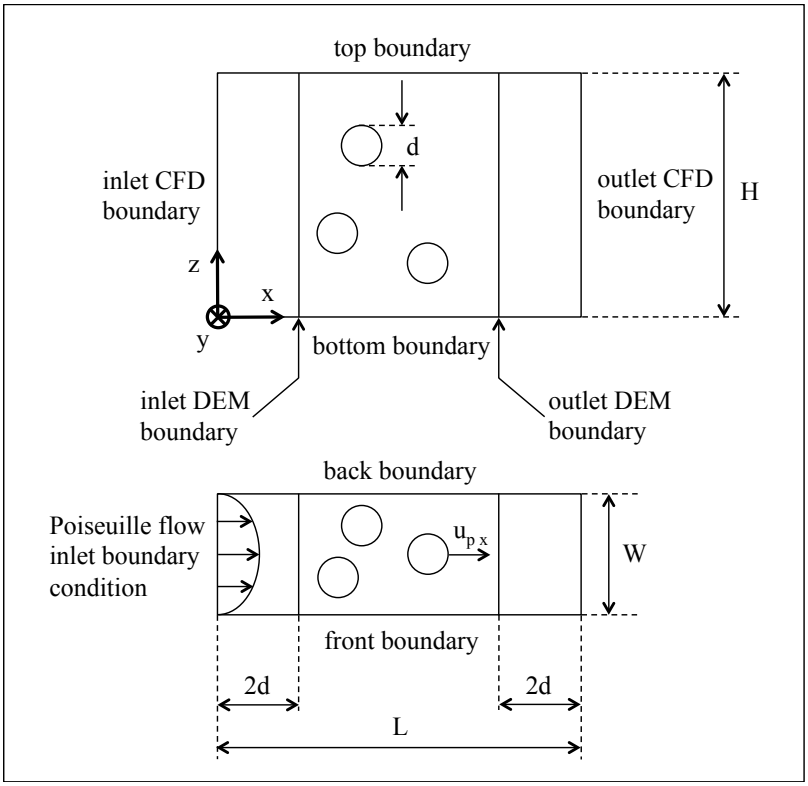

Figure 3.1. Simulation domain.

The CFD and DEM domains share the same boundaries in the *y* and *z* coordinate directions. In the *x* coordinate direction the DEM domain boundaries are two particle diameters inside the CFD domain boundaries. This was found to reduce a small 'step' in translational velocity evident as a particle leaves the *outlet* of the DEM domain and re-enters the *inlet*. This numerical artifact is a consequence of the boundary conditions imposed, which themselves are necessary to produce the required flow field. At the low Reynolds number of the simulations used for verification, the particle was found to reach a steady state before leaving the domain once and this concern was not an issue. However, for larger Reynolds number cases, particles recirculate before reaching steady state. Nonetheless, this effect was shown to be negligible in terms of particle transport. A

detailed discussion of the numerical artifact and domain size is provided in Appendix B. The length of the domain, L, is 9 particle diameters, d. The width, W, takes a particular value to produce the required particle diameter to slot width ratio for each case. The height, H, is 6 particle diameters. As a result, the range in volume of the DEM domain is ~$31.6d^3$ to $300d^3$, corresponding to d/W equal to 0.95 and 0.1 respectively. Only 3 particles provide a volumetric concentration of 5% in the smallest domain, whereas 143 particles are required to provide 25% concentration in the largest domain.

The boundary conditions applied to the CFD domain are as follows:

At the CFD *inlet*: fully developed slot Poiseuille flow

$$u_{fx}(y) = u_{fx\,max}\left\{1-\left[\frac{|y-B|}{B}\right]^{1/n+1}\right\} \qquad u_{fy}=0 \qquad u_{fz}=0 \qquad \frac{\partial p}{\partial x}=0 \tag{3.1}$$

where u_{fx}, u_{fy} and u_{fz} (m/s) are the scalar components of the fluid velocity vector and B is half the slot width. Since the solution provided by Staben *et al*. (2003) is for a Newtonian fluid, the verification simulations also use a Newtonian fluid, for which the fluid behavior index, n, is one. The expression for u_{fx} has been obtained analytically from conservation of momentum considerations for a power-law fluid. This is necessary for extension of the research to cases of shear thinning fluids, which are included in this work.

At the CFD *outlet*: constant pressure

$$\frac{\partial u_{fx}}{\partial x}=0 \qquad \frac{\partial u_{fy}}{\partial x}=0 \qquad \frac{\partial u_{fz}}{\partial x}=0 \qquad p=0 \tag{3.2}$$

At both the CFD *front* and *back* boundaries: no slip condition

$$u_{fx}=0 \qquad u_{fy}=0 \qquad u_{fz}=0 \qquad \frac{\partial p}{\partial x}=0 \tag{3.3}$$

At the CFD *top* and *bottom* boundaries: cyclic pairing

$$u_{fx}\big|_{z=0}=u_{fx}\big|_{z=H} \qquad u_{fy}\big|_{z=0}=u_{fy}\big|_{z=H} \qquad u_{fz}\big|_{z=0}=u_{fz}\big|_{z=H} \qquad p\big|_{z=0}=p\big|_{z=H} \tag{3.4}$$

The cyclic pairing used for the top and bottom boundaries represents an infinitely tall slot.

The boundary conditions applied to the DEM domain are as follows:

At the DEM *inlet* and *outlet* boundaries: periodic pairing, each particle that leaves the domain at the DEM *outlet* re-enters the domain at the DEM *inlet* with the same $\boldsymbol{u}_p$.

At the DEM *front* and *back* boundaries: walls

At the DEM *top* and *bottom* boundaries: periodic pairing

3.2.3 Verification Simulation Results

Two simulations, one at each of the limits of particle position in a slot, were run for each of ten different particle diameter to slot width ratios. The appropriate Reynolds number for slot Poiseuille flow of a power-law fluid, based on a characteristic length of the hydraulic diameter, is:

$$Re_s = \frac{(2W)^n \left[\langle u_{fx} \rangle (1-c)\right]^{2-n} \rho_f}{8^{n-1}\left(\frac{3n+1}{4n}\right)^n \eta_c} \qquad (3.5)$$

where Re_s is the slot flow Reynolds number, c is the concentration and η_c (Pa-s^n) is the fluid consistency index. The factor of (1-c) appears as a result of using the same fluid velocity boundary condition at the inlet for simulation cases at several different concentrations, with the product of $\langle u_{fx} \rangle$(1-c) termed the modified average fluid velocity (m/s). The above expression is considerably simplified in the case of a Newtonian fluid. Staben *et al*. (2003) presented results for low Reynolds number, although the precise range of validity for their results was not provided. The verification simulations have been conducted at a Reynolds number of one. To significantly reduce the transient portion of the simulation, the initial conditions for the fluid domain were that of fully

developed slot Poiseuille flow. This involves application of the following velocity distribution across the domain:

$$u_{fx}(y) = u_{fxmax}\left\{1-\left[\frac{|y-B|}{B}\right]^{1/n+1}\right\} \qquad u_{fy}=0 \qquad u_{fz}=0 \tag{3.6}$$

The analytically derived pressure distribution is also applied across the domain as an initial condition:

$$p(x) = \frac{\eta_c L}{B\rho_f}\left[\frac{(1/n+1)u_{fxmax}}{B}\right]^n\left(1-\frac{x}{L}\right)+p\big|_{x=L} \tag{3.7}$$

In each of the twenty cases, a single particle was initialized at an *x* location half a particle diameter inside the DEM *inlet* boundary and with an *x* component of particle velocity equal to the average fluid velocity. The *y* position specified was half a particle diameter from the CFD *front* boundary for the case of a particle at the wall and at the center of the slot for the other limit of position cases. Finally, the *z* position was at the center of the height of the domain. Both the *y* and *z* components of velocity were zero. By initializing the simulation with a particle at the average fluid velocity, a transient is observed whereby the particle accelerates or decelerates to a steady state. This allowed for confirmation that the simulation had been run for a sufficient period of time to reach steady state. The velocity transients for a particle in the center and at the wall of the slot, for a case with the diameter to slot width ratio of 0.1, is shown in Figure 3.2. Note that the simulation data presented is the result of two separate simulations, each with a single particle present.

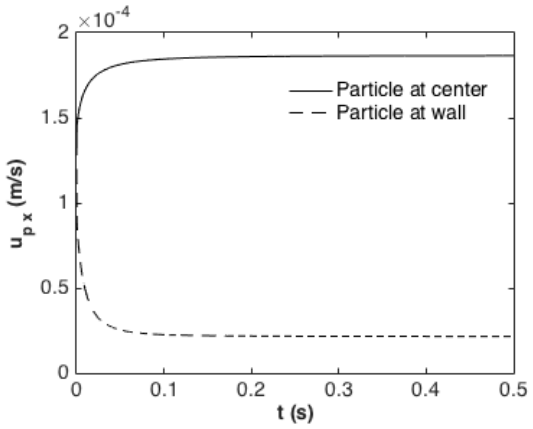

Figure 3.2. Particle velocity transient for a particle positioned at the wall and center of the slot.

For each case, the steady state velocity was determined and is shown in Figure 3.3, normalized by the modified average fluid velocity.

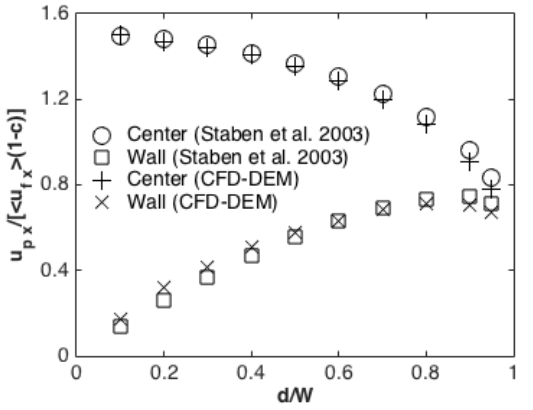

Figure 3.3. CFD-DEM verification results compared to those from Staben *et al*. (2003).

The expression for $u_{f\,x}(y)$ provided in (3.6) demonstrates that the fully developed fluid velocity profile across a slot for a Newtonian fluid in the laminar flow regime results in a parabolic distribution. The maximum fluid velocity is 3/2 times greater than the average fluid velocity. For d/W equal to 0.1, a particle in the middle of a slot translates at very slightly less than the local fluid velocity, 3/2 times the average, from the

results of Staben *et al*. (2003). As a result, the particle velocity normalized by the average fluid velocity presented in Figure 3.3 is approximately 3/2 in this case.

Across the range of *d*/*W* and particle position in the slot, the comparison between the CFD-DEM results and those from Staben *et al*. (2003) demonstrates good agreement. This indicates the suitability of this method to the problem of solid spheres transported by slot Poiseuille flow. It should also be noted that across the range of particle diameter to slot width ratio and across the two limits of particle position in the slot, the results of both Staben *et al*. (2003) and this study show that particles always translate at less than the local fluid velocity.

3.3 Single Particle Slot Poiseuille Flow Simulations

3.3.1 Single Particle Slot Poiseulle Flow Simulation Overview

The following results were obtained from simulations with the same domain and boundary and initial condition types used for the verification simulations. The Reynolds number was larger in all cases due to larger average fluid velocities, though still within the laminar flow regime region. Since the average fluid velocities were much greater, using the same small domain resulted in the particle making many passes through the domain for a simulation of the same duration. This enables the average particle velocity to be calculated via a counter placed in the middle of the domain in the *y*-*z* plane. The average particle velocity is determined from:

$$\left\langle u_{px} \right\rangle = \frac{\dot{m}}{cA\rho_p} \quad (3.8)$$

where $\dot{m}$ (kg/s) is the particle mass rate, A (m^2) is the area of the counter, WxH, and ρ_p (kg/m^3) is the particle density. The particle mass rate was determined from the gradient of

a linear trend fitted to the cumulative mass versus time simulation data via a process of least squares regression.

For a single particle moving in the center of the slot, the cross-slot location used for all simulation results presented in this section, there is no lateral migration and zero rotation. This position in the slot is one of unstable equilibrium. Since there is zero rotation, the simplification made by imposing the particle velocity on the CFD representation of the system without the rotational component is not a concern. The effect of Reynolds number, fluid rheology, particle size and fluid loss through the walls were examined. Particle density and modulus may affect the results of multiple particle systems where particle to particle and particle to wall collisions occur. However, for the single particle cases at steady state examined here, these variables do not alter the results in any way.

3.3.2 Single Particle Slot Poiseuille Flow Simulation Results

Simulations have been completed to determine the effect of Reynolds number, Newtonian fluid viscosity, particle size and fluid loss through the walls. The results of these simulations are shown in Figure 3.4.

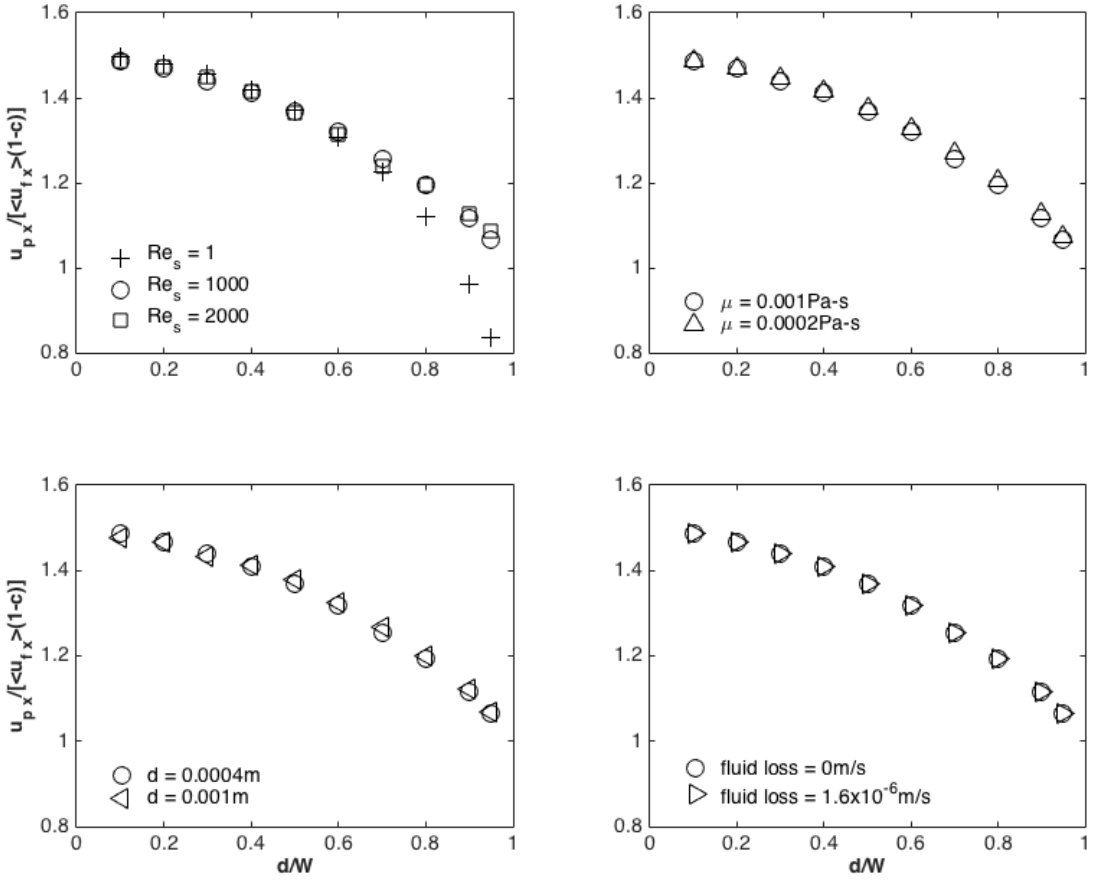

Figure 3.4. Particle velocity normalized by the modified average fluid velocity versus particle diameter to slot width ratio. Top left: Reynolds number. Top right: Newtonian fluid viscosity. Bottom left: Particle size. Bottom right: Fluid loss through the walls.

The top left pane of Figure 3.4 shows the results of simulations at different Reynolds numbers. Larger average fluid velocities were used for the larger Reynolds number cases, with all other variables remaining constant. The normalized particle translation velocity for cases with Reynolds number of 1000 and 2000 are very similar, though they diverge from the validated results at a Reynolds number of one. There is an inertial effect evident for large ratios of particle diameter to slot width. The normalized particle translation velocity is larger when the Reynolds number is larger. This shows that

the wall retardation effect on the slip velocity is reduced with increasing Reynolds number. Nonetheless, the particle velocity remains smaller than the local fluid velocity.

Simulation results with different Newtonian fluid viscosity, 0.0002Pa-s and 0.001Pa-s, are shown in the top right pane of Figure 3.4. All of these simulations were conducted at a Reynolds number of 1000, requiring smaller average fluid velocities to be specified for the smaller Newtonian viscosity cases. These two sets of results are virtually identical, indicating that the Newtonian viscosity does not change the solution when cast in dimensionless terms. That is, the appropriate dimensionless group for the problem is the Reynolds number. The bottom left pane of Figure 3.4 shows the results of simulations with a particle diameter of 0.0004m and 0.001m. To make comparisons at the same ratio of particle diameter to slot width, the domain is proportionally larger in each coordinate direction. With a larger characteristic length, a smaller average fluid velocity was specified in each case to produce a Reynolds number of 1000. As for the comparison at a different Newtonian fluid viscosity, the comparison for a different particle diameter produces very similar results. This further confirms that the Reynolds number can be used to describe the problem in dimensionless terms.

The bottom right pane of Figure 3.4 examines the effect of fluid loss through the slot walls upon a particle in the middle of the slot. The simulations with fluid loss are identical to those without fluid loss except for the modification of the CFD boundary conditions applied on the *front* and *back*. A constant fluid velocity leaving the domain perpendicular to the face has been applied as follows:

$$u_{fy}\Big|_{y=0} = -a \qquad u_{fy}\Big|_{y=W} = a \tag{3.9}$$

An analytical solution to slot Poiseuille flow in the presence of fluid loss through porous walls was provided by Berman (1953). Since the flow field remains symmetric in

the presence of fluid loss perpendicular to the walls, a particle placed at the center does not have a net lateral drag force applied by the fluid flow. Thus, the only effect expected would be due to the fluid deceleration along the slot. This is a very small effect for the fluid loss velocities apparent in most engineering applications, where the average fluid velocity is significantly greater than the fluid loss velocity. In this particular case, the average fluid velocity in the *x* coordinate direction is 0.125m/s, more than four orders of magnitude greater than the fluid loss velocity. If a particle is placed off center, it will experience an additional lateral drag force that would change the equilibrium position in the slot. Asmolov (1999) has determined the existence of several transport regimes for dilute particle transport in slot Poiseuille flow with fluid loss through the walls. This particular problem has not been examined in this study since particle rotation, critical to the equilibrium position of a single particle in Poiseuille flow, has not been included in the implementation used.

The results shown in Figure 3.4 demonstrate that the Reynolds number is the appropriate dimensionless group to reduce the problem of a single particle translating at the center of a slot in Poiseuille flow. A set of simulations has been conducted with a shear-thinning power-law fluid with η_c of 0.1Pa-s and *n* of 0.2, with the results shown in Figure 3.5.

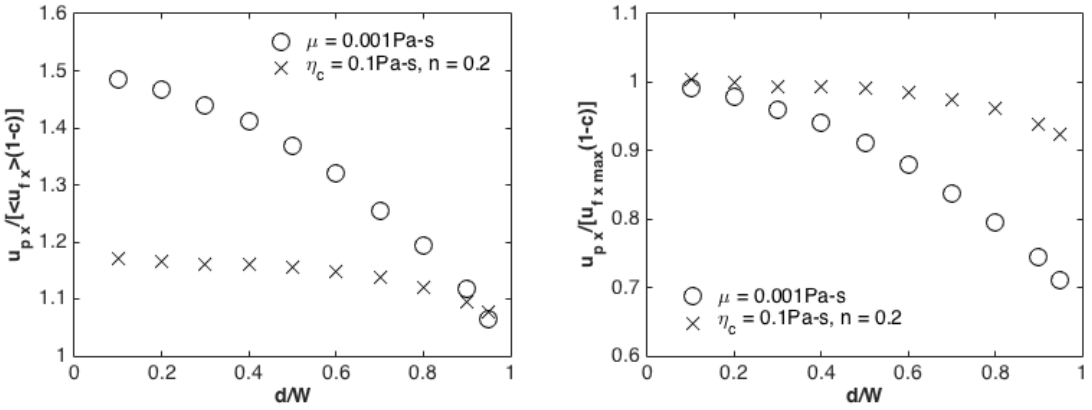

Figure 3.5. Left: Particle velocity normalized by the modified average fluid velocity versus particle diameter to slot width ratio. Right: Particle velocity normalized by the modified maximum fluid velocity versus particle diameter to slot width ratio.

Examining the results shown in Figure 3.5, there is a very different trend apparent between the simulation results with Newtonian and shear-thinning power-law fluids. It should be noted that the relationship between the maximum and average fluid velocity for a power-law fluid in Poiseille flow in the absence of particles is given by:

$$u_{fxmax} = \frac{1/n+2}{1/n+1}\left\langle u_{fx} \right\rangle \qquad (3.10)$$

The function of n takes a value of $3/2$ for a Newtonian fluid and 1.17 for a power-law fluid with n of 0.2, the case studied here. Examining the left pane of Figure 3.5 and comparing cases with a particle diameter to slot width ratio of 0.1, the particle translates at close to the local fluid velocity, which is the maximum fluid velocity, for both the Newtonian and shear-thinning power-law fluids. The right pane, using a particle translation velocity normalized by the maximum fluid velocity, shows this most clearly as the values for both fluid types is very close to one. The much more 'blunt' fluid velocity profile across the slot for the power-law fluid exposes more of the particle to a surrounding fluid velocity close to the maximum fluid velocity. The effect of this is

apparent when examining larger particle diameter to slot width ratios, where is a greater degree of wall retardation evident for the Newtonian fluid compared to the shear-thinning power law fluid.

3.4 MULTIPLE-PARTICLE UNIFORM FLOW SIMULATIONS

3.4.1 Multiple-Particle Uniform Flow Simulation Overview

The following results were obtained from simulations in which particles move in a domain with uniform fluid flow and which represents infinite extent. The effect of two variables, concentration and Reynolds number, upon particle transport velocity is examined. These simulations allow particle motion with fluid flow to be studied in the absence of the complexity of slot Poiseuille flow. This is achieved with cyclic boundary conditions in both the *y* and *z* directions and a uniform velocity applied at the CFD *inlet*. The domain size is the same as shown in Figure 3.1, with *W* equal to 6 times the particle diameter and the same as *H*.

3.4.2 Multiple-Particle Uniform Flow Boundary Conditions

The boundary conditions applied to the CFD domain are as follows:

At the CFD *inlet*: uniform flow

$$u_{fx}(y) = b \qquad u_{fy} = 0 \qquad u_{fz} = 0 \qquad \frac{\partial p}{\partial x} = 0 \tag{3.11}$$

where *b* (m/s) is a constant.

At the CFD *outlet*: constant pressure

$$\frac{\partial u_{fx}}{\partial x} = 0 \qquad \frac{\partial u_{fy}}{\partial x} = 0 \qquad \frac{\partial u_{fz}}{\partial x} = 0 \qquad p = 0 \tag{3.12}$$

At both the CFD *front* and *back* boundaries: cyclic pairing

$$u_{fx}\Big|_{y=0} = u_{fx}\Big|_{y=W} \qquad u_{fy}\Big|_{y=0} = u_{fy}\Big|_{y=W} \qquad u_{fz}\Big|_{y=0} = u_{fz}\Big|_{y=W} \qquad p\Big|_{y=0} = p\Big|_{y=W} \tag{3.13}$$

At the CFD *top* and *bottom* boundaries: cyclic pairing

$$u_{fx}\big|_{z=0} = u_{fx}\big|_{z=H} \qquad u_{fy}\big|_{z=0} = u_{fy}\big|_{z=H} \qquad u_{fz}\big|_{z=0} = u_{fz}\big|_{z=H} \qquad p\big|_{z=0} = p\big|_{z=H} \tag{3.14}$$

The boundary conditions applied to the DEM domain are as follows:

At the DEM *inlet* and *outlet* boundaries: periodic pairing, each particle that leaves the domain at the DEM *outlet* re-enters the domain at the DEM *inlet* with the same $\boldsymbol{u}_p$.

At the DEM *front* and *back* boundaries: periodic pairing

At the DEM *top* and *bottom* boundaries: periodic pairing

3.4.3 Multiple-Particle Uniform Flow Results

Simulations cases were run at six different values of concentration, between dilute and 25%, each at four values of particle Reynolds number, Re_p. The particle Reynolds number uses a characteristic length of the particle diameter and for a Newtonian fluid is given by:

$$Re_p = \frac{d\langle u_{fx}\rangle(1-c)\rho_f}{\mu} \tag{3.15}$$

The largest value of Re_p considered was 4000, which places these cases in the turbulent flow regime region. The k – ε model was used in these cases. Similarly to the approach taken for the verification and single particle slot Poiseuille flow simulations, the initial conditions for the fluid domain were those of fully developed flow to reduce the transient portion of the simulation. In this case, the solution for fully developed flow was found numerically by running a CFD only simulation for a sufficient period of time to ensure the flow field solution had reached steady state. The DEM domain was initially seeded with a particular number of particles to provide the selected concentration. The initial particle positions were determined with each coordinate value selected from a uniform distribution bounded by limits one particle radius inside the DEM simulation domain boundary. The positions drawn from the uniform distribution were rejected if

they produced overlapping particle positions. This eliminated large and non-physical repulsion velocities upon initialization. The DEM boundary conditions used produce a constant concentration for the duration of the simulation. The initial particle velocities were set to the uniform fluid velocity at the inlet, *b*. The average particle velocity was determined by use of a counter in the *y*-*z* plane as detailed above for the single particle simulations.

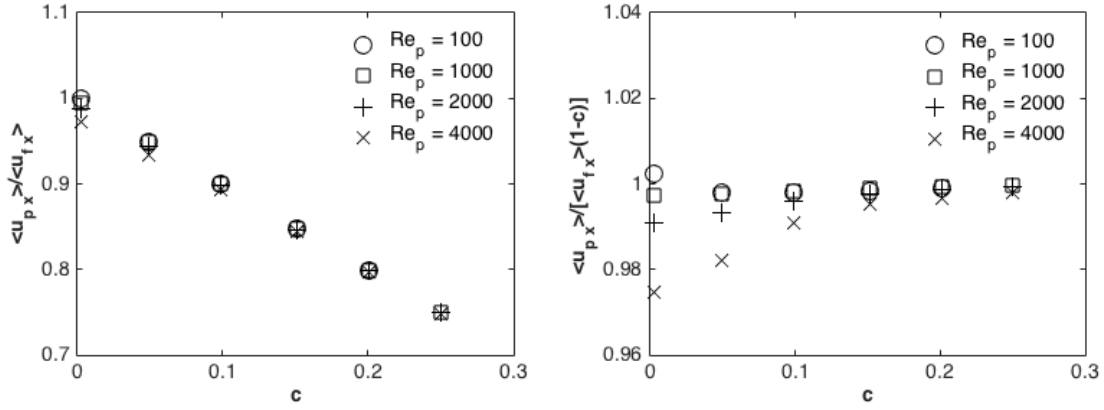

Figure 3.6. Left: Average particle velocity normalized by the average fluid velocity versus concentration. Right: Average particle velocity normalized by the modified average fluid velocity versus concentration.

The simulation results shown in the left pane of Figure 3.6 show that the average particle velocity, normalized by the average fluid velocity, is reduced with increasing concentration. The trend is very close to linear, which is evident when the same results are normalized by the modified average fluid velocity and once more plotted against concentration. This is shown in the right pane of Figure 3.6, and demonstrates that the average particle translation velocity is very close to the modified average fluid velocity. By definition, the average fluid phase velocity is larger than the modified average fluid velocity by a factor of 1/(1-*c*). Another way of stating this result is that there is a significant slip velocity between the particles and the fluid, which increases linearly with

increasing concentration. There is a minor effect attributable to Reynolds number for small concentration and large Reynolds number, whereby the normalized average particle velocity is reduced slightly. The results of Koch and Hill (2001) for particles in uniform flow demonstrate that concentration is the primary variable upon which the drag force depends. They note that Reynolds number has a second order effect. These effects upon the drag force exerted on each particle in uniform flow produce the slip velocities observed in this work. Remarkably, the results may be well described by a very simple relation:

$$\frac{\langle u_{px} \rangle}{\langle u_{fx} \rangle (1-c)} = 1 \qquad (3.16)$$

3.5 Analytical Slot Poiseuille Flow Model

3.5.1 Analytical Slot Poiseuille Flow Model Overview

The results of Staben *et al*. (2003) show that a single particle translates at less than the local fluid velocity for all positions in a slot of all particle diameter to slot width ratio considered. The single particle results contained in this research demonstrate that while the slip velocity is reduced with increasing Reynolds number for a single particle at the center of a slot, the particle nonetheless translates at less than the local fluid velocity. The simulation results examining particles in uniform flow showed that particle transport occurs at the modified average velocity of the fluid. Equivalently, the particle translation velocity is reduced through multiplication by a factor of (1-*c*) times the fluid phase velocity. Clearly this factor is always less than one and the particles translate at a velocity less than the fluid, that is, there is a slip velocity apparent even in the absence of the complexity of slot Poiseuille flow.

The analytical solution presented here neglects the wall retardation effect on the slip velocity as demonstrated by Staben *et al*. and in this work for a single particle at larger Reynolds number. The particle translation velocity dependency upon concentration determined in the simulations of uniform flow has been implemented as the only mechanism causing a slip velocity. Isolation of this single effect for the particle slip velocity allows a detailed examination of the average transport properties. The accuracy of this approximate solution is greater for smaller particle diameter to slot width ratios, since the wall retardation effect upon the slip velocity is reduced in the case of greater wall spacing.

3.5.2 Analytical Slot Poiseuille Flow Model Derivation

The cross-slot average particle velocity in slot Poiseuille flow can be constructed from *i)* the particle concentration distribution and *ii)* the particle velocity in the direction of flow as a function of position in the slot. By definition and with no simplification, this is given by:

$$\left\langle u_{px} \right\rangle = \frac{\int_{d/2}^{B} c(y) u_{px}(y) dy}{\int_{d/2}^{B} c(y) dy} \qquad (3.17)$$

from symmetry and using the physical limit for a particle center at one particle radius from the slot wall as the lower limit of the integral. While the definition is provided without simplification, the two functions needed for solution by this approach do require reduced forms.

The first function required is the concentration distribution, *c(y)*. The exact form is unknown and to the authors' knowledge unavailable in the existing literature. However, a limit can be placed upon its maximum value and its form can be

approximated from simple considerations as follows. An upper limit can be determined from random close packing considerations, which results in a value of approximately 63% by volume, see Song *et al*. (2008). This limit is subsequently denoted as c_{max}. The simplest approximation for the form of *c(y)* is a uniform distribution. However, contrary to this simplifying assumption, concentration peaks at positions of equilibrium of lateral forces are expected to form. Specific values at these peaks and their location for slot Poiseuille flow are not available in the literature for the Reynolds number and concentration range of interest. Nonetheless, across the full spectrum of Reynolds number, the centerline is an unstable equilibrium position due to zero net lateral migration force. Since the centerline is always a position where a concentration peak is expected, a triangular distribution provides the simplest deviation from a uniform distribution and has been used for comparison purposes. For the average concentration, *g*, the concentration distributions are given by:

$$c(y) = g \qquad (3.18)$$

which is a uniform distribution, and:

$$c(y) = \frac{2g}{B - d/2}\left(y - \frac{d}{2}\right) \qquad (3.19)$$

which is a triangular distribution, both of which are valid between the half slot limits of:

$$\frac{d}{2} \le c(y) \le B \qquad (3.20)$$

The second function required is the particle translation velocity as a function of position in the slot, $u_{p\,x}(y)$. The particle velocity relative to the average fluid velocity determined from the uniform flow simulations is assumed to hold for slot Poiseuille flow on a local basis. That is, an extension is made by assuming that the velocity of particles at a particular position in the slot can be determined from the local fluid velocity and the

local concentration. This assumption leads to the following expression for particles flowing in a Newtonian fluid across a range of concentration:

$$u_{px}(y) = u_{fxmax}\left(-\frac{y^2}{B^2} + \frac{2y}{B}\right)\left[1 - c(y)\right] \tag{3.21}$$

which is a result of the velocity profile for fully developed slot Poiseuille flow, derived from conservation of momentum considerations. This form is valid over the half slot limits provided above. It should be noted that this assumes that the fluid velocity profile remains unchanged by the addition of particles. Experimental research by Altobelli *et al*. (1991) and Koh *et al*. (1999) shows that the velocity profile is 'blunted' by the presence of particles, a secondary effect which is neglected in this analysis.

3.5.3 Analytical Slot Poiseuille Flow Model Results

The integral used to determine the average cross-slot particle velocity, provided above, has been evaluated for two example cases, that of uniform and triangular particle concentration distribution. The results of the integrals are:

$$\left\langle u_{px} \right\rangle = u_{fxmax}(1-g)\frac{\frac{2B}{3} + \frac{d^3}{24B^2} - \frac{d^2}{4B}}{B - d/2} \tag{3.22}$$

for a uniform concentration distribution and:

$$\left\langle u_{px} \right\rangle = u_{fxmax}\frac{\left(1 + \frac{gd}{B-d/2}\right)\left(\frac{5B^2}{12} - \frac{dB}{3} - \frac{d^4}{192B^2} + \frac{d^3}{24B}\right) - \frac{2g}{B-d/2}\left(\frac{3B^3}{10} - \frac{5dB^2}{24} - \frac{3d^5}{640B^2} + \frac{d^4}{96B}\right)}{\frac{B^2}{2} - \frac{dB}{2} + \frac{d^2}{8}}$$

(3.23)

for a triangular concentration distribution. Examining the limits of a very large wall spacing relative to the particle diameter, $d << W$, the average particle velocity equals a factor of (1-c) multiplied by average fluid velocity for a uniform particle concentration.

The two expressions provided above have been evaluated for a range of d/w and g, normalized by the average fluid velocity, with the results presented in Figure 3.7. The largest value of g considered is 30%, which leads to a peak in concentration at the center of the slot for the triangular distribution of 60%, which is less than but close to the upper limit c_{max}.

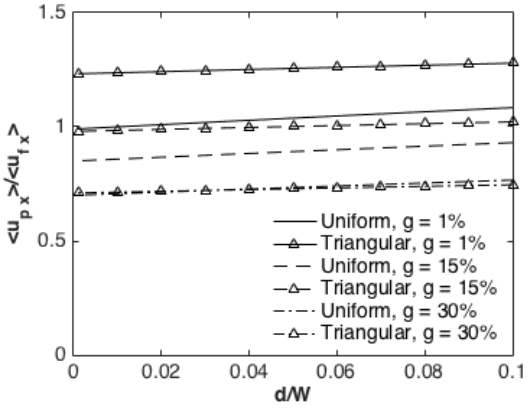

Figure 3.7. Average particle velocity normalized by the average fluid velocity versus particle diameter to slot width ratio for several values of average concentration.

The results in Figure 3.7 illustrate that for dilute average concentration, 1%, distributed uniformly or with a triangular peak, the analytical model predicts an average particle velocity greater than that of the fluid. This is a result of two mechanisms. Firstly, the local particle velocity is very close to the local fluid velocity since the concentration dependent slip velocity is negligible. Secondly, the particle is excluded from the slower moving fluid closer than half its diameter from the walls due to its size. The average particle velocity for a triangular distribution is greater as more particles are located in a region of larger local fluid velocity at the center of the slot.

For an average concentration of 15%, the average particle velocity is reduced substantially for both concentration distributions considered, relative to that for dilute

concentration. There is less difference between the average particle velocity predicted for the uniform and triangular distributions. While more particles are present in a region of larger local fluid velocity for the triangular particle distribution, this effect is substantially offset by the local concentration reducing their velocity relative to that of the fluid. The average particle velocity for a uniform distribution is significantly less than the average fluid velocity, while these two quantities are approximately equal for the triangular concentration distribution.

Considering an average concentration of 30%, the average particle velocity relative to the average fluid velocity for both concentration distributions is close to the same and substantially reduced compared to the 15% and dilute concentration cases. This is a quite remarkable result since the reduction in local particle velocity resulting from increased particle concentration at the center of the slot almost completely offsets the effect of larger local fluid velocity.

3.6. Multiple-Particle Slot Poiseuille Flow Simulations

3.6.1 Multiple-Particle Slot Poiseuille Flow Overview

This research has demonstrated two separate mechanisms responsible for particles translating at less than the surrounding fluid velocity. The first is the observation that a single particle in slot Poiseuille flow exhibits a slip velocity relative to the local fluid velocity. The second is a concentration effect whereby the average particle velocity is reduced by a factor of $(1-c)$ compared to the average fluid velocity in uniform flow. The following simulations of multiple particles in slot Poiseuille flow enable examination of the effects of both these mechanisms simultaneously.

The same domain, boundary condition type and initial conditions used for the verification and single particle slot Poiseuille flow simulations have been used for

simulations at non-dilute particle concentrations. As for the multiple particle uniform flow simulations, large and non-physical particle repulsion velocities have been avoided upon initialization by the particle seeding approach used. This involves determining initial particle positions with each coordinate value selected from a uniform distribution bounded by limits one particle radius inside the DEM simulation domain boundary and rejecting overlapping positions. The modified average fluid velocity was used as the initial velocity for all particles and the boundary conditions used produce a constant concentration for the duration of the simulation.

The effect of particle concentration, Reynolds number, Newtonian fluid viscosity, particle size and fluid loss through the walls was examined. The effect of shear-thinning power-law fluid rheology, as well as particle properties including density and elastic moduli upon the dimensionless particle velocity were also studied.

3.6.2 Multiple-Particle Slot Poiseuille Flow Results

In each simulation case, particles have been seeded with a velocity equal to the modified average fluid velocity. It takes only a small period of time for particles to accelerate or decelerate according to their position in the slot. An example of this response is provided in Figure 3.8, which shows the x component of velocity for each particle at several points in time, for a particular simulation case.

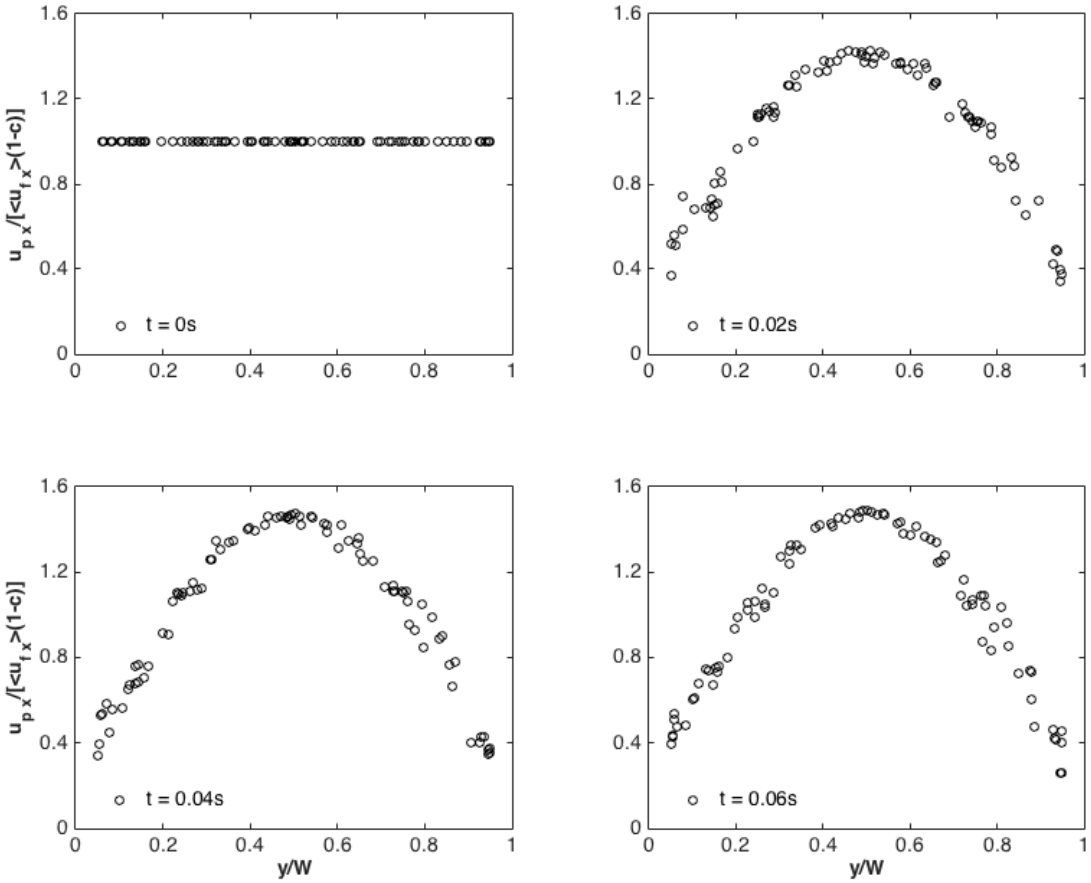

Figure 3.8. Particle velocity normalized by modified average fluid velocity versus dimensionless slot position at four points in time, including the initial condition.

The velocity of each particle for a simulation case at Re_s equal to 1000, c equal to 15% and d/W equal to 0.1 is shown in Figure 3.8. The top left pane shows the initial condition, while the remaining panes show the progression with time. It is apparent that from 0.02s on, the x component of velocity of the individual particles is similar. The concentration distribution from the simulation case presented in Figure 3.8 is shown in Figure 3.9.

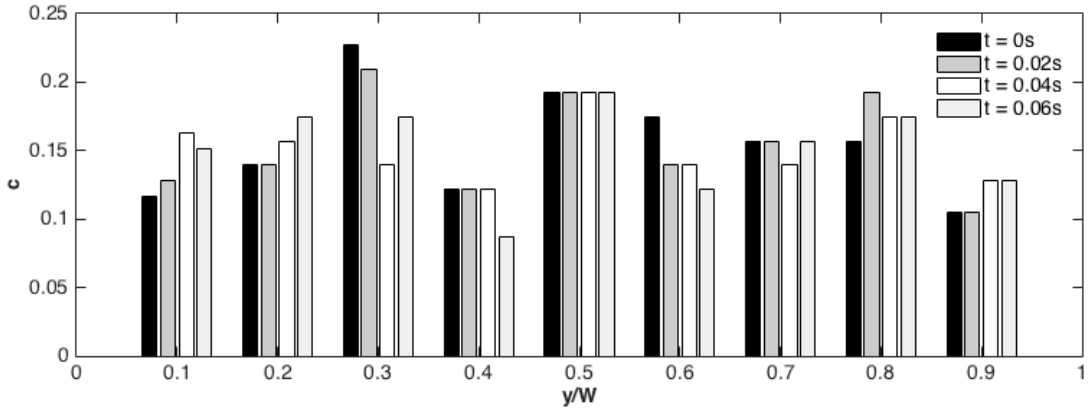

Figure 3.9. Concentration versus dimensionless slot position at four points in time, including the initial condition.

The progression of the concentration distribution with time is shown in Figure 3.9, with the concentration calculated based upon the particles present in each of 9 bins of finite size. The initial condition is an approximately uniform distribution. As the simulation progresses, there is an increase in concentration near both walls, a reduction in concentration in between each of the two walls and the center of the slot and finally a constant concentration at the center of the slot.

The precise center of the slot is an unstable equilibrium position. In the center region, lateral forces are smaller than closer to the walls, producing no net migration over the period of time for which simulation data is available. The increase in concentration near the walls may be due to neglecting the lift force from particle rotation, leaving the inertial lift related to shear slip and lift caused by the velocity profile curvature unbalanced.

The individual particle velocity response, shown in Figure 3.8, occurs more quickly than the more gradual changes in the concentration distribution, shown in Figure 3.9. It is not possible to determine the steady state concentration distribution in the absence of the lift force from particle rotation. Therefore the implementation used

(specifically the simplification made when imposing the particle velocity on the CFD representation of the system without the rotation component) limits application to that of a concentration distribution similar to the initial condition, in this case, an approximately uniform distribution.

Three sets of simulations, each with a different initial seeding produced from the same method as described above is presented. Each set of simulations consists of a range of particle to slot width ratios and were at Re_s equal to 1000 and c equal to 15%. The results of these simulations are presented in Figure 3.10.

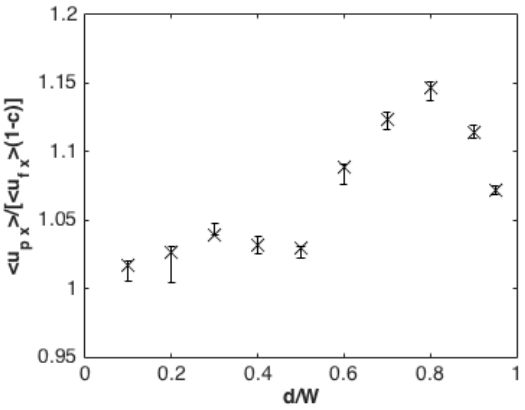

Figure 3.10. Average particle velocity normalized by modified average fluid velocity versus particle diameter to slot width ratio for three sets of initial particle seeding.

The result of each of the three simulations at each value of d/W are presented in Figure 3.10 with the minimum, middle and maximum value determined shown. This demonstrates that there is a range in the results from simulations with different seeds. Of course, particles could have been seeded with a precisely uniform distribution, for example, using positions on a square grid as one possible approach. However, it is highly unlikely that any practical application would yield such a concentration distribution so this approach was not used. The scatter in the results provides a guide to the repeatability

of the subsequent results shown. Simulation results from sets of cases at five different particle concentrations from 5% to 25% are shown in Figure 3.11.

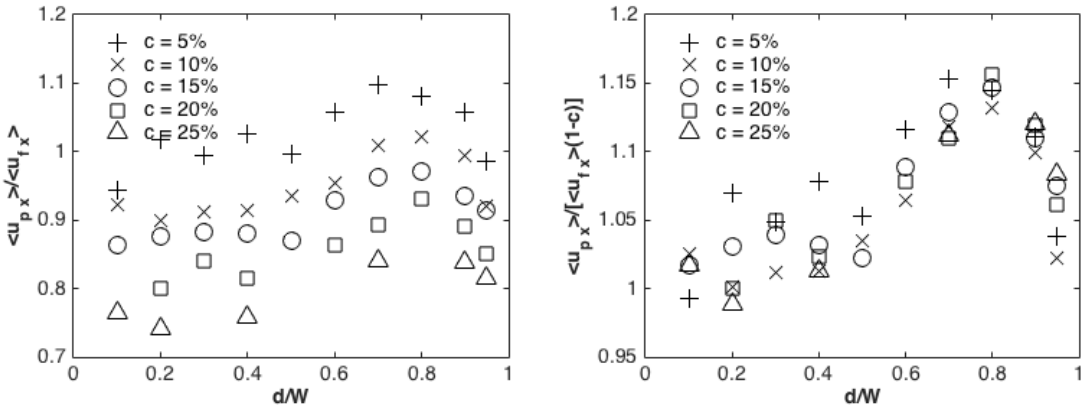

Figure 3.11. Left: Average particle velocity normalized by the average fluid velocity versus particle diameter to slot width ratio. Right: Average particle velocity normalized by the modified average fluid velocity versus particle diameter to slot width ratio.

The results shown in the left pane of Figure 3.11 demonstrate that concentration dependence, similar to that for particles in uniform flow, is present for particles in slot Poiseuille flow. That is, particles present at larger concentration are transported at lower velocity. Examining the results for larger ratios of particle diameter to slot width, there is a peak in the results at d/W of 0.8 for all concentrations examined. When the average particle velocity is normalized by the modified average fluid velocity, shown in the right pane of Figure 3.11, the result is close to a value of one for d/W of 0.4 and smaller. The scatter present is of similar magnitude to that observed in Figure 3.10 and thereby difficult to distinguish from that due to the seeding used. The relationship proposed for particles in uniform flow may be applied to slot Poiseuille flow as a good approximation for this range of d/W.

There is very little data available in the literature for comparison to these two observations. Staben *et al*. (2003) extended the results of their single particle simulations in slot Poiseuille flow at low Reynolds number to a uniform dilute concentration, presenting the average particle velocity normalized by the average fluid velocity for a range of particle diameter to slot width. The results are reproduced in Figure 3.12 for comparison.

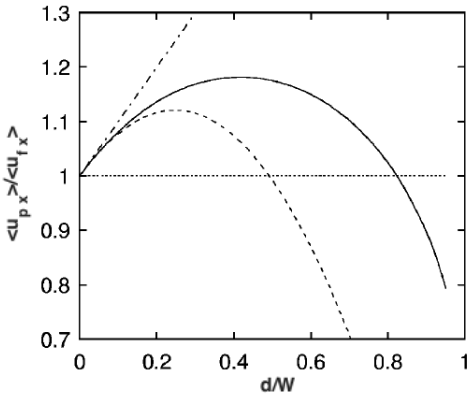

Figure 3.12. Average particle velocity normalized by the average fluid velocity versus particle diameter to slot width ratio from Staben *et al*. (2003). The dashed curve is from asymptotic theory, the dot-dashed line is the first order correction and the solid curve is from the full numerical calculations of Staben *et al*. (2003).

This work presents results at larger Reynolds number and non-dilute concentration and as such agreement between the two results should not be expected. In fact, a Reynolds number effect whereby a single particle translates at a larger dimensionless velocity at the center of the slot for larger Reynolds number was identified in this work (results are shown in the top left pane of Figure 3.4). As anticipated, the results of Staben *et al*. (2003) are different to the results in this research. For the range of d/W 0.4 and smaller, the results of Staben *et al*. (2003) are larger than those in this work, while over most of the range of d/W larger than 0.4 they are smaller. For d/W of 0.4 and

smaller, it appears that the concentration effect governs the normalized average particle velocity and the wall retardation effects are much less important. For larger d/W, greater than 0.4, there are two mechanisms which determine the results.

Excluding the simulations conducted for verification purposes, all results are from simulations conducted at a Reynolds number three orders of magnitude higher than the valid range for those of Staben *et al*. (2003). As there is a demonstrated effect of fluid inertia reducing the slip velocity of a single particle, a similar effect may be apparent in multiple particle cases also.

Lateral migration does not occur for a single particle at low Reynolds number. When multiple particles are present and transported with a fluid at larger Reynolds number, there is considerable lateral movement as they undergo collisions with each other and walls. While a particle being transported by the faster moving fluid in the center of the slot will slow down somewhat as it moves to a region of slower moving fluid near either of the walls, it may well still be travelling faster than a single particle translating at that position in the slot would be. The latter is the result from which Staben *et al*. (2003) correctly makes their calculation for dilute concentration, but this approach cannot be rigorously applied to the larger non-dilute cases examined here.

A second comparison between these results can be made to the experiments of Koh *et al*. (1994). Their results demonstrated a significant reduction in particle velocity when comparing experimental results at particle concentrations of 30% and 10%. Quantitative particle velocity data were not provided and the experiments were conducted at very small Reynolds number. Despite these caveats, qualitative agreement with the results of this work is noted.

Results from simulations examining the effect of the following variables, Reynolds number, Newtonian fluid viscosity, particle size and fluid loss through the walls are presented in Figure 3.13.

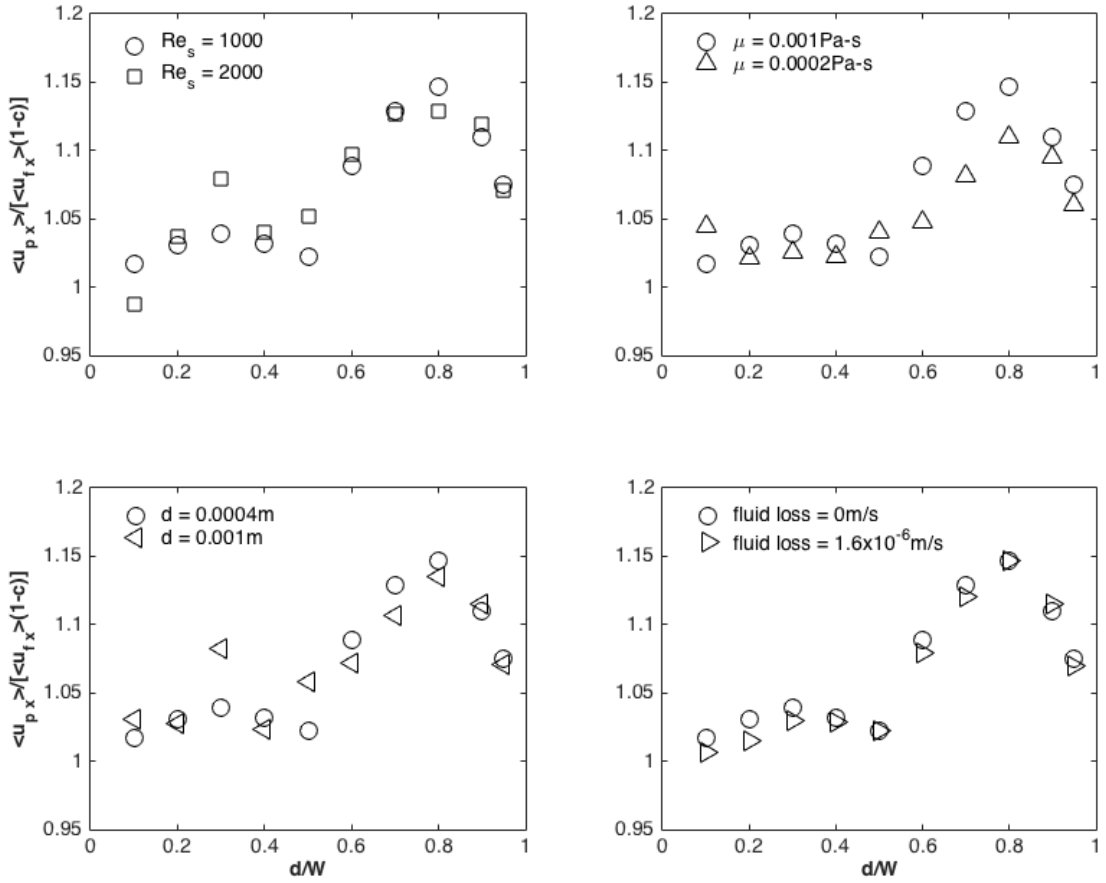

Figure 3.13. The average particle velocity normalized by the modified average fluid velocity versus particle diameter to slot width ratio. Top left: Reynolds number. Top right: Newtonian fluid viscosity. Bottom left: Particle diameter. Bottom right: Fluid loss through the walls.

All the results presented in Figure 3.13 demonstrate the same trend observed in the right pane of Figure 3.11. There is not a systematic difference between results at a Reynolds number of 1000 and 2000, shown in the top left pane. The single particle results shown in the top left pane of Figure 3.4 showed a very small Reynolds number

effect between results at 1000 and 2000 (though there was a significant effect when compared to results for a Reynolds number of one). There is an absence of a systematic trend in the results due to each independent variable examined and simply scatter of a similar magnitude to the random seeding effect.

The top right and bottom left panes of Figure 3.13 show that there is not a systematic difference in the simulation results from cases with a Newtonian fluid viscosity of 0.0002Pa-s and 0.001Pa-s nor a particle size of 0.0004m and 0.001m. In each of these cases the Reynolds number is the same, 1000, and demonstrates clearly that this dimensionless group is appropriate for reducing the results to dimensionless terms, as was the case for the single particle results. The results shown in the bottom right pane demonstrate that there is not a systematic difference in the normalized average particle velocity due to fluid loss through the walls. The fluid loss velocities apparent in most engineering applications are much smaller than the average fluid velocity. In the case shown in the bottom right pane, the average fluid velocity in the *x* coordinate direction is 0.125m/s, more than four orders of magnitude greater than the fluid loss velocity. A set of simulations has been conducted with a shear-thinning power-law fluid with η_c of 0.1Pa-s and *n* of 0.2, with the results shown in Figure 3.14.

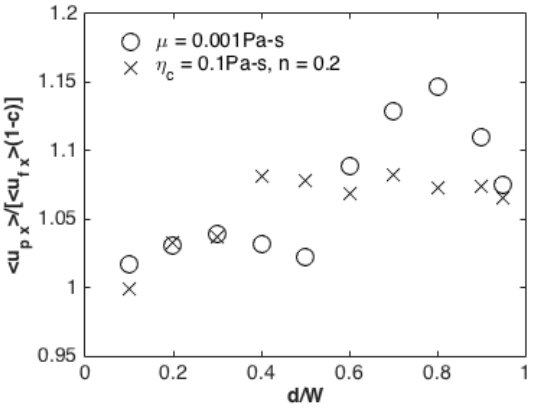

Figure 3.14. Average particle velocity normalized by the modified average fluid velocity versus particle diameter to slot width ratio for different fluid rheology.

Examining the results shown in Figure 3.14, there is a difference in the trend apparent between the simulation results with Newtonian and shear-thinning power-law fluids. The power-law fluid cases show a much 'flatter' trend without the characteristic peak at the *d/W* value of 0.8 observed for the Newtonian fluid. As for the single particle cases, this result is a product of the much more 'blunt' fluid velocity profile across the slot for the power-law fluid. Finally, a set of simulations has been conducted with a particle Young's modulus of 324GPa and a Poisson's ratio of 0.25, to compare to 99GPa and 0.06, representative of the elastic moduli of a typical high-density ceramic and quartz sand, respectively. A particle density of 3600kg/m^3 and 2650kg/m^3 comparison has also been completed to reflect typical values for these two materials.

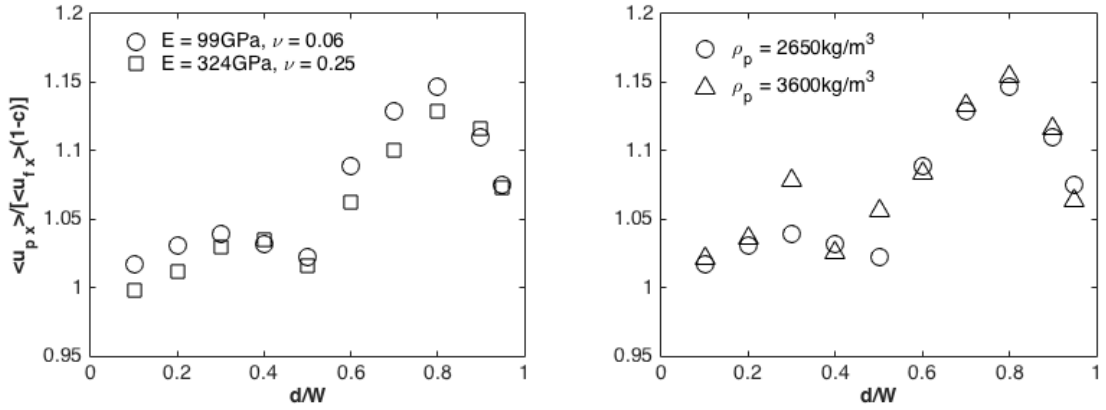

Figure 3.15. Average particle velocity normalized by the modified average fluid velocity versus particle diameter to slot width ratio. Left: Particle elastic moduli. Right: Particle density.

Figure 3.15 demonstrates that the particle elastic moduli and the particle density do not systematically alter the average dimensionless particle velocity.

3.7 CONCLUSIONS

The fully resolved simulation approach used in this work has been validated for the specific application of interest, determining the velocity of particles transported in slot Poiseuille flow. This verification was completed by comparison to a solution from the literature for a single particle translating at the two limits of particle position in a low Reynolds number flow, next to the wall and in the center of the slot. The two sets of results are in good agreement and demonstrate that a particle always translates more slowly than the undisturbed local fluid velocity. There is always a slip velocity between the particle and the fluid on a local basis. The effect of inertia at larger Reynolds number was shown to reduce the particle slip velocity for a particle translating in the center of a slot for large values of particle diameter to slot width, that is, in narrow slots. Examining simulation results from a particle in a shear-thinning power-law fluid, there is less wall

retardation as a result of the more blunt velocity profile compared to that observed for a Newtonian fluid.

Using a suitable set of boundary conditions to produce uniform flow in a representation of an infinite domain, the effect of particle concentration upon the average translation velocity was shown to be significant. Increasing particle concentration reduces translation velocity in a linear manner. This result was used in the development of a simplified analytical model for the cross-slot average particle translation velocity. The analytical model was evaluated for two different concentration distributions and at several concentrations across a range of particle diameter to slot width ratio. Remarkably, the dimensionless average particle velocity was shown to be relatively insensitive to the concentration distribution at larger concentrations, due to competing effects related to the local fluid velocity and particle concentration.

Finally, results from simulations of multiple particles in slot Poiseuille flow were presented. These demonstrated that the average particle velocity was reduced with increased concentration, as shown for particles in uniform flow. In addition, there was found to be a peak in the dimensionless average particle velocity at a particle diameter to slot width ratio of 0.8 for a Newtonian fluid. There was a significantly less pronounced peak for a shear-thinning power-law fluid.

Chapter 4: Settling of Non-Dilute Suspensions in Open Slots

The steady state settling velocity of particles at non-dilute concentrations in a fluid filled open slot has been quantified through application of the simulation approach detailed in Chapter 2. In addition, the resultant average fluid velocity surrounding the particles has been examined.

4.1 INTRODUCTION

A disperse phase, distributed in a second continuous phase, is transported as a result of the difference between the gravity and buoyancy forces arising from the density difference between the two phases. If the densities of the two phases are equal, the disperse phase is described as neutrally buoyant and there is zero net force acting upon it. If the disperse phase is less dense, for example gas bubbles in a liquid, it will rise. Conversely, if the disperse phase is more dense, for example solid particles in a liquid, settling (also referred to as sedimentation) occurs. For a disperse phase rising or settling, a velocity dependent drag force opposes the motion of each bubble or particle and the equilibrium of forces results in a steady state or 'terminal' velocity. This transport mechanism is distinctly different from flow of the continuous phase due to a macroscopic pressure gradient, which also affects transport of the disperse phase. In many industrial applications the two transport mechanisms act simultaneously.

The particle diameter (m), d, is the characteristic length used for the calculation of the dimensionless particle Reynolds number, Re_p, which is given by:

$$Re_p = \frac{du_p\rho_f}{\mu} \qquad (4.1)$$

where u_p is the particle velocity (m/s), ρ_f is the fluid density (kg/m^3) and μ is the fluid dynamic viscosity (Pa-s). Stokes (1851) published one of the earliest theoretical studies of particle settling. An analytical solution to the terminal velocity of a single rigid sphere falling through an infinite volume of a Newtonian viscous fluid, at $Re_p << 1$, was developed from equilibrium of the gravitational, buoyancy and form and friction drag forces acting. The eponymous solution provided by Stokes is given by:

$$u_{Stokes} = \frac{d^2\left(\rho_p - \rho_f\right)\mathbf{g}}{18\mu} \qquad (4.2)$$

where u_{Stokes} is the Stokes' settling velocity (m/s), ρ_p is the particle density (kg/m^3) and $\boldsymbol{g}$ is acceleration due to gravity (m/s^2). As noted above, Stokes' law is valid for a particle at terminal velocity in an infinite fluid domain. When an immersed particle is in a dilute suspension in an infinite volume of fluid, this solution provides an accurate calculation of its terminal velocity. However, when the fluid domain is bounded at the same scale as the particle size, this key assumption used in the development of Stokes' law is no longer valid and the velocity predicted is not accurate.

Ganatos *et al*. (1980) provided a solution to one such case which includes the effect of a spatially constrained fluid domain geometry whose size is comparable to the particle size (for a particle settling between two planar walls forming a slot). The form of the solution given is that of a dimensionless force coefficient, F_t, which quantifies the reduction in settling velocity due to both the spacing of the walls and the position of the particle between the walls, compared to the velocity predicted by Stokes' law. Both smaller wall spacing and closer proximity to a wall, for a given wall spacing, produce larger reductions in the terminal velocity of a particle. The solution is as shown:

$$u_{Ganatos} = \frac{d^2\left(\rho_p - \rho_f\right)\mathbf{g}}{18F_t\mu} \qquad (4.3)$$

where $u_{Ganatos}$ is the modified Stokes' settling velocity (m/s). The other assumptions made in the development of Stokes' law, that of creeping flow and the particle falling in a Newtonian fluid, also apply to this solution. In many applications, Re_p is larger than one and the flow cannot be described by the solutions for creeping flow, such as those provided by Stokes (1851) or Ganatos *et al*. (1980). In these flow regimes, inertial effects are important and can be accounted for through empirical friction factor solutions for the drag force, such as those available in Bird *et al*. (2007). The friction factor, f, provided by Bird *et al*. (2007) for a sphere in motion at $Re_p < 6000$ is given by:

$$f = \left(\sqrt{\frac{24}{\mathrm{Re}_p}} + 0.5407 \right)^2 \quad (4.4)$$

All terminal settling velocity solutions discussed above are applicable only to a single particle settling. When multiple particles are present in a closed system, the settling velocity is reduced relative to that of a single particle. This reduction in settling velocity is often quantified by a modification to a single particle settling solution based on an empirical function of volumetric particle concentration, c. A commonly used 'hindered settling' correlation is that of Richardson and Zaki (1954). Other correlations, each developed for a specific application, are available. See Peker and Helvaci (2008) for a comprehensive review of such correlations.

$$u_{Richardson\,and\,Zaki} = u_t \left(1 - c\right)^s \quad (4.5)$$

where $u_{Richardson\ and\ Zaki}$ is the settling velocity (m/s) predicted by Richardson and Zaki (1954), u_t is the settling velocity of a single particle under the same conditions and s is an empirical function of d, the fluid domain geometry and Re_p. Use of hindered settling correlations is entirely appropriate if they are applied to systems with geometry similar to that used in their development. For example, Richardson and Zaki (1954) developed the correlation above from physical experiments where a concentrated suspension settled in a

closed tube and as a result it can be applied to similar systems with an appropriate value of *s*. However, this correlation cannot be used accurately in the case of particles settling between the planar walls of a slot, as the domain geometry is different.

The motion of spherical solid particles settling in a fluid between the two planar walls of a slot is solved directly in this research. The forces exerted by the fluid on each of the particles is determined directly and used to calculate their trajectories. As the particles move, the boundary of the fluid domain surrounding the particles is altered and the velocity and pressure throughout the domain is calculated. This simulation approach was pioneered by Hu *et al*. (1992), where a finite element formulation was applied to the study of two-dimensional cylinders settling in a quiescent incompressible Newtonian fluid within a rectangular domain. While a two-dimensional implementation is clearly a significant simplification, Hu *et al*. (1992) successfully qualitatively reproduced 'drafting, kissing and tumbling' which was observed in physical experiments where spheres settled in a fluid, the details of which are available in Fortes *et al*. (1987). Johnson and Tezduyar (1996) used a similar finite element solution to create a fully three-dimensional implementation and studied two to five spherical particles settling in a tube, also successfully reproducing the scenario of 'drafting, kissing and tumbling'. The same authors later extended the application of their approach to approximately 100 spheres settling in a tube, with both mono-disperse and poly-disperse cases examined, as reported in Johnson and Tezduyar (1997). Each of these contributions have been validated and are useful for their specific application. However, as is the case with the correlations developed by Richardson and Zaki (1954), they are not directly applicable to particles settling in a slot, as the geometry of the system is different.

In this study, non-dilute suspensions of particles settling in a slot with closely spaced walls have been simulated, allowing the average settling velocity to be quantified.

The effect of slot wall spacing, volumetric particle concentration, Newtonian fluid viscosity, particle size and particle density have each been examined.

4.2 Application to Particle Settling

4.2.1 Simulation Domain and Boundary Conditions

A sufficiently tall domain is required to allow particles to attain a steady state settling velocity. However, run time constraints and the computational expense of the method necessitate as small a domain as possible to allow for an adequate quantity of simulation data to be produced for subsequent analysis. The simulation domain is shown in Figure 4.1, drawn approximately to scale except for height, which has been compressed for practical reasons.

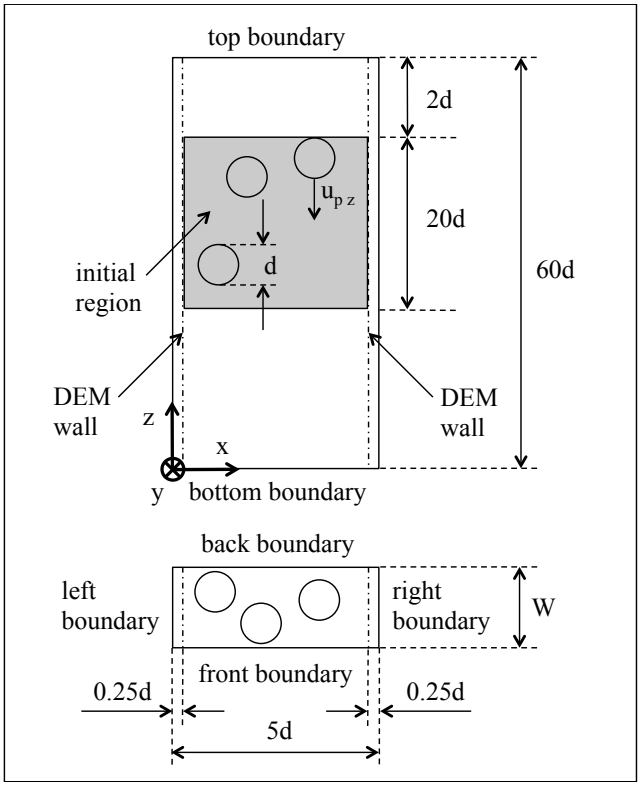

Figure 4.1. Simulation domain.

The wall spacing in the y coordinate direction, W, is selected based on the particle diameter and the ratio d/W required for each simulation case, between 0.5 and 0.95 inclusive. The height of the domain in the z coordinate direction, $60d$, is large enough for particles to attain terminal settling velocity prior to reaching the bottom of the simulation domain. The initial region is $20d$ in height and $4.5d$ in length. As a result, the range in volume of the DEM domain is ~$94.7d^3$ to $180d^3$, corresponding to d/W equal to 0.95 and 0.5 respectively. Only 9 particles are required to provide a volumetric concentration of 5% in the smallest domain, whereas 52 particles provide 15% concentration in the largest domain.

The initial and boundary conditions applied to the CFD domain are as follows:

Both the pressure and velocity fields are set to zero across the fluid domain initially

At the *left* and *right* boundaries: cyclic pairing

$$u_{fx}\big|_{x=0} = u_{fx}\big|_{x=5d} \qquad u_{fy}\big|_{x=0} = u_{fy}\big|_{x=5d} \qquad u_{fz}\big|_{x=0} = u_{fz}\big|_{x=5d} \qquad p\big|_{x=0} = p\big|_{x=5d} \tag{4.6}$$

where u_{fx}, u_{fy} and u_{fz} (m/s) are the scalar components of the fluid velocity vector. Cyclic pairing is used for the boundaries perpendicular to the x coordinate direction to represent a domain infinite in extent in this direction.

At both the *front* and *back* boundaries: no slip condition

$$u_{fx} = 0 \qquad u_{fy} = 0 \qquad u_{fz} = 0 \qquad \frac{\partial p}{\partial x} = 0 \tag{4.7}$$

No slip boundaries perpendicular to the y coordinate direction represent the two planar walls of the slot.

At the *top* and *bottom* boundaries: constant pressure

$$\frac{\partial u_{fx}}{\partial x} = 0 \qquad \frac{\partial u_{fy}}{\partial x} = 0 \qquad \frac{\partial u_{fz}}{\partial x} = 0 \qquad p = 0 \tag{4.8}$$

Equal and constant pressure boundaries perpendicular to the z coordinate direction ensures that no bulk fluid flow is imposed upon the system in this direction.

The setup used within the DEM domain is as follows:

Sufficient particles needed to provide a specified volumetric concentration within the *initial region* (shown in grey in Figure 4.1) are seeded upon initialization at random non-overlapping positions.

Walls have been placed one quarter of a particle diameter inside the *left* and *right* boundaries. In the absence of these walls, particles in very close proximity to the cyclic boundary were found to not reach a steady state settling velocity, whereas they did at all other x coordinate positions provided that they were initially at a sufficient height (z coordinate) in the domain. This is a numerical artifact produced by the CFD representation of particles interacting with the boundary condition imposed. The walls placed inside the domain avoid this numerical artifact at the expense of introducing additional particle to wall collisions not related to modeling the physical system. Nonetheless, particles do interact at a distance via the flow field around each one across the cyclic paired *left* and *right* boundaries.

Walls are also placed at the *front* and *back* boundaries to represent the walls of the slot.

4.2.2 Verification

The reduction in settling velocity compared to Stokes' law calculated by Ganatos *et al*. (1980) for a single particle settling between two planar walls of a slot has been used to validate the simulation approach described above. Ganatos *et al*. (1980) provided F_t as a function of both the spacing of the walls and the position of the particle between the walls. A continuous solution is provided in graphical form between 1.1 radii from a wall

to the center of the slot. These two limits of particle position have been used for comparison, for each of three separations between the walls.

A single particle with diameter of 0.0004m and density of 2650kg/m^3 was placed at the center of the simulation domain in the x coordinate direction. A position at either the center or 1.1 radii from a wall in the y coordinate direction and at the top of the *initial region* was used for each simulation case, with the particle initially at rest. The slot walls were spaced such that d/W was equal to 0.5, 0.67 or 0.8, for a total of six cases. The Newtonian fluid properties used for all cases were ρ_f of 1000kg/m^3 and μ of 0.1Pa-s. The settling velocity predicted by Stokes' law (4.2) places the flow regime within $Re_p << 1$. The results of the simulations are shown in Figure 4.2.

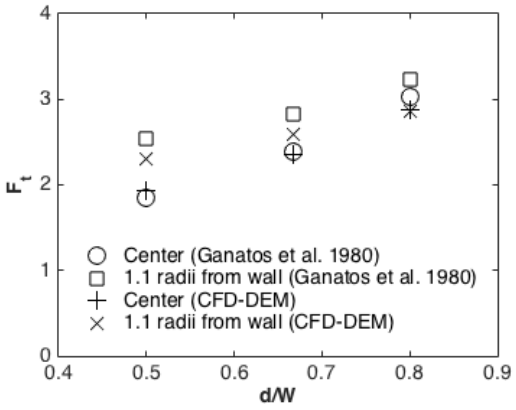

Figure 4.2. CFD-DEM verification results compared to those from Ganatos *et al*. (1980).

For each simulation case, the x and y components of the velocity of the particle were negligible for the duration of the simulation, while the z component demonstrated acceleration from rest to steady state. The terminal velocity, along with d, ρ_p, ρ_f and μ, were used to calculate F_t by rearrangement of (4.3). These results presented in Figure 4.2 shows reasonable agreement with the solution from Ganatos *et al*. (1980), illustrating the suitability of the method to particles settling in a slot. The percentage difference between

F_t was no greater than 12% in each case considered and in most cases much less. Through the process of developing the simulation case setup, it was found that a larger domain size in the x coordinate reduced the difference between the simulation result and the solution of Ganatos *et al*. (1980). A domain size of 5d was selected as a trade off between increased accuracy and the production of less simulation data for a given run time.

4.2.3 Data Analysis

For the non-dilute simulation cases examined, particles are initialized in the *initial region*. Subsequently, the position and velocity of each particle is calculated by the DEM code at each time step. For practical analysis purposes (due to the small time steps required for DEM simulation), the simulation data has been recorded at a prescribed multiple of time steps, 100. The mean of the z component of velocity of each particle, $<u_{p_z}>$, has been calculated for each recorded state of the system. That is, an average over all particles has been determined, allowing the progression of the system towards steady state to be observed as the particles settle.

As discussed above, particles are initially placed at a specified volumetric concentration in the *initial region*. During settling, differences in settling velocity between individual particles, due to proximity to the slot walls and other particles, are sufficiently small that there remains a region of the domain with approximately the same volumetric concentration as initially specified. Of course, the location of this region moves down with time as the particles settle. This results in two volumes of fluid with no particles present, one above and one below the particle region. The particles 'drag' fluid with them as they settle, which is quantified in several cases. This calculation has been made indirectly from the average of the z component of the fluid velocity at the top

boundary, $\left\langle u_{fz} \right\rangle\Big|_{z=60d}$, modified for the particle region. Conservation of mass and the boundary conditions imposed on the *left*, *right*, *front* and *back* require the mass rate of the fluid to be constant with height in z. This allows $\langle u_{fz} \rangle$ to be determined in the particle region simply by consideration of the value of c, as shown:

$$\left\langle u_{fz} \right\rangle = \frac{\left\langle u_{fz} \right\rangle\Big|_{z=60d}}{1-c} \qquad (4.9)$$

An example of the averages taken from the simulation data produced for a case with c equal to 0.15 and d/W equal to 0.80 is shown in Figure 4.3.

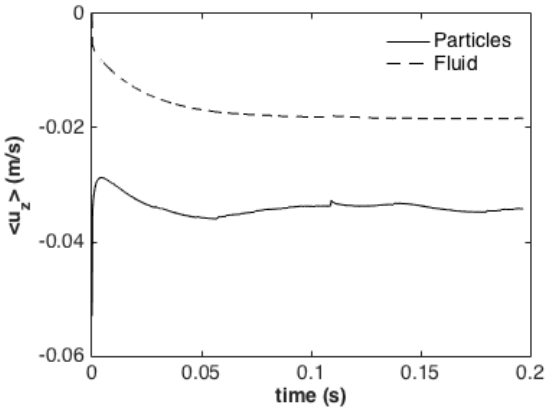

Figure 4.3. Average particle settling velocity and average of the z component of the fluid velocity for fluid surrounding the particles versus time.

Both the average particle and average fluid velocities shown in Figure 4.3 demonstrate that the system reaches steady state at approximately 0.06s. Since the simulation includes a relatively small number of particles, just 32 in this particular case, there is some variation in $\langle u_{pz} \rangle$ from 0.06s onwards as collisions occur and particles interact hydro-dynamically as they settle. There is little variation in $\langle u_{fz} \rangle$ surrounding the particles from 0.06s on. In subsequent analysis, a time average from steady state to completion of the simulation is presented for both average velocities.

4.3 RESULTS

4.3.1 Effect of Concentration and Slot Width

The effect of volumetric particle concentration and slot width upon the particle settling velocity has been examined. The particle diameter and density specified are 0.0004m and 2650kg/m^3, respectively, while the Newtonian fluid viscosity is 0.001Pa-s and fluid density 1000kg/m^3. Assuming that the fluid is unbounded for the purposes of estimating the particle settling velocity, by the friction factor solution of Bird *et al*. (2007), (4.4), the particle Reynolds number is outside of the creeping flow regime. Simulations with concentration from 0.05 to 0.25 and particle diameter to slot width from 0.5 to 0.95 have been completed and the results are presented in Figure 4.4.

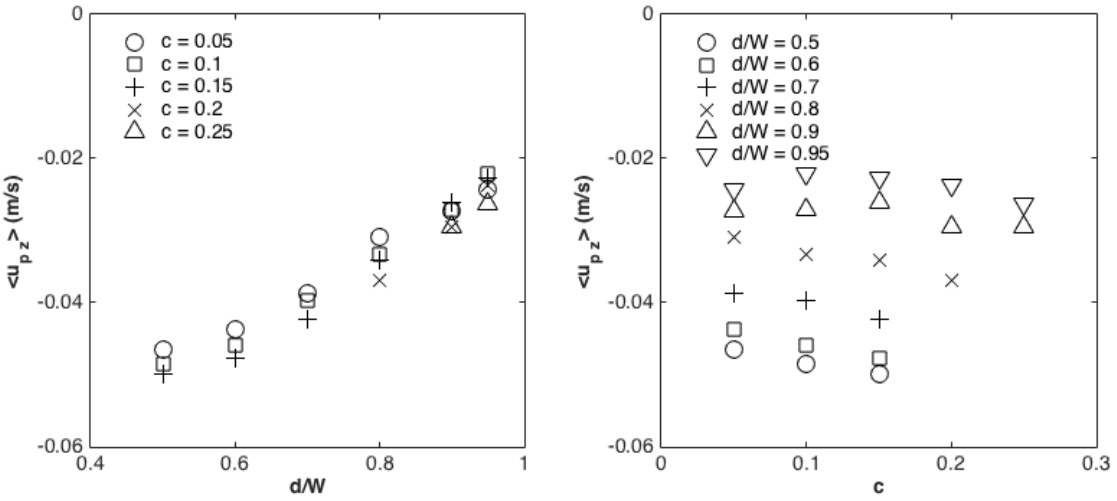

Figure 4.4. Left: Average particle settling velocity versus particle diameter to slot width ratio. Right: Average particle settling velocity versus concentration.

The left pane of Figure 4.4 presents the average particle settling velocity versus d/W and demonstrates that larger d/W, which corresponds to smaller W, reduces the average particle settling velocity for all c. While the results of Ganatos *et al*. (1980) are

for a single particle settling at a particular position in a slot and within a creeping flow regime, there is qualitative agreement between these results.

The right pane of Figure 4.4 shows the same settling velocity plotted versus c. It is apparent that in most cases there is a small increase in the average particle settling velocity with larger c. Correlations of the type presented in Richardson and Zaki (1954), (4.5), predict a decrease in particle settling velocity with larger c. As discussed, the geometry of this system is different to that used by Richardson and Zaki (1954), however qualitative agreement may be expected if the same boundary conditions were applied. Critically, the boundary conditions applied in these simulations are different. Equal pressure conditions have been applied at the top and bottom of the fluid domain in this study. This allows fluid 'dragged' along by the particles to flow out of the bottom of the domain, while new fluid is drawn in at the top of the domain. This is the only mechanism by which fluid is transported. In contrast, correlations such as (4.5) are typically developed from experiments where a front of particles settles in a liquid within a closed container. In such a system, some fluid is dragged by the particles as is the case of the simulations presented here, but there is also a net fluid flow upwards (in the opposite direction of particles settling) required by conservation of mass considerations. This results in a reduction of the average particle settling velocity. The relationship between the two average velocities, for each the particles and the fluid, is given by:

$$c\langle u_{pz}\rangle + (1-c)\langle u_{fz}\rangle = 0 \quad (4.10)$$

Counter current fluid flow occurs in a hydraulic fracture, but its magnitude may be different to that produced by the advance of a step change concentration front evident in laboratory experiments. The $<u_{fz}>$ surrounding the particles from the simulation cases presented in Figure 4.4 is included in Figure 4.5.

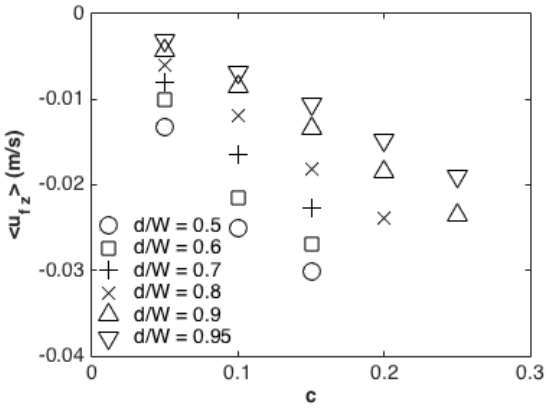

Figure 4.5. Average of z component of fluid velocity surrounding the particles versus concentration.

The simulation data shown in Figure 4.5 demonstrates that $\langle u_{fz} \rangle$ surrounding the particles is larger for larger c, approximating a linear trend. Cases with smaller d/W (which corresponds to a larger W), were found to result in larger $\langle u_{fz} \rangle$ surrounding the particles. If each particle drags along approximately the same volume of fluid, a linear trend with c is expected. The same assumption leads to the conclusion that larger slot width, in which particles settle faster, produces larger fluid velocity as observed in the simulation results.

4.3.2 Effect of Particle Size

The average particle settling velocity has been determined for different particle sizes and slot widths. The particle diameters examined are 0.0004, 0.00055 and 0.0007m, while the slot widths specified result in particle diameter to slot width ratios in the range of 0.5 to 0.95. For all cases, the concentration equals 0.15 and the particle density is 2650kg/m^3, while the Newtonian fluid viscosity and density are 0.001Pa-s and 1000kg/m^3, respectively. The results are presented in Figure 4.6.

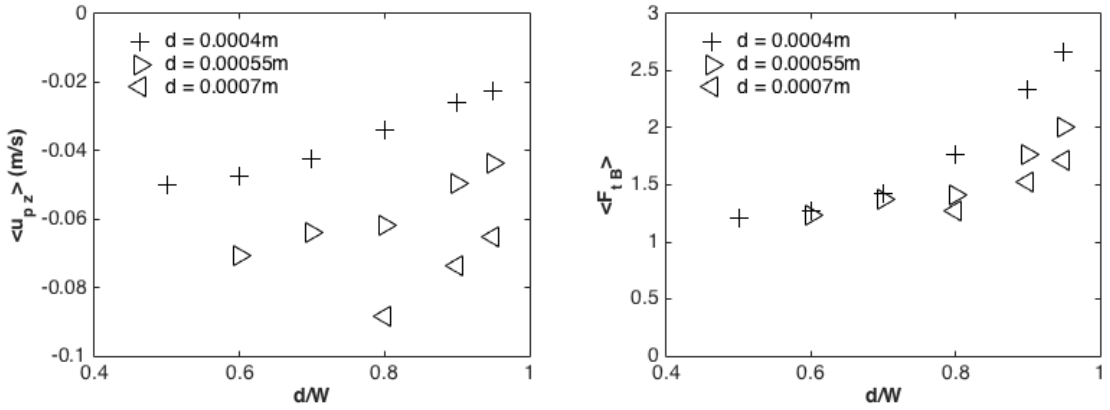

Figure 4.6. Left: Average particle settling velocity versus particle diameter to slot width ratio. Right: Average dimensionless force coefficient (from (4.4)) versus particle diameter to slot width ratio.

The results shown in the left pane of Figure 4.6 demonstrate that larger d results in larger $\langle u_{p\,z} \rangle$, which is the trend expected from inspection of the available formulae for particle settling velocity. For all d, larger d/W reduces $\langle u_{p\,z} \rangle$. This result is qualitatively in agreement with the results of Ganatos *et al*. (1980), as are the results shown in the left pane of Figure 4.4. Note that while simulations have been completed across the range of d/W noted above, steady state $\langle u_{p\,z} \rangle$ was not attained for larger d and smaller d/W cases and as a result these simulation results are not reported.

The single particle settling velocity calculated from the friction factor solution of Bird *et al*. (2007), (4.4), has been used to normalize $\langle u_{p\,z} \rangle$ for each of the simulation cases. The resultant quantity is termed the average dimensionless force coefficient, $\langle F_{t\,B} \rangle$, and is presented in the right pane of Figure 4.6. This quantity is similar to that presented by Ganatos *et al*. (1980) for a single particle in creeping flow at a specific position in a slot. However, in this case the dimensionless force coefficient is an average across all particles in the system, which are at a variety of positions in the slot and Re_p is outside the creeping flow regime. This normalization is shown to 'collapse' the

simulation results at d/W of 0.6 and 0.7 for d equal to 0.0004 and 0.00055m. For larger d/W, for which simulation results are available for all d, there is separation in the values of $\langle F_t \rangle$ for different d. This is the result of the wall spacing reducing $\langle u_{p\,z} \rangle$ sufficiently that the inertial effect resulting from the dependency upon d does not follow that correlated by the solution of Bird *et al*. (2007). Normalization has also been completed using Stokes' law with the results shown in Figure 4.7.

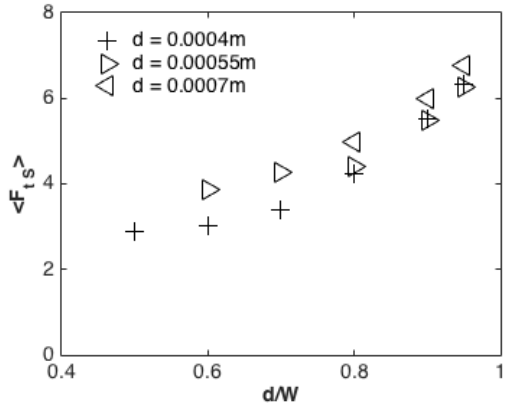

Figure 4.7. Average dimensionless force coefficient (from Stokes' law (4.2)) versus particle diameter to slot width ratio.

Figure 4.7 indicates that normalization by Stokes' law, producing a dimensionless force coefficient denoted $\langle F_{t\,S} \rangle$, produces a better 'collapse' of the simulation data for d/W of 0.9 and 0.95. This is at the expense of the 'collapse' of results for smaller d/W. Even for d/W of 0.9 and 0.95, there is a difference between results for d equal to 0.001m and for results at the other two values of d examined. It is apparent that small wall spacing reduces particle settling velocity by increasing the drag force sufficiently that it becomes approximately proportional to d^2 (see Stokes' law (4.2)). It should be noted that these simulations are all still outside the creeping flow regime with Re_p in the range ~7 to ~28 and it is only the dependency upon the function of d predicted by Stokes' law which reduces the results effectively.

4.3.3 Effect of Particle Density

The effect of particle density and slot width upon the particle settling velocity has been examined. The particle densities considered are 2650, 3125 and 3600kg/m^3. The slots widths, concentration and fluid properties are the same as those used for the simulation cases discussed in prior sections.

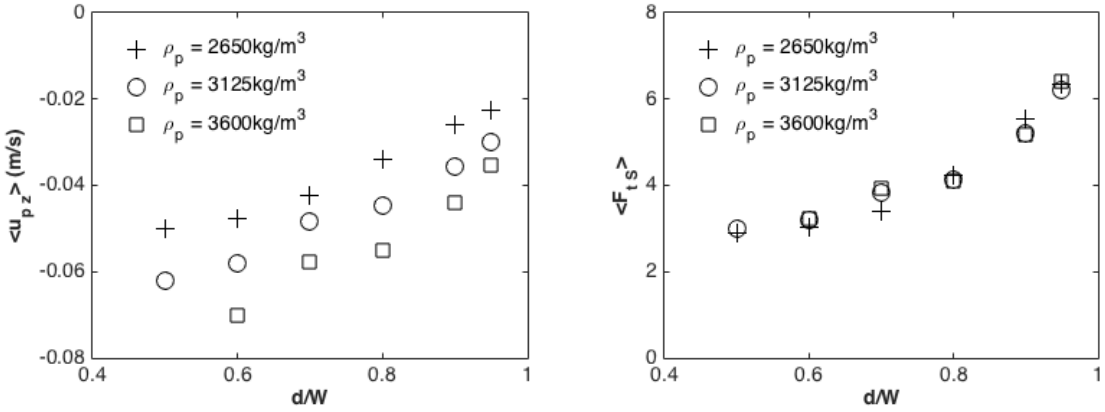

Figure 4.8. Left: Average particle settling velocity versus particle diameter to slot width ratio. Right: Average dimensionless force coefficient (from Stokes' law (4.2)) versus particle diameter to slot width ratio.

The left pane of Figure 4.8 shows that larger ρ_p and smaller d/W results in larger $<u_{p\ z}>$, which is as expected considering the available literature. Both average dimensionless force coefficients previously defined, $<F_{t\ B}>$ and $<F_{t\ S}>$, have been determined and the simulation results collapse better using $<F_{t\,S}>$, as shown in the right pane. As per the simulation results shown in Figure 4.7, the results presented in the right pane of Figure 4.8 are for $<u_{p\ z}>$ outside the creeping flow regime, it is only the dependency upon the function of d predicted by Stokes' law which reduces the results effectively.

4.3.4 Effect of Newtonian Fluid Viscosity

The average particle settling velocity has been determined for different Newtonian fluid viscosity and slot width. Viscosity of 0.0008, 0.001 and 0.0012Pa-s has been specified for three sets of simulation cases. The particle size and slots width ratios, particle concentration and density are the same as those used for the simulation cases discussed in prior sections.

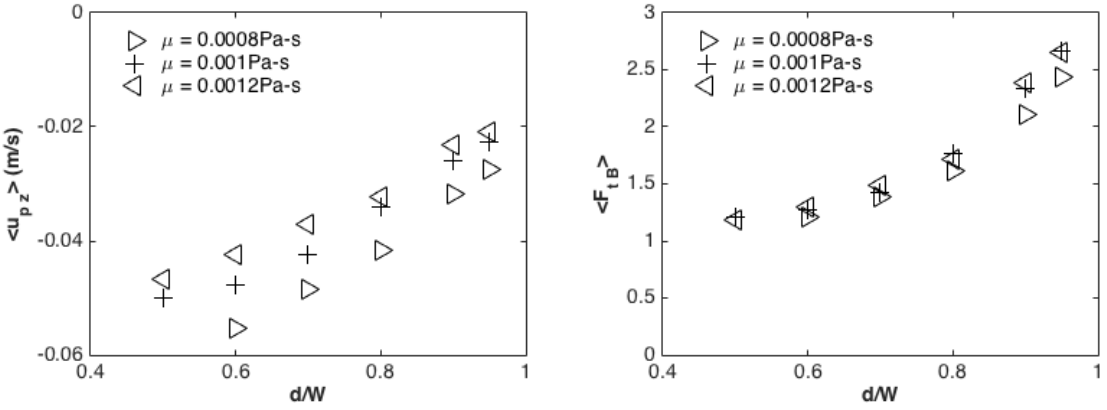

Figure 4.9. Left: Average particle settling velocity versus particle diameter to slot width ratio. Right: Average dimensionless force coefficient (from (4.4)) versus particle diameter to slot width ratio.

The results presented in the left pane of Figure 4.9 demonstrate that smaller μ and d/W both result in larger $\langle u_{p\ z} \rangle$, as expected considering the available literature. Once more, both average dimensionless force coefficients previously defined, $\langle F_{t\ B} \rangle$ and $\langle F_{t\ S} \rangle$, have been determined and the simulation results collapse better using $\langle F_{t\ B} \rangle$, as shown in the right pane.

4.4 CONCLUSIONS

A comprehensive numerical simulation approach, which includes resolution of the fluid flow around particles and determination of their motion on an individual basis, has been applied to determine the steady state average particle settling velocity at non-dilute

concentration in a slot. Prior to this application, verification of the approach was completed through single particle settling simulations in slots of three different widths and at two positions, the results of which compared well to an accepted solution available in the literature for the terminal velocity.

Smaller slot width reduces the average particle settling velocity for all cases examined. Larger concentration was shown to increase the average settling velocity, in apparent contrast to the trend predicted by many correlations available in the literature. This is due to the absence of counter current fluid flow due to the boundary conditions imposed upon the simulation domain. Typical correlations available in the literature have been developed from laboratory scale closed systems where fluid must flow upwards in the space between particles as a result of downward movement of a step change in the particle concentration. In a hydraulic fracture, counter current fluid flow is expected but its magnitude may be different to that produced by the advance of a step change concentration front. This demonstrates that proppant settling in a hydraulic fracture is more complex than usually considered. Larger concentration and slot width increase the fluid velocity downwards in between the settling particles following approximately linear trends.

Larger particle diameter increases the average particle settling velocity, through interaction with the effect of the slot width produces results that cannot easily be reduced by means of the unbounded particle settling velocity calculated at just one Reynolds number. The dependency of average particle settling velocity upon particle diameter changes with slot width. Over the range of independent variables considered, the difference between the particle and fluid densities approximately linearly increases the average settling velocity. This is the same dependency as predicted by Stokes' law, although it should be noted that particles settle outside the creeping flow regime in all

simulation cases considered (with the exception of the verification cases). Larger Newtonian viscosity reduces the average particle settling velocity, approximating the dependency predicted by a friction factor solution for particle settling.

Chapter 5: Effective Propped Fracture Length[1]

Chapter 3 quantified the relative average velocity of proppant and fluid in pressure driven slot flow using the simulation approach detailed in Chapter 2. A correlation has been fitted to these results, allowing their application in a macro scale proppant transport model. The settling velocities calculated in Chapter 4 are available over a small range of slot width and have not been used in the development of the transport model, as doing so would require considerable extrapolation. To complete the proppant transport model, a settling velocity correlation proposed by Liu (2006) has been applied. Inclusion of the transport model in UTEFRAC-3D has enabled calculation of effective propped fracture length.

5.1 INTRODUCTION

Liu (2006) proposed an approximate solution to proppant settling velocity in a hydraulic fracture. This involves modifying u_{Stokes} (4.2) by the use of independent functions to account for inertial, concentration and wall effects. The inertial correction used is provided in an explicit form, which removes the need for iteration required by friction factor solutions such as that available in Bird *et al*. (2007), (4.4). The concentration correction used is a polynomial fitted to the empirical correlations of Nolte (1988), Daneshy (1978), Richardson and Zaki (1954) and Maude and Whitmore (1958). Finally, the wall spacing correction formulated by Liu (2006) is based on the solution of Lorentz (1907) for a sphere translating near a wall. The corrected settling velocity (m/s), $u_{settling}$, is given by:

[1] Many results reported in this chapter were first published in the following:
Blyton, C. A. J., Gala, D. P. and M. M. Sharma, 2015. A Comprehensive Study of Proppant Transport in a Hydraulic Fracture. SPE 174973, presented at the Annual Technical Conference and Exhibition, Houston, Texas, USA, 28-30 September.

$$u_{settling} = u_{Stokes}\left(\frac{m\mu^{0.57}}{\rho_f^{0.29}\left(\rho_p-\rho_f\right)^{0.29}d^{0.86}}\right)\left(1-4.8c+8.8c^2-5.9c^3\right)\left[1-1.563\left(\frac{d}{W}\right)+0.563\left(\frac{d}{W}\right)^2\right]$$

(5.1)

where m is a unit converstion constant, c is the volumetric particle concentration and W is the width of the hydraulic fracture (m).

A continuous piecewise function has been fitted to the CFD-DEM simulation results from Chapter 3, providing the relative average velocity of proppant and fluid in pressure driven slot flow. At particle diameter to slot width ratios equal to or smaller than 0.4, a linear function with a constant value of (1-c) has been used. For d/W greater than 0.4 and less than or equal to 0.95, the product of (1-c) and a cubic polynomial was fitted, for the dependency upon c and d/W respectively. For d/W equal to 1, that is, for a particle diameter the same size as the slot width, it is expected that the particle would jam and as the dimensionless velocity would be zero. Simulations were not conducted for d/W greater than 0.95 and therefore the exact behavior of the dimensionless velocity in this range is not known. As such, the simplest trend possible has been fitted, a linear function for d/W, multiplied by (1-c) for the concentration dependence. The complete correlation fitted is given by:

$$\frac{\langle u_{px}\rangle}{\langle u_{fx}\rangle} = h\left(c,\frac{d}{W}\right) = \begin{cases} (1-c) \text{ if } \dfrac{d}{W} \le 0.4 \\ (1-c)\left[-1.73\left(\dfrac{d}{W}\right)^3+2.45\left(\dfrac{d}{W}\right)^2-0.69\left(\dfrac{d}{W}\right)+1.00\right] \text{ if } 0.4 < \dfrac{d}{W} \le 0.95 \\ (1-c)\left[-21.45\left(\dfrac{d}{W}\right)+21.45\right] \text{ if } \dfrac{d}{W} > 0.95 \end{cases}$$

(5.2)

5.2 HYDRAULIC FRACTURE SIMULATION APPROACH

5.2.1 Incorporation of CFD-DEM Correlations

The correlation developed above for proppant transport in pressure driven slot flow can be incorporated into any hydraulic fracturing simulator. This section provides a brief discussion of how this has been done in a three dimensional planar hydraulic fracturing simulator that couples fracture mechanics with fluid and proppant transport, UTEFRAC-3D. The constitutive equations shown below are based on the appropriate assumptions for an incompressible, isothermal, single phase and single component carrier fluid. The code has additional functionality for modeling compressible fluids and compositional effects, which are necessary for modeling gases and foams. This capability has not been used in this study as the CFD-DEM simulation results are for a single incompressible carrier fluid phase. A detailed description of the Galerkin method based finite element discretization of the differential equations and solution algorithm is available in Ribeiro and Sharma (2013).

5.2.2 Mathematical Problem Definition

The fracture is assumed to be planar, vertical and symmetric with respect to the wellbore (bi-wing) and propagating in a purely elastic medium. Both height and length growth are permitted, with the capability to include horizontal layers with different elastic moduli and minimum horizontal stress. The fracture width is negligible compared to fracture height and length and thus slurry flow through fracture is modeled as two dimensional in the *x-z* plane between parallel porous walls.

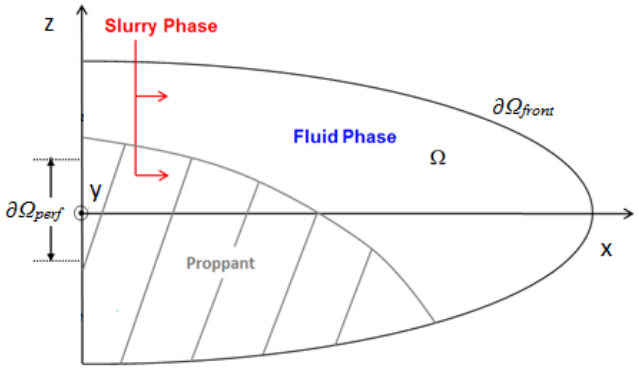

Figure 5.1. Simulation domain, fracture front and the perforated interval along the wellbore, adapted from Ribiero and Sharma (2013).

The illustration of the fracture domain in Figure 5.1 shows the simulation domain, Ω, the fracture front, $\partial\Omega_{front}$, and the portion of the boundary where the injection of slurry is imposed, the perforated interval, $\partial\Omega_{perf}$, which forms an important boundary condition. To model a fracture in a horizontal well, the perforated interval is small. The slurry flows over the entire fracture domain with vector components in the x direction and z direction. A typical distribution of proppant is shown, whereby settling has produced a large concentration in the bottom portion of the fracture. Hence the propped fracture length is often much smaller than the created fracture length.

5.2.3 Fracture Mechanics and Propagation Criteria

The opening equation for a tensile Mode-I planar fracture in an isotropic, homogenous, three-dimensional elastic medium is a boundary integral equation. This is provided in Kossecka (1971), as shown below:

$$-p+\sigma_{h\min}=\frac{G}{4\pi(1-\nu)}\int_{\Omega}\left[\frac{\partial}{\partial x}\left(\frac{1}{r}\right)\frac{\partial W}{\partial x'}+\frac{\partial}{\partial z}\left(\frac{1}{r}\right)\frac{\partial W}{\partial z'}\right]d\Omega \qquad (5.3)$$

where

$$r=\sqrt{\left(x'-x\right)^2+\left(z'-z\right)^2} \qquad (5.4)$$

This equation relates the net fluid pressure in the fracture (Pa), $-p+\sigma_{h\ min}$, to the fracture width in the y coordinate direction (m), W, both of which vary across the fracture domain. G is the shear modulus (Pa) and ν is the Poisson's ratio of the reservoir rock.

The stress intensity factor (Pa-m$^{0.5}$), K_I, is given by:

$$K_I = \frac{G}{4(1-\nu)}\sqrt{\frac{2\pi}{r_{tip}}W} \qquad (5.5)$$

where r_{tip} is the distance to the fracture tip (m). The fracture propagation (m), Δd, is governed by the difference between the stress intensity factor and rock toughness as established by Mastrojannis *et al*. (1979):

$$\Delta d = \max\left(\Delta d_{\max}\left(\frac{K_I - K_{IC}}{K_{IC}}\right);0\right) \qquad (5.6)$$

where K_{IC} is the rock toughness (Pa-m$^{0.5}$).

5.2.4 Fluid and Proppant Transport

The overall conservation of mass of fluid and proppant is given by:

$$\frac{\partial(\rho_s W)}{\partial t} + \nabla \bullet \left(\rho_s W \overrightarrow{\langle u_s \rangle}\right) + \rho_f q_L = 0 \qquad (5.7)$$

where ρ_s and $\overrightarrow{\langle u_s \rangle}$ are the slurry density (kg/m^3) and average slurry velocity (m/s) respectively and q_L is the fluid leak-off (m/s) calculated from Carter's leak-off coefficient. More detail covering Carter's leak-off model is available in Howard and Fast (1957). Slurry properties apply to the carrier fluid and proppant together, that is, a continuum assumption is employed. The slurry velocity is related to the pressure gradient by the solution to the incompressible Navier-Stokes equation for a power law fluid flowing between two infinite plates. Using correlations for the rheological properties of a proppant-laden slurry developed by Shah (1993), based upon experiments, the transport of slurry can be accurately modeled. Shah (1993) determined that both the flow

consistency index (Pa-s^n) and the flow behavior index were functions of proppant concentration. Incorporation of the Navier-Stokes result in the above conservation of mass statement forms the pressure equation. The pressure equation is solved coupled to the fracture opening equation to yield the average slurry velocity, pressure and width across the fracture domain, among other variables.

The slurry density and slurry mass flux are given by:

$$\rho_s = (1-c)\rho_f + c\rho_p \quad (5.8)$$

and

$$\rho_s \overrightarrow{\langle u_s \rangle} = (1-c)\rho_f \overrightarrow{\langle u_f \rangle} + c\rho_p \overrightarrow{\langle u_p \rangle} \quad (5.9)$$

The relative average velocity of the two phases, proppant and fluid, due to convection is given by the CFD-DEM derived correlation $h(c, d/W)$. These each may have vector components in the x and z coordinate directions. There is an additional vector component in z coordinate direction for the proppant phase due to settling, given by the model suggested by Liu (2006). Rearrangement of the definition of slurry mass flux, $h(c, d/W)$ and $u_{settling}$ allows for solution of the average proppant velocity. With $\overrightarrow{\langle u_p \rangle}$ known, the continuity equation for proppant can be solved to determine its distribution across the fracture domain. The continuity equation for proppant is given by:

$$\frac{\partial(\rho_p c W)}{\partial t} + \nabla \bullet \left(\rho_p c W \overrightarrow{\langle u_p \rangle}\right) = 0 \quad (5.10)$$

5.3. RESULTS

5.3.1 Results Overview

The fracturing simulator described in the previous section, improved by incorporation of the CFD-DEM derived correlation for proppant transport with flow, can be used to design fracture treatments. For a given application, defined by the in-situ stress

profile, rock elastic moduli and toughness, along with leak-off properties of the reservoir, the treatment can be optimized. For two typical cases, the effect of several factors affecting proppant transport has been evaluated separately. That is, for each case a comparison has been made between the proppant distribution predicted by Stokes settling alone, corrected Stokes settling, Stokes settling with the CFD-DEM derived correlation for flow and finally corrected Stokes settling with the CFD-DEM derived correlation for flow.

5.3.2 Simulation Cases

A large barrier stress contrast limits height growth and was used in all hydraulic fracture simulation cases. The minimum horizontal stress profile and the proppant schedule used are shown below.

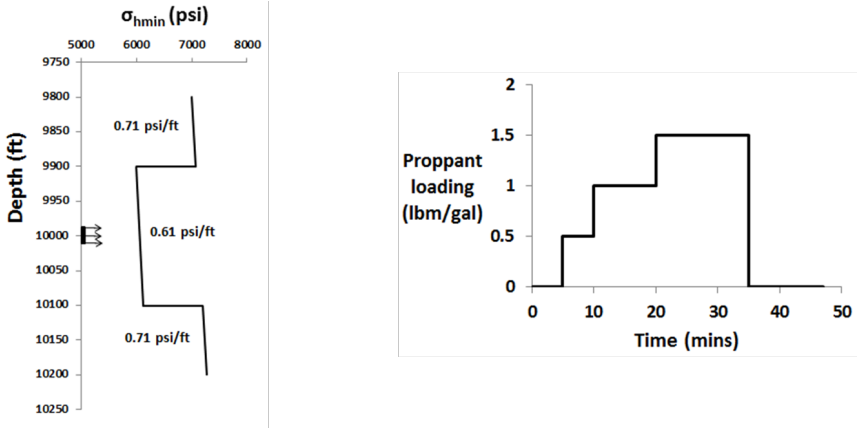

Figure 5.2. Left: Minimum horizontal stress profile versus depth. Right: Proppant loading versus time.

Table 5.1 includes all necessary inputs required by the hydraulic fracture simulator described above. Where only one value for an independent variable is included, it was used for all simulations.

Independent variable	Value (SI units)	Value (field units)
Shear modulus, G (Young's modulus)	11.03 (GPa) 27.58 (GPa)	1.6 (MMpsi) 4 (MMpsi)
Poisson's ratio, ν	0.25	
rock toughness, K_{IC}	1.099MPa-$m^{0.5}$	1000psi-$in^{0.5}$
height	60.96m	200ft
proppant diameter, d	0.0003	40/70 mesh proppant
proppant density, ρ_p	2650kg/m^3	165 lbm/ft^3
fluid density, ρ_f	1000kg/m^3	62.4 lbm/ft^3
fluid rheology, μ	0.001Pa-s	1cP slickwater
injection rate (bi-wing, hence half into single fracture)	0.03975, 0.06625m^3/s	15, 25bbl/min
leak-off, C_L	3.935x10^{-6}m/$s^{0.5}$	0.0001ft/$min^{0.5}$

Table 5.1. Hydraulic fracture simulation parameters.

The specified injection rate per bi-wing fracture is representative of one quarter of a typical overall stimulation injection rate, reflecting common practice to simultaneously stimulate four clusters. The two overall injection rates modeled are 100 and 60bbl/min. 40/70 proppant was included as per the schedule in Figure 5.2. Slickwater fluid rheology is well characterized by a Newtonian fluid with a viscosity of 1cP. The value used for Carter's leak-off coefficient was 0.0001ft/$min^{0.5}$ in all cases.

5.3.3 Final Proppant Distribution

5.3.3.1 Final Proppant Distribution with Injection at 25bbl/min

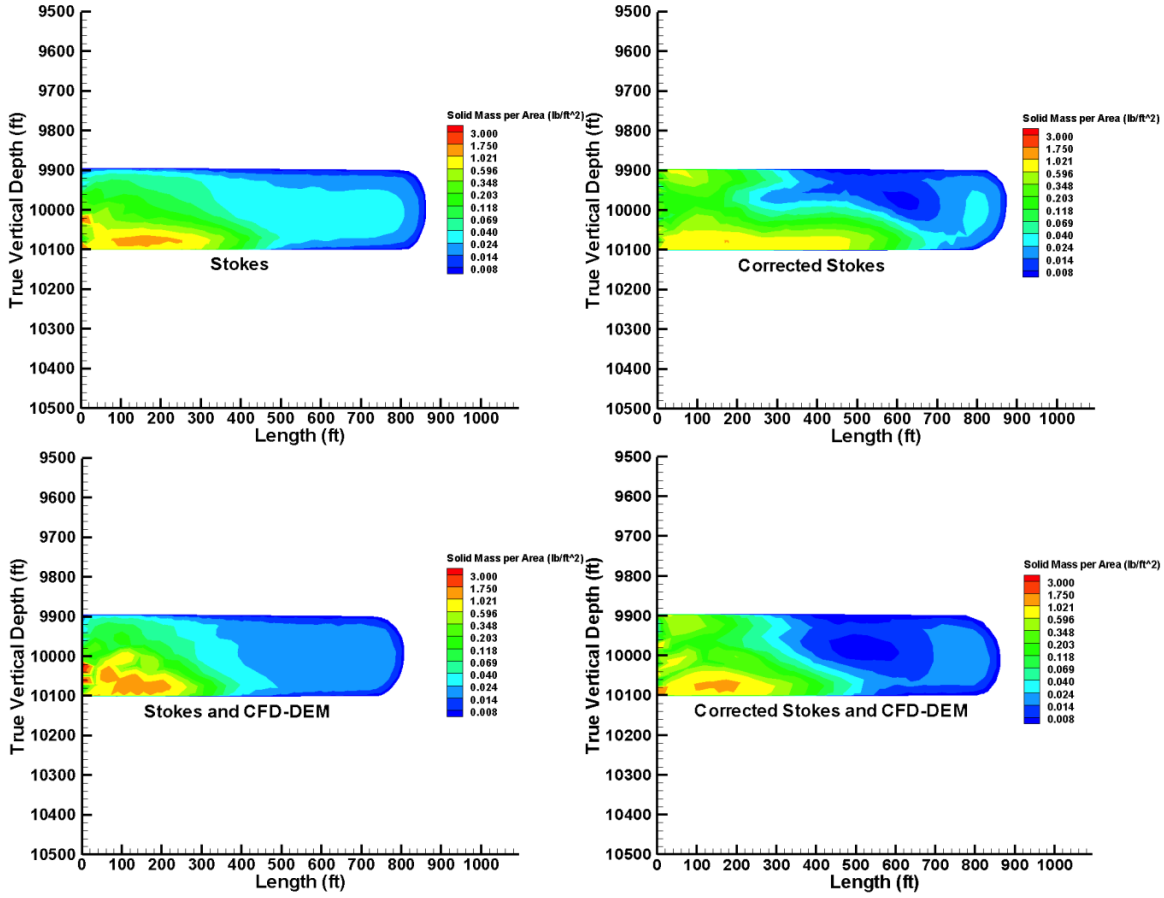

Figure 5.3. Final proppant distribution with injection at 25bbl/min. Top left: Stokes settling. Top right: Corrected Stokes setting. Bottom left: Stokes settling and CFD-DEM correlation *h(c, d/W)*. Bottom right: Corrected Stokes settling and CFD-DEM correlation *h(c, d/W)*.

The proppant distribution at the end of pumping for a case with an injection rate of 25bbl/min into one bi-wing fracture is shown in Figure 5.3. Comparing first the top left and top right panes, it is apparent that the effective (or propped) fracture length is smaller if the Stokes settling velocity is assumed versus the Stokes settling velocity corrected with the correlation proposed by Liu (2006). Comparing the effective fracture

length with the CFD-DEM correlation applied versus not applying it, using corrected Stokes settling as shown in the top right and bottom right panes, the effective fracture lengths are significantly reduced. If Stokes settling is assumed as shown in the top left and bottom left panes, there is less reduction in the effective fracture length due to the inclusion of the CFD-DEM correlation. However, this is a less accurate settling model as the proppant settles at a particle Reynolds number outside of the Stokes regime. For clarity, the propped width of each fracture, averaged over its height, is presented in Figure 5.4.

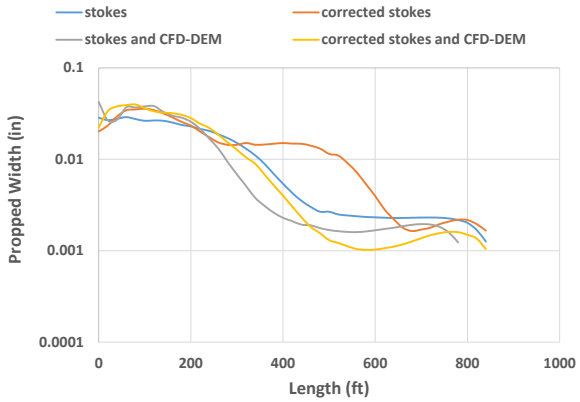

Figure 5.4. Final average propped fracture width versus length with injection at 25bbl/min.

The average propped width of the fracture versus length shown in Figure 5.4 indicates that the effective fracture length is reduced by inclusion of the CFD-DEM correlation, whether the settling is assumed to follow Stokes' law with or without the correction proposed by Liu (2006).

5.3.3.2 Final Proppant Distribution with Injection at 15bbl/min

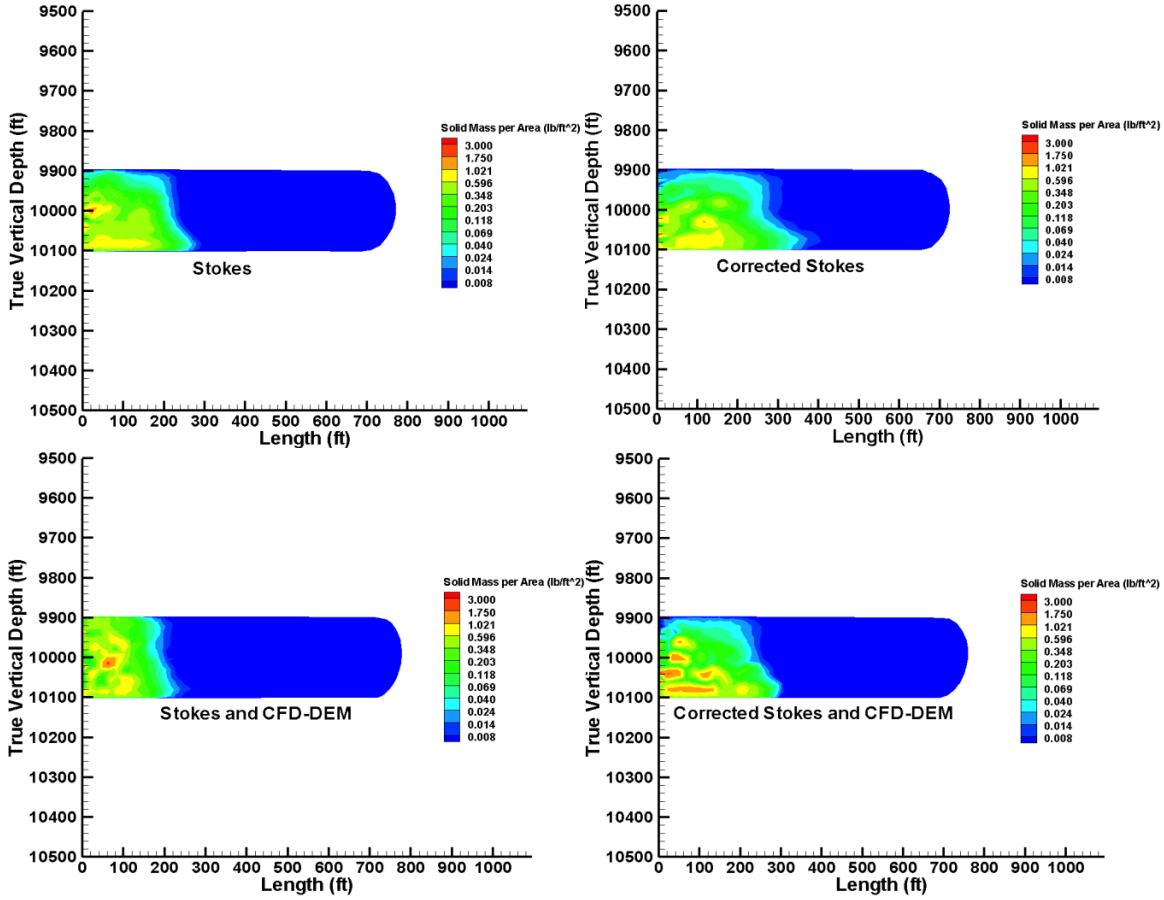

Figure 5.5. Final proppant distribution with injection at 15bbl/min. Top left: Stokes settling. Top right: Corrected Stokes setting. Bottom left: Stokes settling and CFD-DEM correlation *h(c, d/W)*. Bottom right: Corrected Stokes settling and CFD-DEM correlation *h(c, d/W)*.

A case using an injection rate of 15bbl/min into one bi-wing fracture was simulated with the proppant distribution at the end of pumping shown in Figure 5.5. Comparing the effect of application of the CFD-DEM derived correlation, while assuming the more accurate corrected Stokes settling model as shown in the top right and bottom right panes, there is a small reduction in the effective fracture length due to the CFD-DEM correlation. The reduction in the effective fracture length is less than for the

case with injection at 25bbl/min as convection plays a smaller part in the overall transport of proppant with injection at 15bbl/min. For clarity, the propped width of each fracture, averaged over its height, is presented in Figure 5.6.

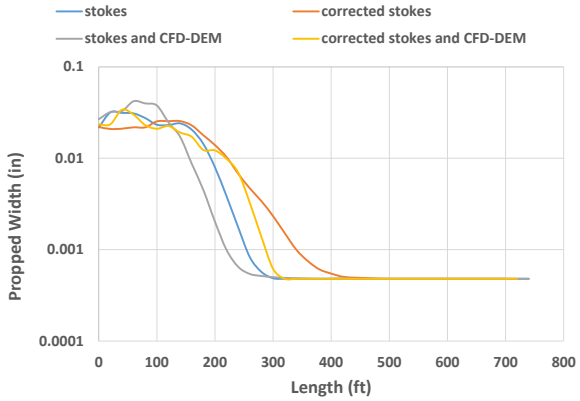

Figure 5.6. Final average propped fracture width versus length with injection at 15bbl/min.

The small reduction in the effective fracture length due to inclusion of the CFD-DEM correlation is apparent on examination of the results shown in Figure 5.6.

5.4 CONCLUSIONS

The CFD-DEM simulation results clearly demonstrate that the average proppant velocity is generally lower than the average fluid phase velocity. The relative velocity of the two phases is a linearly proportional function of the volumetric concentration of proppant. There is an exception to this for low proppant concentrations at large ratios of proppant diameter to slot width, though it is uncommon for this to be case in hydraulic fracturing applications.

The CFD-DEM results have been incorporated in UTEFRAC-3D via a simple correlation. The reduced proppant velocity with increased concentration leads to a reduction in propped fracture lengths compared to predictions made with simplified

proppant transport assumptions commonly used in industry. The reduction in length is greater for larger injection rates as transport by convection is the more significant transport mechanism in these cases. The improvement of the proppant transport calculation made in UTEFRAC-3D allows for more accurate engineering optimization of fracture treatments, with predictions closer to typical results available from history matching field data.

Chapter 6: Particle Transport of Non-Dilute Suspensions in Branched Slots

The simulation approach detailed in Chapter 2 has been applied to the transport of particles in a branched slot. The proportion of particles transported into the branch has been determined for a wide variety of domain geometry and proportion of fluid flowing into the branch, among other relevant factors.

6.1 Introduction

A hydraulic fracture is typically assumed to propagate perpendicular to the minimum horizontal stress in a homogeneous reservoir where both horizontal stresses are smaller than the vertical stress. However, rock deviates from this simplifying assumption of homogeneity to various degrees. Discontinuities in rock include natural (pre-existing) fractures, amongst many others across various scales. Interaction between a propagating hydraulic fracture and natural fractures has been extensively studied through physical experiments. Early laboratory scale experimental work by Lamont and Jessen (1963) and Daneshy (1974) examined the propagation of a hydraulic fracture in a sample of rock containing a natural fracture. Lamont and Jessen (1963) found that the natural fracture was bypassed by the hydraulic fracture in all cases considered, while Daneshy (1974) identified some cases where the hydraulic fracture was arrested. The cases in which the hydraulic fracture was arrested were attributed to the relative scale of the two fractures. Blanton (1986) conducted similar experiments and identified the angle of approach between the hydraulic and natural fracture and the differential stress as the primary controlling factors for propagation behavior. Small angle of approach, 30°, and low differential stress tended to result in diversion of the hydraulic fracture along the natural

fracture. Conversely, larger angles of approach, 60° and 90°, resulted in no diversion of the hydraulic fracture from propagating perpendicular to the minimum horizontal stress, if the differential stress was sufficiently large. Blanton (1986) proposed criteria allowing the conditions under which diversion occurs to be identified. Warpinski and Teufel (1987) conducted both laboratory and field scale experiments. The latter were examined by excavation of the hydraulically fractured rock. Observations of rock after hydraulic fracturing demonstrated multi-stranded fracture propagation. The results of laboratory experiments demonstrated similar trends to those reported by Blanton (1986) in terms of propagation behavior as a function of angle of approach and differential stress.

Experimental studies of hydraulic and natural fracture interaction illustrate that there are a wide range of conditions under which a hydraulic fracture is not diverted by the presence of a natural fracture. However, the natural fracture may subsequently dilate and accept fluid. This results in an intersection that, at a small scale, may be considered a branched slot. This leads to many branches in the fracture network into which particles may be transported. However, the proportion of particles entering each branch is not necessarily the same as the proportion of fluid. The particle transport efficiency for particles exiting a wellbore casing into perforations (small holes in the well casing), was determined experimentally by Haynes and Gray (1974). They found particles to be transported more efficiently with increasing flow rate, decreasing particle size and concentration. A similar study by Gruesbeck and Collins (1982) showed the particle concentration to be unimportant, in contrast to the results of Haynes and Gray (1974). Gruesbeck and Collins (1982) found particles to be transported in smaller proportion than the proportion of fluid accepted by the perforations for lower viscosity fluids. In addition, particles were found to form bridges in cases where the perforation was only a small multiple, two or three, of the particle diameter.

While there is no reason to doubt the validity of the results of the two experimental particle transport studies, the geometry and scale of the system examined is very different to that expected at a hydraulic and natural fracture intersection. In this case the fractures have a small width, in some cases approaching the size of the particles transported through them. In contrast, a wellbore is much larger. As such, the results above cannot be directly applied to the problem of interest in this research.

This study directly solves the motion of spherical solid particles in a fluid. This is achieved through calculation of the velocity and pressure across the fluid domain surrounding the particles. Subsequently, the forces exerted by the fluid on the particles is determined directly and used to calculate their trajectories. While the numerical approach used in this research is different, this general simulation approach was pioneered by Hu *et al*. (1992) and subsequently applied by Feng *et al*. (1994), to study two-dimensional cylinders settling and moving in Poiseille flow, respectively. Yang *et al*. (2005) applied a similar approach to study a three-dimensional spherical particle in tube Poiseuille flow. This approach has not previously been applied to the problem of interest in this research, that of suspension flow in bifurcating slots. Simulation cases have been run to determine the proportion of particles entering a branch of various aperture and orientation, subject to a range of slot flow Reynolds number at the inlet and proportion of fluid entering the branch. The effect of fluid rheology, particle concentration, size and density has also been quantified.

6.2 Application to Flow in a Branched Slot

6.2.1 Simulation Domain and Boundary Conditions

A schematic of the simulation domain is shown in Figure 6.1.

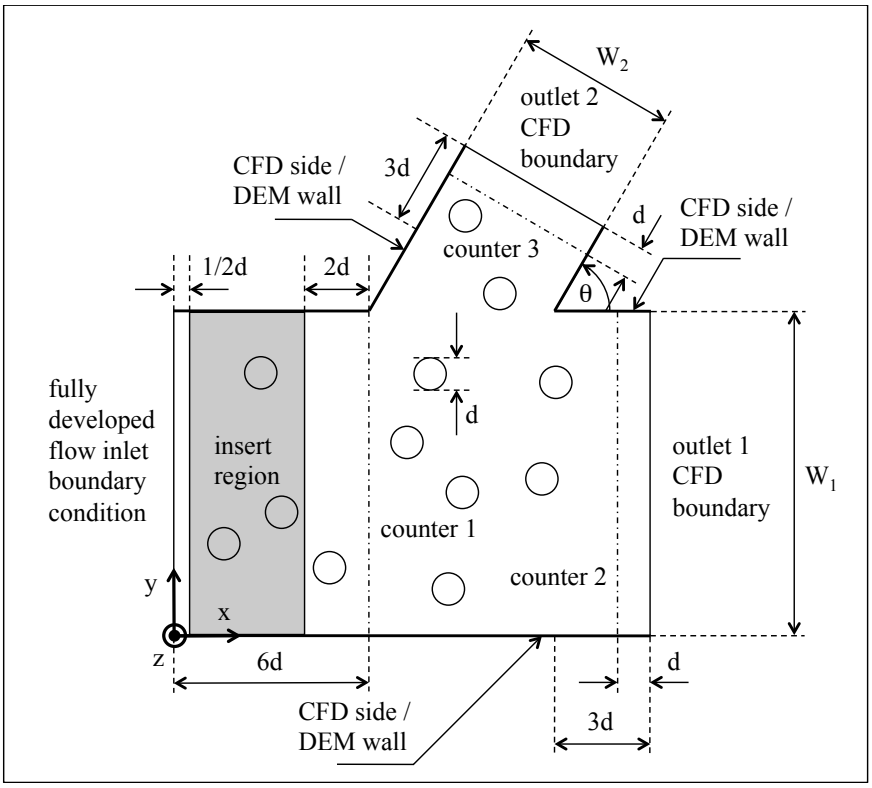

Figure 6.1. Simulation domain.

The coupled CFD-DEM approach involves two representations of the physical system and as such the relevant equations are each solved across two separate domains, which are not necessarily coincident. In this study, the CFD and DEM domains share the same planar boundaries in the z coordinate direction (out of the page), with a height, H, of 2 particle diameters, d. However, in the x and y coordinate directions the DEM domain is larger than the CFM domain due to a requirement of the DEM code used, which specifies a minimum domain volume. This is a practical requirement rather than one driven by the physical system modeled. The x and y boundaries of the CFD domain are shown in Figure 6.1 and consist of a main slot and branch set at a particular angle to the main slot, θ. The main slot and branch can take different widths, W_1 and W_2, respectively.

The simulation approach applied involves considerable numerical expense and run time constraints require a small domain to allow for production of sufficient simulation data. As such, the lengths of each portion of the slot from the intersection are relatively small multiples of *d*. While the DEM domain is larger than the CFD domain, the particles are restricted to move within a subset of the CFD domain by walls and the insertion and deletion approach used, as detailed below.

The boundary conditions applied to the CFD domain are as follows:

At the CFD *inlet* and *outlet 1*: fully developed slot flow.

In the laminar flow regime this condition is slot Poiseuille flow, with the scalar components of the fluid velocity vector and the pressure specified by

$$u_{fx}(y) = (1-\beta) * u_{fx\,max}\left\{1-\left[\frac{|y-B|}{B}\right]^{1/n+1}\right\} \qquad u_{fy}=0 \qquad u_{fz}=0 \qquad \frac{\partial p}{\partial x}=0 \tag{6.1}$$

where β is the proportion of fluid flowing into the branch and is within the range $0 \le \beta \le 1$, $u_{fx\,max}$ is the maximum value of the *x* component of the fluid velocity, *B* is half the main slot width, *n* is the fluid behavior index. The expression for u_{fx} has been obtained analytically from conservation of momentum considerations for a power-law fluid. This is necessary for extension of the research to cases of shear thinning fluids, which are included in this work. With reference to the boundary condition expression above, β is always zero at the inlet and greater than zero at *outlet 1*.

In the turbulent flow regime, the time average velocity profile across a slot is commonly described by a logarithmic law, see standard texts such as Pope (2000). The expression for u_{fx} with *y* within the range $0 < y \le B$ is provided below.

$$u_{fx}(y) = \frac{u_\tau}{\kappa}\ln\left(\frac{y}{B}\right) + u_{fx\,max} \qquad u_{fy}=0 \qquad u_{fz}=0 \qquad \frac{\partial p}{\partial x}=0 \tag{6.2}$$

where κ is the von Karman constant, assumed to be 0.41 and u_τ is the friction velocity (m/s). For y within the range $B < y \le 2B$ a similar expression is used to produce a symmetric velocity profile. This expression is often termed the 'velocity defect law' as the logarithmic term defines the difference between the local time average velocity and the maximum time average velocity, which occurs at the center of the slot. The other two scalar components of the time average velocity, $u_{f\,y}$ and $u_{f\,z}$, are the same as for slot Poiseuille flow and equal to zero. Similarly, the pressure gradient in the direction of flow is zero. The friction velocity is also required to satisfy:

$$\frac{u_{f\,x\,max}}{u_\tau} = \frac{1}{\kappa}\ln\left[\mathrm{Re}_0\left(\frac{u_{f\,x\,max}}{u_\tau}\right)^{-1}\right] + B_1 \qquad (6.3)$$

where B_1 is a constant assumed to take the value of 5.2. The notation used in the available literature often uses B for this particular constant, however in this context B is used for the main slot half width. Re_0 is the Reynolds number calculated in terms of the maximum time average fluid velocity and a characteristic length of B.

Since the shape of the velocity profile is a function of Reynolds number, the expression applied at the CFD *inlet* cannot simply be multiplied by (1-β) as done for laminar flow at *outlet 1* but a separate calculation of $u_{f\,x\,max}$ and u_τ is required.

At the CFD *outlet 2*: constant pressure

$$\frac{\partial u_{f\,x}}{\partial x} = 0 \qquad \frac{\partial u_{f\,y}}{\partial x} = 0 \qquad \frac{\partial u_{f\,z}}{\partial x} = 0 \qquad p = 0 \qquad (6.4)$$

At all the CFD *sides*: no slip condition

$$u_{f\,x} = 0 \qquad u_{f\,y} = 0 \qquad u_{f\,z} = 0 \qquad \frac{\partial p}{\partial x} = 0 \qquad (6.5)$$

At the planar CFD boundaries in z: cyclic pairing

$$u_{f\,x}\Big|_{z=0} = u_{f\,x}\Big|_{z=H} \qquad u_{f\,y}\Big|_{z=0} = u_{f\,y}\Big|_{z=H} \qquad u_{f\,z}\Big|_{z=0} = u_{f\,z}\Big|_{z=H} \qquad p\Big|_{z=0} = p\Big|_{z=H} \qquad (6.6)$$

This boundary condition, cyclic pairing, represents an infinitely tall domain.

The setup used within the DEM domain is as follows:

There is an *insert region* (shown in grey in Figure 6.1), a volume into which particles are introduced at random non-overlapping positions to satisfy a specified insert mass rate (kg/s), $\dot{m}_{insert}$. This is determined from:

$$\dot{m}_{insert} = \left\langle u_{fx} \right\rangle (1-c)\, cA\rho_p \qquad (6.7)$$

where $\langle u_{fx} \rangle (1\text{-}c)$ (m/s) is the modified average fluid velocity in the main branch prior to the intersection, c is the volumetric particle concentration required, A (m^2) is the cross sectional area of the main branch, $W_1 \times H$, and ρ_p (kg/m^3) is the particle density. Each particle is inserted with the x component of its velocity initially equal to the modified average fluid velocity in the main branch prior to the intersection, while the other two velocity components, in the y and z coordinate directions, are zero. In addition to the particles continuously inserted into the domain, there is initially one particle placed at the center of the main slot prior to the intersection. This is done so that the DEM code does not produce an error on determining that there are zero particles in the system initially and is not related to modeling the physical system.

In this work, a counter is defined by four points in the Cartesian coordinate system with two placed on either side of the slot at each wall, forming a rectangular shape on a plane normal to the slot walls. The counter records the cumulative number and mass of particles passing though it. There are three counters placed in the simulation domain, one prior to the branch, one after the branch and one in the branch. *Counter 2* and *counter 3* delete particles that have passed through them.

Walls are placed as shown in Figure 6.1.

Periodic pairing is used at the *top* and *bottom* of the DEM domain.

6.2.2 Data Analysis

An example of the cumulative mass of particles recorded passing through each counter is presented in Figure 6.2.

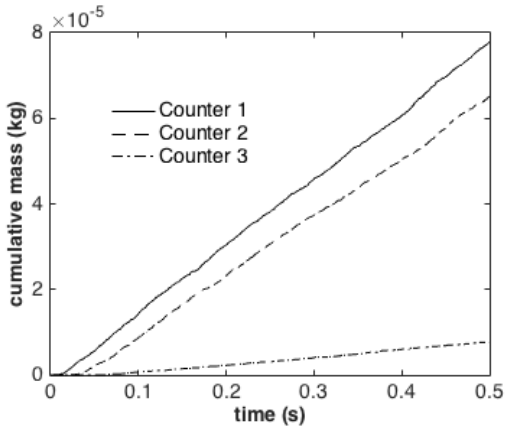

Figure 6.2. Cumulative mass recorded at each counter versus time.

From the simulation data recorded by each counter, a dimensionless quantity termed the 'particle transport coefficient', *PTC*, has been calculated. This quantity is defined as the proportion of particles transported into the branch normalized by the proportion of fluid flowing into the branch, given by:

$$PTC = \frac{\dot{m}_3}{\dot{m}_1}\frac{1}{\beta} \qquad (6.8)$$

where $\dot{m}_3$ and $\dot{m}_1$ are the mass rates (kg/s) determined from the cumulative mass recorded by *counter 3* and *counter 1*, respectively. Each mass rate has been determined using a linear trend fitted by a process of least squares regression to the simulation data from the time at which the first particle arrives at *counter 3*.

6.2.3 Domain Size, Grid Refinement, Time Step Considerations and Particle Seeding

As noted above, the method is computationally expensive. This necessitates efficient design of the simulation setup to enable production of sufficient data within run

time constraints. Small domain size and sparing refinement of the CFD grid achieves this aim. While the domain needs to small enough to enable enough simulation data to be produced, certain minimum requirements need to be met. One such requirement is that the translational velocity of each particle is a close approximation to steady state, given its particular position in the slot, prior to arrival at the branch. This requires the length of the main slot between the *insert region* and the branch to be greater than a certain value. Particles inserted closest to the branch travel only 2.5*d* before arriving at the branch. To determine if this is sufficient, two checks were made. The first check required determining the velocity transient of a single particle accelerating from an initial x velocity equal to the average fluid velocity (the initial condition used for all particles inserted) at the center of a slot in Poiseuille flow, using the simulation approach detailed above. This velocity transient reveals that the particle reaches approximately 90% of the steady state velocity after translating 2.5*d*. It is important to note that this is the smallest distance a particle translates from the insert region to the branch, particles can travel up to 5*d* if inserted at the furthest location within the *insert region*, doing so more closely approximates steady state. That is, the most inaccurate translation velocity obtained for particles in the middle of the slot is only 10% from the true steady state value. The second check involved the construction of a simulation domain where the minimum distance particles travel is 8.5*d* from the *insert region* to the branch, with all other dimensions and parameters remaining the same. Comparison of the transport coefficient determined from the two simulation domains agreed within 10%. The larger simulation domain case produced approximately half the simulation data as the smaller domain, which is a significant drawback for accurate calculation of the transport coefficient for smaller values of the proportion of fluid flowing into the branch, as discussed in detail

below. Since reasonable agreement between the results was found, the smaller domain has been used for all subsequent simulations.

The original static CFD grid used consists of ten grid blocks across both the main slot and the branch. This provides sufficient resolution of the flow field in the absence of particles. Using such a grid for the branch results in a very refined mesh in the x coordinate direction across the intersection of the main slot for cases with a small branch width. Since such refinement is numerically expense and not required in the main slot prior to and after the branch, grading has been applied with a cell-to-cell expansion ratio of greater than 0.8 in all cases, following standard CFD practice. The main slot is ten particle diameters wide for all simulations, resulting in CFD grid blocks of one particle diameter in length. This is a relatively coarse grid for this particular simulation approach, which requires adequate resolution of the flow field surrounding particles. Two steps of dynamic mesh refinement have been used to provide greater resolution of particles and the fluid flow around them. Each refinement step splits a grid-block in two in each Cartesian coordinate direction. The end result is four grid blocks per particle across the slot, a ratio demonstrated to provide reasonable accuracy when applied to a particle settling as described in Hager *et al*. (2011). Grid blocks are one third of a particle diameter in length in the z coordinate direction. Discussion of adequacy of the grid used is provided below.

A coupling interval between the two codes, OpenFoam and LIGGGHTs, allows a predetermined number of smaller DEM time steps to be taken prior to the CFD solver solution of the fluid flow. Since a rigorous criteria for selection of an appropriate coupling interval is not available in the literature, a process of trial and error has been used. In general, simulation cases at larger slot flow Reynolds number at the inlet require a smaller coupling interval. Each code does have its own stability criteria. For the DEM

solver, these are the Raleigh time and Hertz time. For the CFD solver this is the Courant number, a measure of the magnitude of the local fluid velocity relative to the size of the grid-block for a particular time step, is the relevant criteria for CFD simulation stability. All of these considerations were satisfied through the simulation parameters used.

The appropriate slot flow Reynolds number, Re_s, for a power-law fluid, based on a characteristic length of the hydraulic diameter and specified at the main branch prior to the intersection, is:

$$Re_s = \frac{(2W)^n \left[\langle u_{fx} \rangle (1-c)\right]^{2-n} \rho_f}{8^{n-1}\left(\frac{3n+1}{4n}\right)^n \eta_c} \qquad (6.9)$$

The factor of (1-c) appears as a result of using the same fluid velocity boundary condition at the inlet for simulation cases at several different concentrations. The above expression is considerably simplified in the case of a Newtonian fluid.

Particles are inserted into the domain in the *insert region*. Doing so requires specifying a 'seed', a number used to determine the sequence of particle insertion positions. A comparison was made between three sets of simulations, for which all parameters are the same except for the particle insertion seed used. The parameters are given in Table 6.1.

Parameter	
d/W_1	0.1
d/W_2	0.2
θ (degrees)	60
d (m)	0.0004
c	0.15
Re_s	1000
β	0.2, 0.1, 0.05, 0.04, 0.03, 0.02, 0.01, 0.005
μ (Pa-s)	0.001
ρ_f (kg/m^3)	1000
ρ_p (kg/m^3)	2650

Table 6.1. Branched slot simulation parameters.

The proportion of fluid flowing into the branch has been varied and takes a value between 0.2 and 0.005 for each of the eight simulation cases. The result of running each of the cases is presented in terms of the particle transport coefficient, in Figure 6.3.

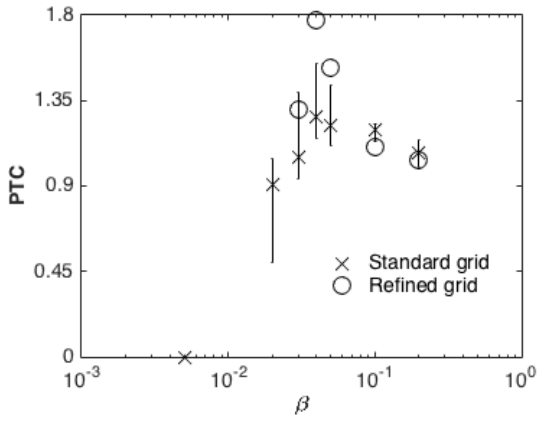

Figure 6.3. Particle transport coefficient versus the fraction of fluid flowing into the branch for different particle seeds and grids.

The error bar plot shown in Figure 6.3 shows the smallest, middle and largest value of *PTC* determined from the three simulation cases, each run with a different seed but otherwise identical parameters. The length of the error bar, representing the range of *PTC*, generally becomes larger with smaller β. The reason for this is as follows. While

the domain size, CFD grid and coupling interval have each been selected to provide as much simulation data as possible, only approximately 0.5s is produced given the run time constraints and the parameters listed in Table 6.1. Over the course of ~0.5s, approximately 1000 particles are seeded in the *insert region*. For *PTC* in the range 0.2 to 0.02, it takes between approximately 10% and 30% of the 0.5s of the simulation duration for particles to arrive at *counter 3*. For β of 0.02, the maximum and minimum total number of particles transported into the branch is 15 and 8 particles, respectively. In contrast, for β of 0.2, there are 179 and 163 particles in total corresponding to the maximum and minimum totals. While the range in the total number of particles is in fact larger for β of 0.2 compared to that for β of 0.02, there are substantially more particles over which to calculate the average mass rate. Nonetheless, as long as the range in the estimate of *PTC* is understood, there is value in reporting it for small values of β. However, so few particles arrived during the cases for which β is 0.01 that a meaningful average was not possible. In these cases the *PTC* was not reported. Finally, while even fewer particles arrived for the cases with β of 0.005 than the β of 0.01 cases, these have been reported as a *PTC* of zero since the one or two particles corresponds to a *PTC* of less than 0.5. Throughout this research such a small number of particles arriving at *counter 3* will be reported as a *PTC* of zero and a note made as to whether this is the result of zero particles actually observed or simply so few that the *PTC* value if calculated would be less than 0.5.

The same set of eight simulation cases, for which the parameters are shown in Table 1, have been run with a refined grid. This grid uses twenty grid blocks across the main slot in place of the ten used for the standard grid. Using such a grid produces only approximately 0.2s of data versus the ~0.5s produced using the standard grid. This is the motivation for using a relatively coarse grid as standard. As a result, it is only possible to

report *PTC* from simulations with β in the range 0.2 to 0.03. For β of 0.02 and smaller there are too few particles recorded from which a meaningful average can be determined but also too little simulation data to be able to justifiably report a *PTC* of zero following the criteria detailed above. From the *PTC* results available, the trend observed is the same as that for the standard grid, a peak in *PTC* corresponding to β of 0.04. The *PTC* values do not always fall within the error bars, though they should not be expected too as these are a simple measure of the range observed in three simulations and not true measures of the variation in the population. A comparison between the standard and refined grid was also made with a volumetric concentration of 0.05, in place of c equal to 0.15 used for the simulation results presented in Figure 6.3, since this parameter results in significantly more simulation data produced. While approximately a factor of three times the simulation data is available from these simulations, the mass rate is reduced by approximately one third and as a result the same limitation in terms of a small cumulative number of particles recorded is evident. More detail on the total number of particles counted is available in Appendix A.

6.3 RESULTS

6.3.1 Effect of Branch Width

The simulation approach adopted and the setup developed for application to a branched slot has been detailed above. The effect of domain geometry upon *PTC* has first been examined through simulations with different branch widths, W_2, selected such that d/W_2 is between 0.2 and 0.95. The values of the other parameters are identical to those included in Table 6.1. The simulation data has been processed and the results are presented in Figure 6.4.

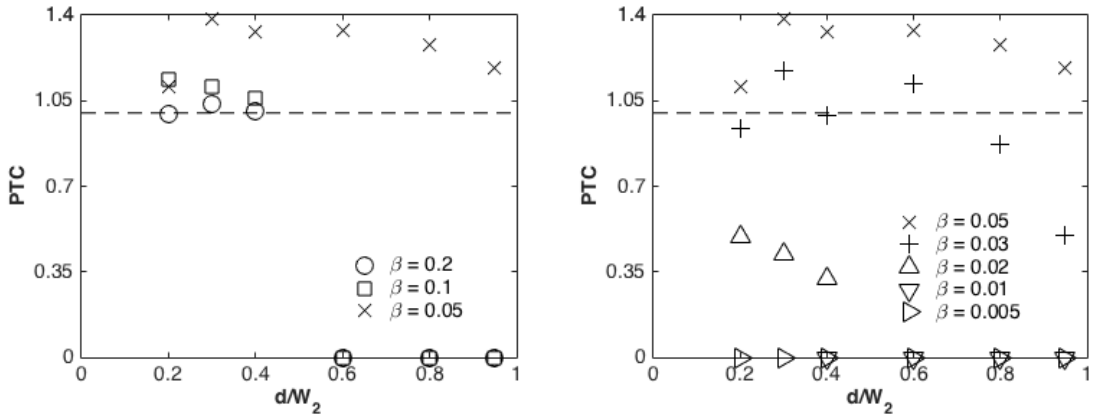

Figure 6.4. Particle transport coefficient versus particle diameter to branch width ratio. Left: Fraction of fluid flowing into the branch between 0.2 and 0.05, Right: Fraction of fluid flowing into the branch between 0.05 and 0.005.

While simulation cases have been run with β equal to 0.04, the results are very similar to those at β equal to 0.05 and as such have been omitted for clarity of presentation in Figure 6.4. There are several cases for which *PTC* is greater than one. A dashed line is shown at *PTC* equal to one in this figure to aid identification of these cases. The results shown in Figure 6.4 demonstrate that *PTC* varies as both a function of d/W_2 and β. Examining the left pane, for d/W_2 equal to 0.6 and larger, when β is equal to 0.2 and 0.1, a small number of particles were recorded at *counter 3*, followed by the formation of a stable particle bridge which prevented further particle transport. In each of these six cases the branch remained 'jammed' for the remainder of the simulation and as such the value of *PTC* reported is zero. With a small amount of simulation data available in each case, ~0.5s, the formation of a particle bridge within this time may be considered an instantaneously jammed state and *PTC* is zero for practical purposes. The remaining simulation results presented in the left pane did not exhibit particle jamming. There is an increase in *PTC* with decreasing β over the range considered (β between 0.2 and 0.05). The values of *PTC* are reasonably flat across the range of d/W_2 considered, with a slight

decrease in *PTC* with increasing d/W_2 in most cases. That is, smaller W_2 results in smaller *PTC*.

The results presented in the right pane of Figure 6.4 contrast with the results presented in the left pane, with *PTC* decreasing as β decreases over the range presented (β between 0.05 and 0.005). Considering the results in both panes of Figure 6.4 together demonstrates that there is a peak in the particle transport coefficient when the proportion of fluid flowing into the branch is approximately equal to 0.05.

Decreasing *PTC* with increasing d/W_2 is observed and is more pronounced with smaller β. No more than 5 particles were observed in the results of simulations with β equal to 0.02 and d/W_2 equal to 0.6, 0.8 and 0.95. The calculated *PTC* for these cases is in the range 0.1 to 0.2, but considering the uncertainty in the calculation associated with such small numbers of particles, these have not been reported in Figure 6.4. A similar result is found for β equal to 0.01 and d/W_2 equal to 0.2 and 0.3 and these are also not reported. All simulations with β equal to 0.005 demonstrated a *PTC* of zero, with zero or at most one particle recorded at *counter 3*. Larger d/W_2 is equivalent to smaller W_2 for a given d, thus a smaller branch width has been observed to reduce *PTC* in most available comparisons.

The value of β at which *PTC* equals zero, β_0, has been plotted versus d/W_2 and is shown in Figure 6.5.

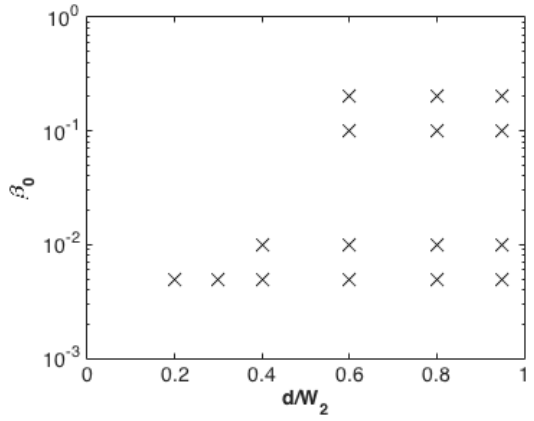

Figure 6.5. Proportion of fluid flowing into the branch at zero particle transport coefficient versus particle diameter to branch width ratio.

The results shown in Figure 6.5 demonstrate that *PTC* is zero for both large and small β. For β equal to 0.1 and 0.2, jamming is the mechanism responsible, while for β of 0.005 and 0.001, particles simply bypass the secondary branch and are transported with flow along the main branch in a continuous manner.

6.3.2 Particle Jamming

As noted above, the formation of stable particle bridges preventing subsequent particle transport into the branch was observed in 6 simulations. For these cases, the value of β was equal to 0.2 and 0.1 and d/W_2 was equal to 0.6, 0.8 and 0.95. The location and buildup of particles for the simulation case with value of β equal to 0.2 and d/W_2 equal to 0.8 is examined in Figure 6.6.

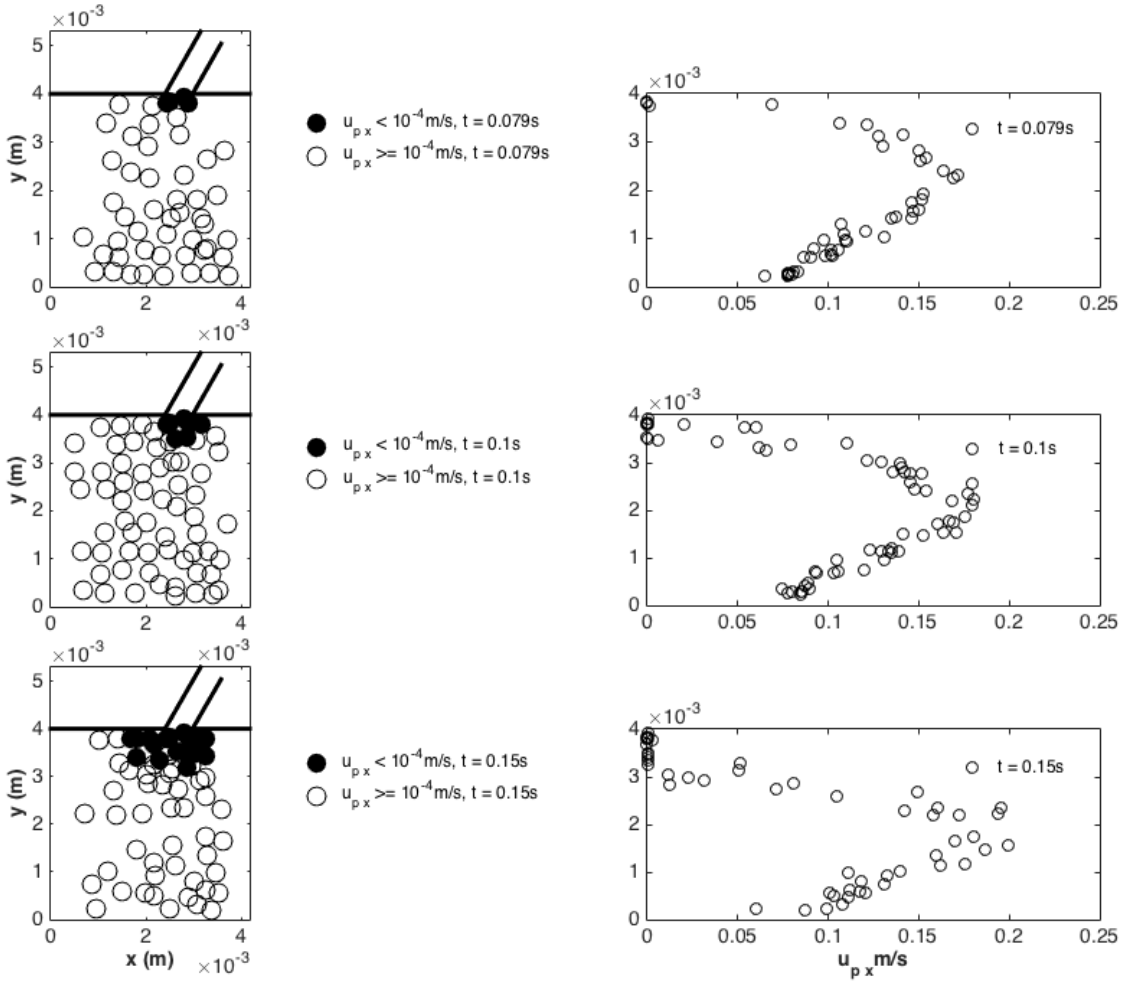

Figure 6.6. Particle locations and velocities. Top to bottom shows three states of the system as it evolves with time. Left: Particle location (*x* and *y* coordinate) in the main branch. The main slot walls and branch are shown as a thick solid line. Right: Particle location in the *y* coordinate direction versus *x* component of velocity.

The top two panes of Figure 6.6 show the state of the simulated system at 0.079s, which is directly after *counter 3* registered the last particle transported into the branch. That is, the first jammed state of the system. There are a total of 50 particles present at this time, with the magnitude of the *x* component of velocity of each of 4 particles less than 10^{-4}m/s, shown as filled circles in the left pane. This velocity, 10^{-4}m/s, has been used

as an indicator of jammed particles. While this is an arbitrary criterion, at this time in the evolution of the system, particles transported at greater velocities are each travelling at least one order of magnitude faster, as shown in the right pane. The 4 jammed particles are deposited in the main branch at the inlet to the secondary branch and not in the secondary branch itself.

The middle panes show the evolution of the system at 0.1s. At this time 7 particles are jammed, including the original 4 which were jammed at 0.079s. At this time, two layers of particles have been deposited in the *y* coordinate direction. There are a total of 67 particles in the system, which is more than at 0.079s, as insertion has continued at the same rate whilst accumulation has also occurred since this time. The particle velocity distribution at 0.1s shown in the right pane exhibits a larger maximum velocity and less symmetry than at 0.079s resulting from the larger fluid velocity now present in unjammed portion of the main branch.

The state of the system at 0.15s is shown in the bottom panes. A total of 17 particles are jammed, out of a total of 63. The particle bridge includes the 7 jammed at 0.1s and new additions to the particle bridges, which are both longer in the *x* coordinate direction and three layers thick in the *y* coordinate direction. As a result there has been a further increase in the maximum particle velocity in the unjammed portion of the branch due to larger fluid velocity.

6.3.3 Peak Particle Transport Coefficient

The results presented in Figure 6.4 demonstrate that there is a peak in *PTC* for β equal to 0.05. The peak value of *PTC* is greater than one and as large as approximately 1.4, when considering the results shown in Figure 6.4. This is a result of the distribution of particle velocities across the main slot prior to the intersection and the difference in

lateral fluid to particle forces acting to transport particles into the branch for different values of β.

This result was examined in particle scale detail by analysis of two simulations with different values of β, 0.2 and 0.05. The values of the other parameters are identical to those presented in Table 6.1, except for the Newtonian fluid viscosity (Pa-s), μ, of 0.0005Pa-s and Re_s of 2000. The calculated values of *PTC* are 1.0 and 1.3 for β equal to 0.2 and 0.05, respectively. For each simulation, the position and velocity of 200 particles passing through *counter 1* (located in the main slot immediately prior to the intersection as shown in Figure 1) were compared with the final position of each particle, determined by whether or not it arrived at *counter 3* (located in the branch). The results are presented in Figure 6.7.

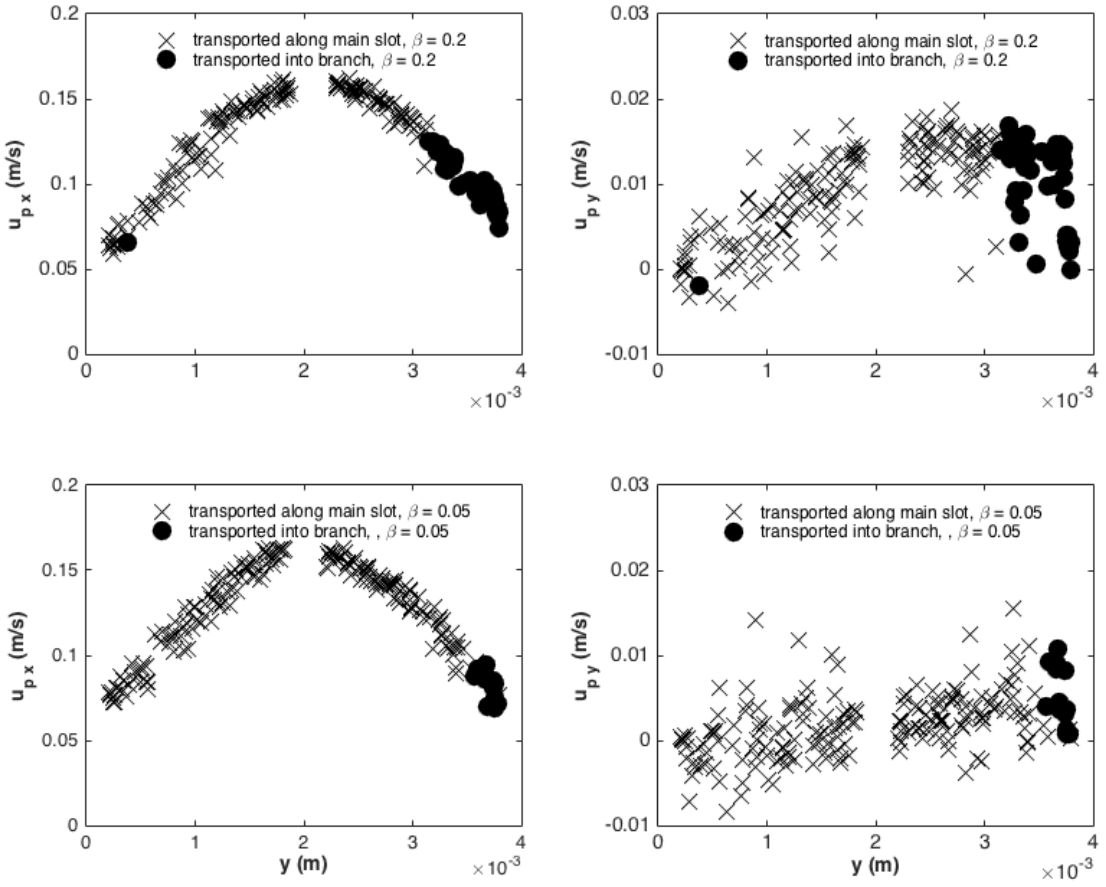

Figure 6.7. Particle velocities in the *x* and *y* coordinate directions at *counter 1*. The two top panes are at a fraction of fluid flowing into the branch of 0.2, while the two bottom panes are at 0.05. Left: Particle *x* velocity versus *y* coordinate location. Right: Particle *y* velocity versus *y* coordinate location.

Analysis of only approximately 0.1s of the available data was necessary in each case to determine the position and velocity of 200 particles and the results are presented in Figure 6.7. As each simulation produced approximately 0.5s of data, 0.1s of data represents a sub-set of that available. Particle tracking showed that 41 and 14 particles were transported into the branch for β equal to 0.2 and 0.05 respectively. A calculation of *PTC* based on this sub-set of the simulation data results in values of 1.0 and 1.4, which are similar results to 1.0 and 1.3 as determined from analysis of the complete data set.

This indicates that the analysis of 200 particles is adequately representative of the complete simulation.

Examining the two left panes of Figure 6.7 illustrates that, with one exception, only particles transported next to the main slot wall on the same side as the branch are transported into the branch. For the case with β equal to 0.2, only one particle out of 41 transported into the branch is observed at a lateral position on the opposite side of the main slot on entering the intersection. With particles transported into the branch primarily drawn from lateral positions closest to the branch side of the main slot, *PTC* can be viewed as a direct function of the limit of lateral position in the main slot for which particles are transported into the branch.

Considering the case with β equal to 0.05, the particles transported into the branch are, on average, moving with lower velocity in the x coordinate direction on entering the intersection than those in the case with β equal to 0.2, as a result of the particle velocity distribution across the main slot. However, in the case with β equal to 0.2, the lateral forces applied to the particles are expected to be greater. Competition between these factors ultimately determines the limit of lateral position particles can be drawn from and consequently the resulting value of *PTC*.

The results shown in the right panes of Figure 6.7 demonstrates that for the case with β equal to 0.2, particles are travelling at larger average velocity in the y coordinate direction than the case with β equal to 0.05. This is a consequence of the larger lateral forces expected from the fluid acting on the particles in this case.

6.3.4 Effect of Branch Orientation

The second study of the effect of domain geometry is an examination of *PTC* with different orientation of the branch, θ. The values of the other parameters are identical to

those included in Table 6.1. The simulation data has been processed and the results are presented in Figure 6.8.

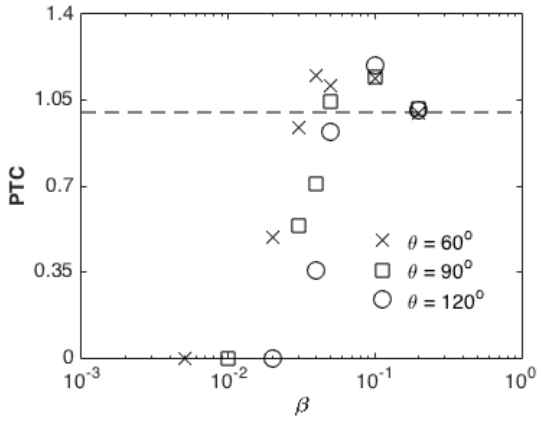

Figure 6.8. Particle transport coefficient versus the fraction of fluid flowing into the branch for branch orientation equal to 60, 90 and 120°.

The results shown in Figure 6.8 demonstrate that for β in the range 0.2 to 0.05, there is little difference in the value of *PTC* as a function of θ. However, for β equal to 0.04 and smaller, *PTC* is reduced for cases with larger θ. The value of β for which *PTC* is zero is larger for larger θ. Defining an effective branch width along the main slot as the distance between the branch walls in the x coordinate direction, this quantity takes the same value for θ equal to 60 and 120°. As a result, reduced *PTC* for θ equal to 120° compared to 60° must be attributed to reduced lateral forces arising from the fluid flow in the intersection. For θ equal to 90°, there is a smaller effective branch width along the main slot and different fluid flow in the intersection, which together result in the observed smaller *PTC* compared to θ equal to 60°. For three cases, θ and β equal to 60° and 0.01, 90° and 0.02, 120° and 0.03, there was at most 7 particles counted by *counter 3*. These have not been reported in Figure 6.7 due to the uncertainty associated with taking

averages over such small numbers of particles. For all simulations shown in Figure 6.8 with *PTC* reported as zero, at most one particle was recorded at *counter 3*.

The value of β_0 has been plotted versus θ and is shown in Figure 6.9.

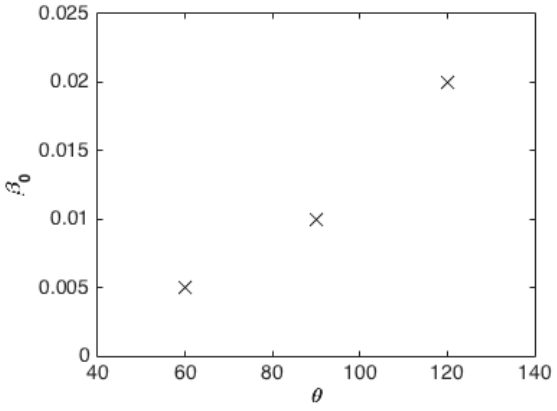

Figure 6.9. Proportion of fluid flowing into the branch at zero particle transport coefficient versus branch orientation.

The results shown in Figure 6.9 demonstrate that β_0 is larger for larger θ.

6.3.5 Effect of Reynolds Number

The effect of Re_s upon *PTC* has been examined through the analysis of four sets of simulation runs. The value of Re_s used for each set was 1000, 2000, 4000 and 8000. The values of the other parameters are identical to those presented in Table 6.1 and the results are presented in Figure 6.10.

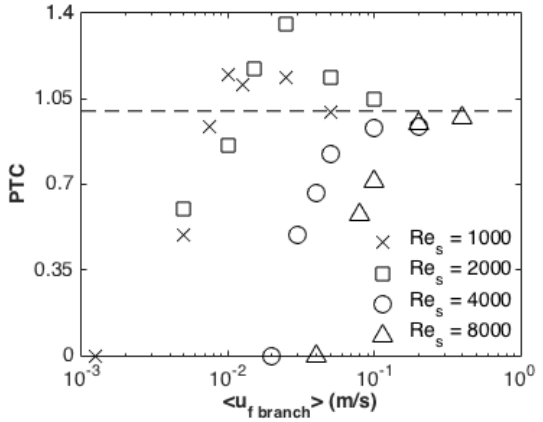

Figure 6.10. Particle transport coefficient versus average fluid velocity in the branch for Reynolds numbers of 1000, 2000, 4000 and 8000.

The simulation results presented in Figure 6.10 shows *PTC* versus the average fluid velocity in the direction of flow along the branch (m/s), $<u_{f\,branch}>$, in the absence of particles in the branch. This average has components in both the x and y coordinate directions due to the orientation of the branch. While the four sets of simulations have each been run with the same range of values of β, the results are presented in this manner to be able to compare *PTC* to the absolute quantity of fluid flowing into the branch.

The sets of results at Re_s of 1000 and 2000 demonstrate similar *PTC*, considering the range expected as a result of seeding (indicated by the results presented in the error bar plot of Figure 6.3). There is a similar characteristic peak in *PTC* as discussed in detail above. There is a reduction in *PTC* observed with increasing Re_s, evident through comparison of the results in the laminar flow regime (as noted above, at Re_s equal to 1000 and 2000 these are similar) to those in the turbulent flow regime at Re_s equal to 4000 and 8000. This is the result of larger particle translation velocities in the main slot, where similar lateral forces arising from fluid flow into the branch have less time to act on each particle. The results for the turbulent flow cases show that *PTC* decreases monotonically

with decreasing $<u_{f\,branch}>$, in contrast to the characteristic peak observed for cases in the laminar flow regime. The time-average fluid velocity profile across the main slot for the turbulent flow cases is much 'flatter' than that for laminar flow. While the time-average velocity profile for turbulent slot flow is Reynolds number dependent, in the range of Re_s of 4000 to 8000, the maximum fluid velocity is approximately 1.2 times the average fluid velocity. For comparison, this multiple is 3/2 for laminar flow. The difference in the fluid velocity profile results in a smaller distribution of particle translation velocities, producing the observed difference in the trend of *PTC*. Finally, it is observed that the value of $<u_{f\,branch}>$ at which *PTC* is zero is considerably larger for larger Re_s.

With the branch representing a dilated natural fracture and assuming no propagation, that is, the natural fracture does not become larger in areal extent, the fluid volume entering the natural fracture from the hydraulic fracture is equal to that lost to the reservoir rock and storage. Storage is volume change in the width distribution across the natural fracture. Change in width is related to change in fluid pressure, which typically occurs gradually during a hydraulic fracture treatment. As a result, storage can be reasonably neglected for this discussion, allowing the fluid volume lost to the reservoir rock to be equated to that entering the natural fracture. The fluid lost to an unconventional reservoir rock is very small due to its low permeability. It follows that in many cases it will be smaller than the value of $<u_{f\,branch}>$ at which *PTC* is zero, which means zero particles will be transported into the natural fracture.

For two cases, Re_s and β equal to 1000 and 0.01, and 2000 and 0.005, at most 7 particles were observed at *counter 3*. Results from these cases have not been reported in Figure 6.10 due to the uncertainty associated with taking averages over such small numbers of particles. For the simulation case at Re_s equal to 1000 shown in Figure 6.10, with *PTC* reported as zero, one particle was recorded at *counter 3*. With Re_s equal to 4000

and 8000, the results reported as zero shown in Figure 6.9 correspond to no more than 5 particles recorded at *counter 3*. While cases with a similar number of particles observed at *counter 3* for simulations at lower Reynolds number are not reported, in this case the total number of particles simulated is larger, approximately 1500 and 2000, compared to approximately 1000 for Re_s equal to 1000. This, in turn, corresponds to a smaller *PTC* of less than 0.2 and has been reported as zero.

The value of $\langle u_{f\ branch} \rangle$ at which *PTC* equals zero, $\langle u_{f\ branch} \rangle_0$, has been plotted versus Re_s and is shown in Figure 6.11.

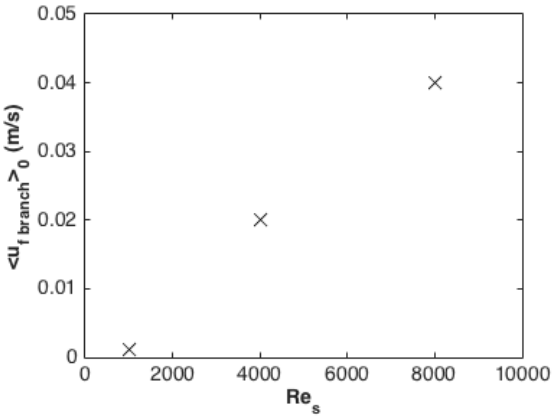

Figure 6.11. Average fluid velocity in the branch at zero particle transport coefficient versus slot flow Reynolds number.

The results shown in Figure 6.11 demonstrate that $\langle u_{f\ branch} \rangle_0$ is larger for larger Re_s.

6.3.6 Effect of Fluid Rheology

The particle transport coefficient calculated from simulation data with a Newtonian fluid viscosity (Pa-s), μ, of 0.001 and 0.0005Pa-s and Re_s of 1000 and 2000 is presented in Figure 6.12. The values of the other parameters are identical to those

presented in Table 6.1, though fewer lower viscosity simulation cases across the range of β were conducted.

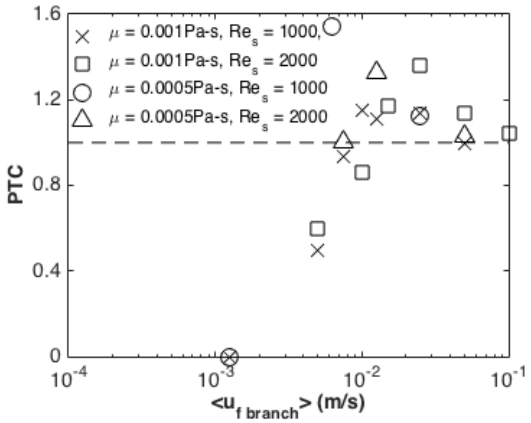

Figure 6.12. Particle transport coefficient versus average fluid velocity in the branch for different Newtonian fluid viscosity and Reynolds number.

Figure 6.12 shows the results of four sets of simulations, the first with μ equal to 0.001Pa-s and Re_s equal to 1000, the second with μ equal to 0.001Pa-s and Re_s equal to 2000, the third with μ equal to 0.0005Pa-s and Re_s equal to 1000 and finally the fourth with μ equal to 0.0005Pa-s and Re_s equal to 2000. There is very little difference observed in *PTC* between these four sets, put in the context of the uncertainty due to seeding as shown in Figure 6.3. The characteristic peak in *PTC* discussed in detail above is observed.

For the cases with μ equal to 0.001Pa-s and Re_s equal to 1000 and 2000, the results reported are discussed in relation to the presentation in Figure 6.10, above. For two cases with μ equal to 0.0005Pa-s, Re_s equal to 1000 and 2000 and β equal to 0.03 and 0.01 respectively, at most 4 particles were observed at *counter 3*. These results have not been reported in Figure 6.12 due to the uncertainty associated with taking averages over such small numbers of particles. For the simulation case with μ equal to 0.0005Pa-s, Re_s

equal to 1000 and β equal to 0.03, *PTC* was reported as zero with one particle was recorded at *counter 3*.

The effect of a shear-thinning power-law fluid upon *PTC* was examined with simulation cases run with η_c and *n* equal to 0.1Pa-s and 0.2, respectively. The results are shown in Figure 6.13.

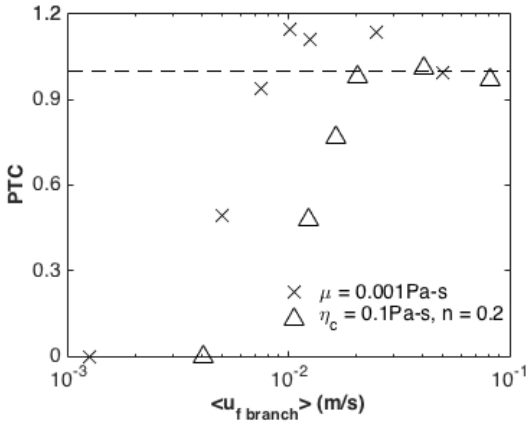

Figure 6.13. Particle transport coefficient versus average fluid velocity in the branch for a Newtonian and a shear-thinning power-law fluid.

There are two observations to be made regarding the results presented in Figure 6.13. The first is that *PTC* is smaller for the shear-thinning power-law fluid compared to the Newtonian fluid. Note that while Re_s is the same for the two sets of cases, the average fluid velocity for the shear-thinning power-law fluid is approximately 0.204m/s while it is 0.125m/s for the Newtonian fluid cases. However, to allow an appropriate comparison to be made, *PTC* is presented versus $<u_{f\ branch}>$ rather than β. Nonetheless, the smaller values of *PTC* reported cannot be attributed to the average fluid velocity since *PTC* for a Newtonian fluid at Re_s equal to 2000 (presented in Figure 6.12) are similar to those at 1000. The Newtonian fluid cases at Re_s of 2000 have an average fluid velocity is 0.25m/s,

similar to that for the shear-thinning power law fluid cases at Re_s of 1000. The lower values of *PTC* observed appear to be due to fluid rheology alone.

The second observation to be made is that results for the shear-thinning power-law cases demonstrate that *PTC* decreases monotonically with decreasing $<u_{f\ branch}>$. The characteristic peak for Newtonian fluid cases in the laminar flow regime is not evident for a shear-thinning power-law fluid. In fact, the trend is similar to those for a Newtonian fluid in the turbulent flow regime. The fluid velocity profile across the slot for a shear-thinning power-law fluid is 'flatter' compared to that for a Newtonian fluid. The maximum fluid velocity is approximately 1.2 times the average fluid velocity for n equal to 0.2, compared to that for a Newtonian fluid where it is 3/2. While the time-average fluid velocity profile for a Newtonian fluid in turbulent flow is different to that of a shear-thinning power-law fluid in laminar flow, they are both much 'flatter' than a Newtonian fluid in the laminar flow regime. In this context, the similarity in the trend of *PTC* versus $<u_{f\ branch}>$ for a shear-thinning power-law fluid in laminar flow and that for a Newtonian fluid in turbulent flow appears to be due to the assumed similar distribution of particle translation velocities.

For the cases with μ equal to 0.001Pa-s and Re_s equal to 1000, the results reported are discussed in relation to the presentation in Figure 6.12, above. For the shear-thinning power-law fluid cases, at β equal to 0.02, there are only 7 particles recorded at *counter 3* and as such this result has not been reported.

6.3.7 Effect of Particle Concentration, Size and Density

Several sets of simulations with different volumetric concentration, particle size and density have been analyzed with the results presented in Figure 6.14, Figure 6.15 and

Figure 6.16. In each case other parameters are identical to those listed in Table 6.1, except β, which was extended to 0.0025 for the 5% concentration cases.

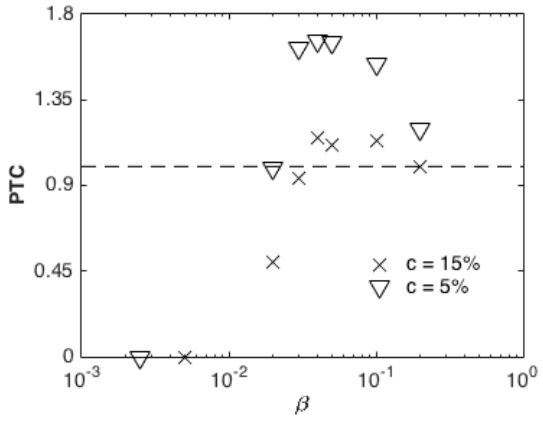

Figure 6.14. Particle transport coefficient versus the fraction of fluid flowing into the branch for concentration equal to 5 and 15% by volume.

The results in Figure 6.14 indicate that there is a dependency of *PTC* upon concentration. Increasing concentration decreases *PTC*. For the 5% concentration cases, a β of 0.005 and 0.01 resulted in 3 and 6 particle counts at *counter 3*, respectively. These results were not reported. The case with β of 0.0025 resulted in one particle at *counter 3* and has been reported as *PTC* equal to zero. The value of β for which *PTC* is zero is smaller for the 5% concentration cases compared to the 15% concentration cases.

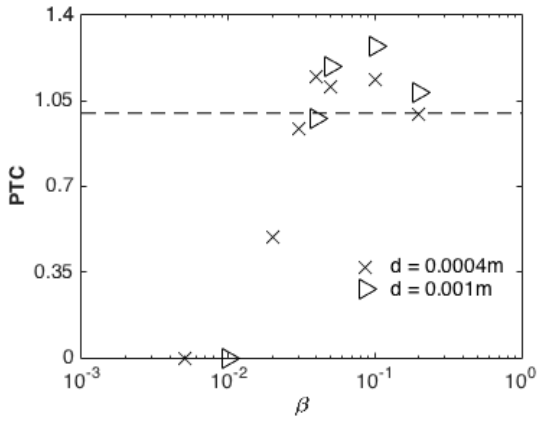

Figure 6.15. Particle transport coefficient versus the fraction of fluid flowing into the branch for particle diameter equal to 0.0004 and 0.001m.

Most of the results at larger particle diameter, d, shown in Figure 6.15 demonstrate similar values of *PTC* as those at smaller particle diameter. However, the value of β for which *PTC* is zero is larger for the larger particles. Note that the value of Re_s is the same, 1000, for both of these sets of simulations with d equal to 0.0004 and 0.001m. The larger particle diameter and larger domain used for comparison, combined with the same fluid viscosity, necessitate a smaller average fluid velocity for the same Re_s. Nonetheless, the product of the average fluid velocity and slot width are the same between the simulations at d equal to 0.0004 and 0.001m. A β equal to 0.02 and 0.03 resulted in 2 and 5 particle counts at *counter 3*, respectively, for the 0.001m diameter cases. These results were not reported. The case with β of 0.01 resulted in one particle at *counter 3* and has been reported as *PTC* equal to zero. The value of β for which *PTC* is zero is larger for the 0.001m diameter cases compared to the 0.0004m diameter cases.

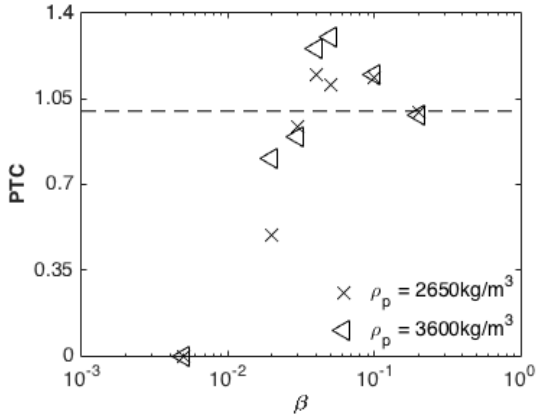

Figure 6.16. Particle transport coefficient versus the fraction of fluid flowing into the branch for particle density equal to 2650 and 3600kg/m^3.

Examining Figure 6.16, there is very little difference observed in *PTC* between the two sets of simulations with a particle density of 2650 and 3600kg/m^3, put in the context of the variability due to seeding as shown in Figure 6.3. For β equal to 0.01, the 3600kg/m^3 density particle case recorded 2 particle counts at *counter 3* and the result was not reported. For β equal to 0.005, the 3600kg/m^3 density particle case recorded one particle count at *counter 3* and *PTC* equal to zero was reported.

6.4 CONCLUSIONS

A rigorous numerical simulation approach for particle motion as a result of fluid flow, resolved CFD-DEM, has been validated for several applications including one very similar to that examined in this research. The approach has been applied to the transport of solid particles with fluid flow in a branched slot. A 'particle transport coefficient', *PTC*, has been defined by the proportion of particles transported into the branch at steady state, normalized by the proportion of fluid flowing into the branch. Cases of small branch width and large fluid proportion flowing into the branch have been shown to result in the formation of a stable particle bridge preventing subsequent particle transport

into the branch. This results in *PTC* being effectively zero. For the cases in which particle jamming was not evident, smaller branch aperture and larger angle of orientation between the main slot and branch generally result in smaller transport coefficient. There is also a reduction in *PTC* with larger Reynolds number at the inlet in most cases. There are two characteristic trends of *PTC* versus proportion of fluid flowing into the branch. A monotonic reduction in *PTC* with decreasing proportion of fluid flowing into the branch is the result of a 'flatter' fluid velocity profile across the main slot, whether due to turbulent flow of a Newtonian fluid or shear-thinning power-law fluid rheology in laminar flow. The other trend observed is characterized by a peak in *PTC*, at particular proportion of fluid, which is apparent for a Newtonian fluid in laminar flow. The fluid velocity profile in this case includes a larger difference between the maximum and average fluid velocity. Smaller particle size and concentration each result in a larger transport coefficient. Newtonian fluid viscosity and particle density do not affect *PTC* over the range of each examined.

Chapter 7: Width of Dilated Natural Fractures

The width of a dilated natural fracture has been determined, assuming linear elastic rock behavior and constant fluid pressure, via the implementation of a three-dimensional displacement discontinuity solution. Several cases of complex fracture geometry are examined, as is the effect of the in-situ stress state and fluid pressure.

7.1 INTRODUCTION

There are several methods available for determining the reservoir rock deformation that results from a hydraulic fracturing process. Confining the discussion to the solid mechanics problem, the media is typically assumed to be homogeneous, isotropic and linear elastic. Adopting this assumption, there are analytical solutions available for cases of particular geometry, such as the solution provided by Sneddon and Elliot (1946) for an infinitely long fracture subject to a prescribed distribution of internal fluid pressure. The functional dependence of fracture width upon constant net pressure, fracture height and elastic moduli derived by Sneddon and Elliot (1946) was used by Nordgren (1972) in the development of what became known as the 'Perkins, Kern and Nordgren' or 'PKN' fracture model. Since this model is based on the analytical solution for an infinitely long fracture, it is most accurate for fracture geometry where the length is much longer than the (constant) height.

If the geometry of the fracture deviates significantly from the assumptions used to develop a particular analytical solution, it cannot be expected to be accurate. In these cases a numerical solution is typically used. The fracture width distribution across a planar fracture of arbitrary geometry is available from Kossecka (1971), in the form of a boundary integral equation. Solution of this equation by a finite element approach was

used by Gu (1987) to construct a fracture model. This approach allows for the width distribution of a fracture of any length and variable height to be accurately determined, overcoming the restrictions of the 'PKN' and other models based on analytical solutions for a particular geometry.

Simultaneous propagation of multiple hydraulic fractures alters the surrounding stress field in a non-uniform manner. As a result, mixed mode fracture propagation may occur and produce non-planar fracture growth. In addition to this behavior, reservoir rocks deviate from the simplifying assumption of homogeneous, isotropic and linear elastic behavior due to the presence of discontinuities, including natural (pre-existing) fractures. The interaction between a propagating hydraulic fracture and natural fractures may result in non-planar fracture growth. Laboratory experiments by Lamont and Jessen (1963), Daneshy (1974) and Blanton (1986) examined the conditions under which diversion of a hydraulic fracture along a natural fracture plane produced non-planar growth. In the case of a hydraulic fracture bypassing a natural fracture, subsequent dilation may occur if the fluid pressure is sufficient.

There are several numerical methods suitable for determining the width distribution of non-planar fractures. Each of these can be divided into one of two broad classes, domain methods and boundary methods. The finite volume method is an example of the former, while the displacement discontinuity method is an example of the latter. A key advantage of using the displacement discontinuity method over the finite volume method is that it reduces the system of equations required and hence reduces the time taken to complete the calculation.

All displacement discontinuity methods utilize analytical solutions of the stresses induced by a displacement discontinuity over a finite line or area, for a solution in two or three dimensions respectively. Discretizing the boundary of a domain with a sufficient

number of elements allows the width distribution of a hydraulic fracture (planar or non-planar) to be determined. The two-dimensional solution provided by Crouch (1976) can be used to calculate the width distribution of very large height fractures. However, without modification it is not suitable for fractures of limited height. Olson (2004) proposed an empirical correction factor to enable the two-dimensional solution to be used to model hydraulic fractures with finite height. There are several three-dimensional solutions available, each applicable to a displacement discontinuity element of a particular shape. Rongved (1957) and Salamon (1964) provided the solution for a rectangular area, which was extended by Shou (1993). A simplification of this solution was proposed by Wu and Olson (2014), to enable faster computation of hydraulic fracture geometry. A three dimensional solution for triangular displacement discontinuity elements is available in Kuriyama and Mizuta (1993).

This research uses the complete set of equations for a three-dimensional formulation of rectangular displacement discontinuity elements to determine the width distribution of a hydraulic fracture and dilated natural fracture. The widths have been determined for several combinations of stress anisotropy, net pressure, hydraulic fracture height and length. The effect of the length, height and orientation of the natural fracture and the elastic moduli of the rock have also been examined. With a solution for the natural fracture width, its impact upon proppant transport is discussed.

7.2 Displacement Discontinuity Simulation

7.2.1 Formulation

A single rectangular displacement discontinuity element is shown in Figure 7.1.

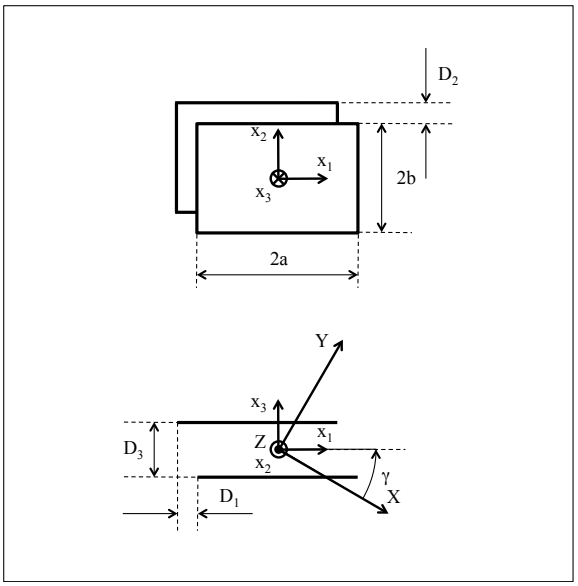

Figure 7.1. Rectangular displacement discontinuity element.

Figure 7.1 shows the three displacement discontinuity components, $D_i = (D_1, D_2, D_3)$, for a rectangular element of length $2a$ and height $2b$. The global coordinate system has Cartesian coordinate directions in X, Y and Z, while each element has a local Cartesian coordinate directions x_1, x_2 and x_3. Each displacement discontinuity component is the difference between the displacement of the negative and positive sides of the element, as follows:

$$D_i = u_i\left(x_1, x_2, 0^-\right) - u_i\left(x_1, x_2, 0^+\right) \quad (7.1)$$

For a homogeneous, isotropic, linear elastic media infinite in extent, the analytical solution for each component of the stress tensor induced by the displacement discontinuity of a particular element, in the local coordinate system, is available in Rongved (1957) and is as follows:

$$\sigma_{11} = \frac{G}{4\pi(1-\nu)}\left\{\left[2I_{13} - x_3 I_{111}\right]D_1 + \left[2\nu I_{23} - x_3 I_{211}\right]D_2 + \left[I_{33} + (1-2\nu)I_{22} - x_3 I_{311}\right]D_3\right\}$$

$$\sigma_{22} = \frac{G}{4\pi(1-\nu)}\left\{\left[2\nu I_{13} - x_3 I_{122}\right]D_1 + \left[2I_{23} - x_3 I_{222}\right]D_2 + \left[I_{33} + (1-2\nu)I_{11} - x_3 I_{322}\right]D_3\right\}$$

$$\sigma_{33} = \frac{G}{4\pi(1-\nu)}\left\{\left[-x_3 I_{133}\right]D_1 + \left[-x_3 I_{233}\right]D_2 + \left[I_{33} - x_3 I_{333}\right]D_3\right\}$$

$$\sigma_{12} = \frac{G}{4\pi(1-\nu)}\left\{\left[(1-\nu)I_{23} - x_3 I_{112}\right]D_1 + \left[(1-\nu)I_{13} - x_3 I_{212}\right]D_2 + \left[-(1-2\nu)I_{12} - x_3 I_{312}\right]D_3\right\}$$

$$\sigma_{13} = \frac{G}{4\pi(1-\nu)}\left\{\left[I_{33} + \nu I_{22} - x_3 I_{113}\right]D_1 + \left[-\nu I_{12} - x_3 I_{213}\right]D_2 + \left[-x_3 I_{313}\right]D_3\right\}$$

$$\sigma_{23} = \frac{G}{4\pi(1-\nu)}\left\{\left[-\nu I_{21} - x_3 I_{123}\right]D_1 + \left[I_{33} + \nu I_{11} - x_3 I_{223}\right]D_2 + \left[-x_3 I_{323}\right]D_3\right\} \quad (7.2)$$

where G is the shear modulus (Pa) and ν is Poisson's ratio. I_{ij} and I_{ijk} are the second and third partial derivatives (i = 1, 2 or 3 denotes the partial derivative with respect to x_1, x_2 and x_3 respectively) of the following function:

$$I(x_1, x_2, x_3) = \int_{-b}^{b}\int_{-a}^{a} \frac{1}{\sqrt{(x_1-\xi_1)^2 + (x_2-\xi_2)^2 + x_3^2}} d\xi_1 \xi_2 \quad (7.3)$$

which after integrating twice yields:

$$I(x_1, x_2, x_3) = \left[\overline{x_1}\ln\left(r + \overline{x_2}\right) + \overline{x_2}\ln\left(r + \overline{x_1}\right) - x_3 \tan^{-1}\left(\frac{\overline{x_1}\,\overline{x_2}}{r x_3}\right)\right]\Bigg|_{\xi_1=-a}^{\xi_1=a}\Bigg|_{\xi_2=-b}^{\xi_2=b} \quad (7.4)$$

where

$$r = \sqrt{\overline{x_1}^2 + \overline{x_2}^2 + x_3^2}\,, \quad \overline{x_1} = x_1 - \xi_1 \text{ and } \overline{x_2} = x_2 - \xi_2 \quad (7.5)$$

Practical engineering problems require the solution of more than one element. Solving many elements simultaneously requires determining the influence each element in the system has on the normal and shear stresses of every element in the system. This is done through transformation of the contribution of each element to the stress tensor in the local coordinate system of that particular element. For a fluid filled fracture, the normal

stress on each element is equal the local fluid pressure, p, minus the far field stress normal to the plane of the element, the two shear stresses are each equal to zero. These boundary conditions are as follows:

$$\sigma_{33} = p - \sigma_{33\ remote}$$

$$\sigma_{13} = 0$$

$$\sigma_{23} = 0 \qquad (7.6)$$

Through coordinate transformation of the analytical solution for the contribution each displacement discontinuity makes to the stress tensor, a matrix of influence coefficients, A, is determined for particular system geometry. The matrix A relates the stress boundary conditions, $\sigma_{boundary}$, to the displacement discontinuities, D. With the number of elements N, the influence coefficient matrix contains $9N^2$ entries, while the column vector of stresses at the boundary contains $3N$ entries. The matrix A is inverted for a solution of D due to $\sigma_{boundary}$. This system can be written as:

$$AD = \sigma_{boundary} \qquad (7.7)$$

7.2.2 Verification

To examine the accuracy of the formulation, comparisons were made to the analytical solution for an infinitely long fracture at constant pressure available in Sneddon and Elliot (1946). This solution can be expressed as follows:

$$W(Z) = \frac{(1-\nu)}{G}\left(H^2 - 4Z^2\right)^{1/2} p_{net} \qquad (7.8)$$

where W is the width of a fracture of height H with the origin of the coordinate system at the center of the fracture in terms of height. The fluid pressure minus the stress normal to the fracture is p_{net}. The maximum width, W_{max}, occurs at the origin and hence:

$$W_{max} = \frac{(1-\nu)}{G} H p_{net} \qquad (7.9)$$

The displacement discontinuity method has been applied to a planar fracture of H equal to 10m and length L equal to 100m. The ratio of L/H is 10, which approximates an infinitely long fracture and enables comparison to the analytical solution of Sneddon and Elliot (1946). Results for G equal to 1.06×10^{10}Pa, ν equal to 0.3 and p_{net} equal to 3.447×10^{6}Pa are shown in Figure 7.2.

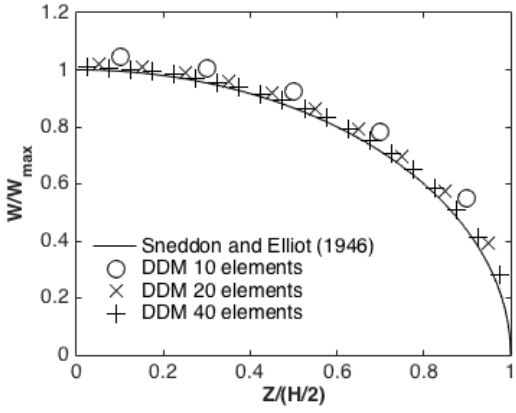

Figure 7.2. Analytical and displacement discontinuity solutions to the width of a constant pressure fracture.

Several different numbers of elements have been used for discretization in the vertical direction using the displacement discontinuity method, 10, 20 and 40. The analytical solution W and D_3 at the center of the fracture along its length were normalized by W_{max}. Due to symmetry, only half of the solution is required to make a comparison, with Z normalized by $H/2$. There is good agreement demonstrated between the numerical results and the analytical solution, with better agreement apparent when more elements are used and closest to the center of the fracture in terms of height.

7.2.3 Application to a Dilated Natural Fracture

The simplified geometry of a hydraulic fracture and dilated natural fracture is shown in Figure 7.3.

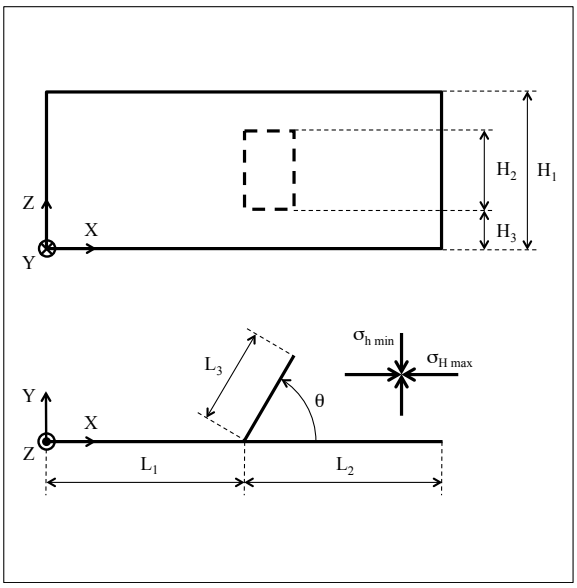

Figure 7.3. Geometry of a hydraulic fracture and dilated natural fracture.

For the application of interest in this research, determining the width distribution of a hydraulic and dilated natural fracture, a constant fluid pressure has been applied to each element used to create the simplified geometry shown above. Examining the results of the verification comparison, use of 20 elements in height provides sufficient accuracy without unnecessary computational expense.

7.3 RESULTS

7.3.1 Results Overview

The width distribution of a hydraulic and dilated natural fracture has been determined for several cases of stress anisotropy and pressure. These allow for the conditions under which natural fracture dilation occurs to be determined. The geometry of the fracture, both in terms of the height and length of each fracture, were each varied systematically and a calculation of the widths made. The effect of natural fracture orientation and location was also examined, as was the elastic moduli of the rock.

The width distribution of a hydraulic fracture with both L_1 and L_2 equal to 76.2m and a natural fracture with L_3 equal to 6.096m and oriented at 60° to the hydraulic fracture was calculated. Both H_1 and H_2 are equal to 60.96m. The elastic moduli G and ν were equal to 1.06×10^{10}Pa and 0.25 respectively, while σ_{hmin} was equal to 1.379×10^{7}Pa with zero stress anisotropy present ($\sigma_{Hmax} = \sigma_{hmin}$). The width variation with height for the hydraulic and natural fractures at the intersection is shown in Figure 7.4. The natural fracture widths are taken from the elements closest to the hydraulic fracture, while the hydraulic fracture widths are at X equal to L_1-a.

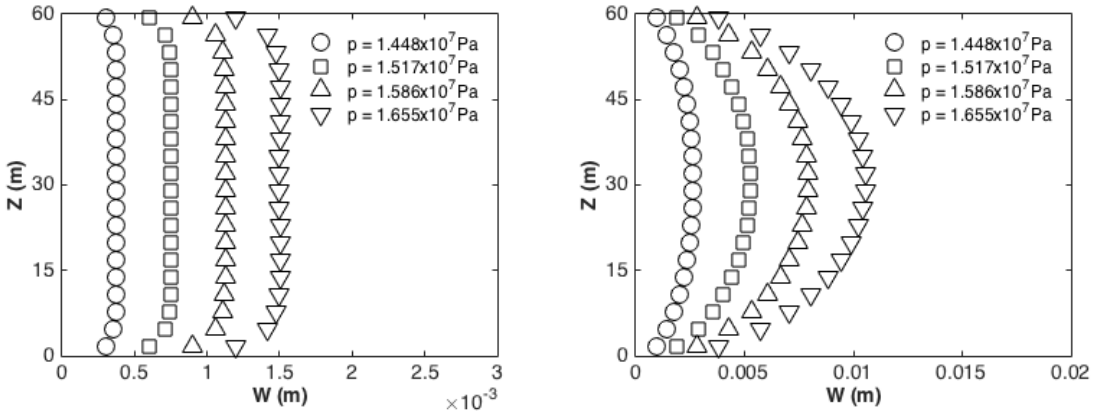

Figure 7.4. Left: Width variation with height for a natural fracture. Right: Width variation with height for a hydraulic fracture.

Examining Figure 7.4, variation in width with height is apparent for both the hydraulic and natural fracture. The width distribution for the hydraulic fracture more closely approximates the analytical solution of Sneddon and Elliot (1946), while there is less variation for the natural fracture, which has a much smaller length. While there is zero stress anisotropy applied, the width of the natural fracture is much smaller than that of the hydraulic fracture due to the fracture geometry. For practical reasons, the width at the center of each fracture in terms of height is shown in subsequent figures, W_{hyd} is the width of the hydraulic fracture and W_{nat} is the width of the natural fracture.

7.3.2 Effect of Stress Anisotropy and Net Pressure

The same fracture geometry examined in Figure 7.4 has been used with several values of p and σ_{Hmax}, with the simulation data presented in Figure 7.5.

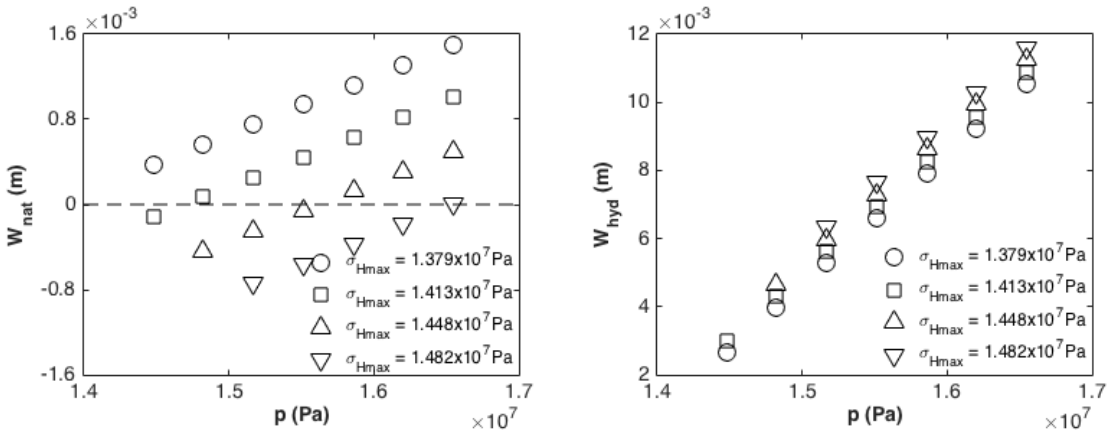

Figure 7.5. Left: Width versus fluid pressure for a natural fracture. Right: Width versus fluid pressure for a hydraulic fracture.

In all cases W_{nat} is much smaller than W_{hyd} and there is an increase in both with increasing p, as shown in Figure 7.5. For many cases of smaller p and larger σ_{Hmax}, W_{nat} is negative. A dashed line is shown at W_{nat} equal to zero in this figure to aid identification of these cases. While the displacement discontinuity method allows for this unphysical solution, the physical interpretation to be drawn is that the natural fracture would not dilate for the given combination of geometry, pressure and remote stress. It should be noted that in all these cases, p is larger than σ_{Hmax} and as a result it is entirely the influence of the hydraulic fracture on the surrounding stress field that produces this result. The entire displacement discontinuity solution is incorrect in cases where W_{nat} is negative, including the value of W_{hyd}. Another observation is that the largest σ_{Hmax} cases result in larger W_{hyd} for a given p as there is less mechanical influence from the smaller W_{nat}. Considering a hydraulic fracture with no natural fractures present, σ_{Hmax} has no

effect upon W_{hyd}. These results clearly illustrate two mechanisms by which there is interaction between natural and hydraulic fractures.

7.3.3 Effect of Fracture Height

For p equal to 1.379x10^{7}Pa and 1.413x10^{7}Pa, several values of fracture height ($H_1 = H_2$, $H_3 = 0$) were simulated with all other variables taking the same values as above. The results are presented in Figure 7.6.

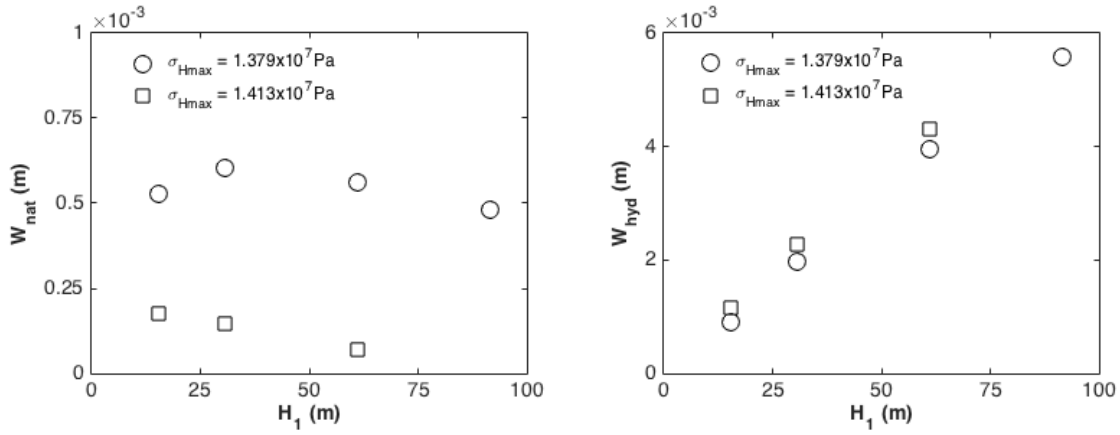

Figure 7.6. Left: Width versus fracture height for a natural fracture. Right: Width versus fracture height for a hydraulic fracture.

W_{nat} is smaller than W_{hyd} and relatively insensitive to fracture height. Larger σ_{Hmax} reduces W_{nat} but increases W_{hyd}. W_{hyd} is approximately linearly proportional to fracture height. The result of a case including a natural fracture of smaller height than the hydraulic fracture is presented in Figure 7.7.

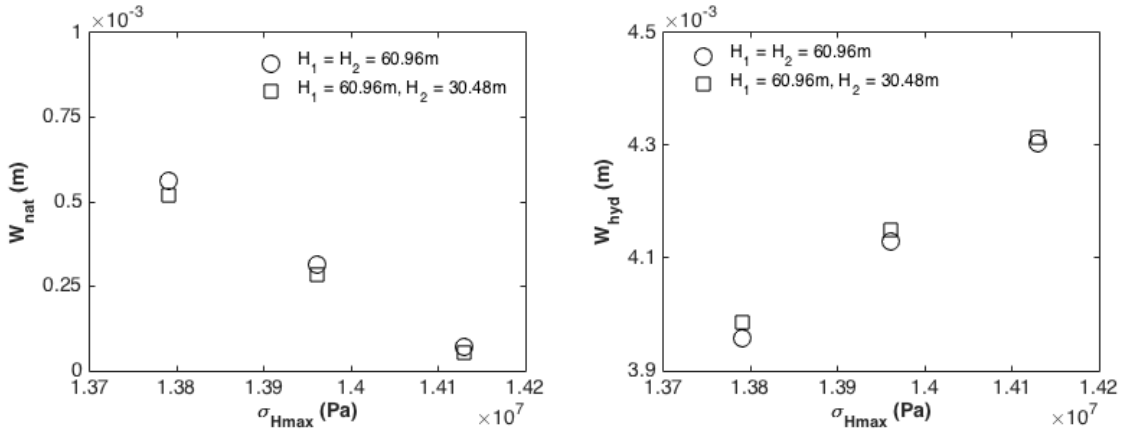

Figure 7.7. Left: Width versus maximum horizontal stress for full and partial height natural fractures. Right: Width versus maximum horizontal stress for a hydraulic fracture.

The results from a case with H_1 equal to 60.96m, H_2 equal to 30.48m and H_3 equal to 15.24m are shown in Figure 7.7. There is only a small difference apparent comparing the simulation results for the half height fracture to the full height fracture. For a single infinitely long fracture, the width is proportional to the height, as indicated by the solution of Sneddon and Elliot (1946). While this simulation is of a fully three dimensional multi planar fracture, the width of the natural fracture is controlled by the smaller of its two dimensions, length and height. In this case, since L_3 is smaller than H_2, W_{nat} is relatively insensitive to H_2.

7.3.4 Effect of Fracture Length

With all other variables taking the same values as above, simulations were run with L_1 equal to 38.1m and 152.4m. For all cases $L_1 = L_2$. The results are presented in Figure 7.8.

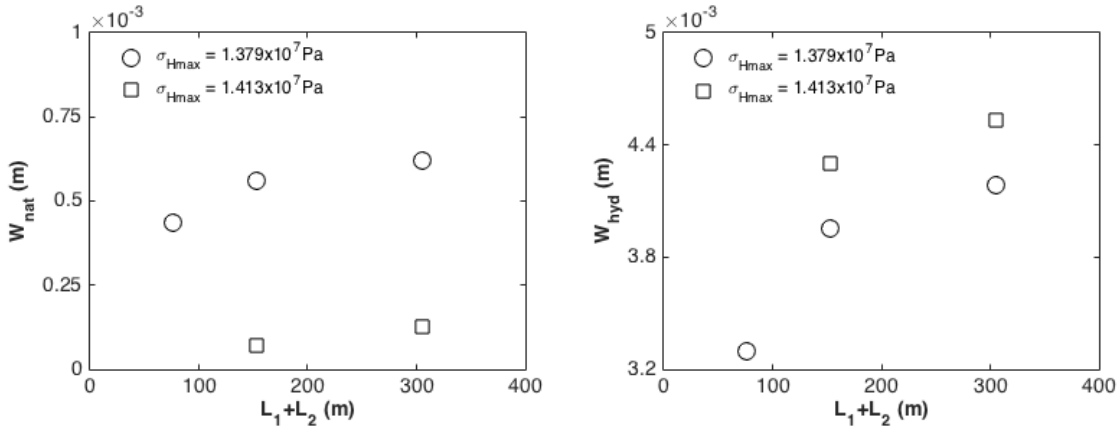

Figure 7.8. Left: Width versus total hydraulic fracture length for a natural fracture. Right: Width versus total hydraulic fracture length for a hydraulic fracture.

W_{nat} is relatively insensitive to the total hydraulic fracture length. Larger W_{nat} from smaller σ_{Hmax} results in smaller W_{hyd}. Cases with several natural fracture lengths have been simulated, with the results presented in Figure 7.9.

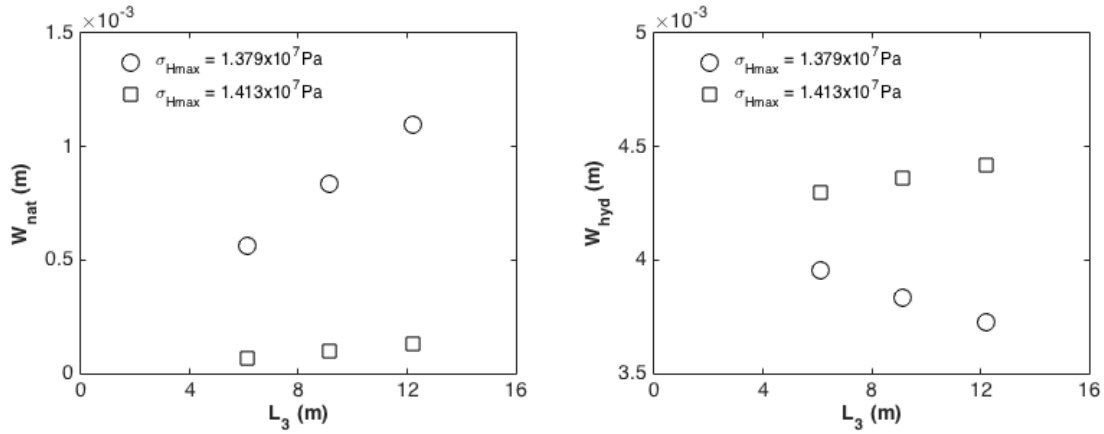

Figure 7.9. Left: Width versus natural fracture length for a natural fracture. Right: Width versus natural fracture length for a hydraulic fracture.

W_{nat} increases with larger L_3. L_3 is smaller than H_2 and thereby controls the fracture width. Again larger W_{nat} from smaller σ_{Hmax} results in smaller W_{hyd}.

7.3.5 Effect of Natural Fracture Location and Orientation

Several cases with different dimensionless natural fracture locations, $L_1/(L_1+L_2)$, have been simulated. The total hydraulic fracture length, L_1+L_2, is the same in all cases, as are the remaining variables. The simulation data is presented in Figure 7.10.

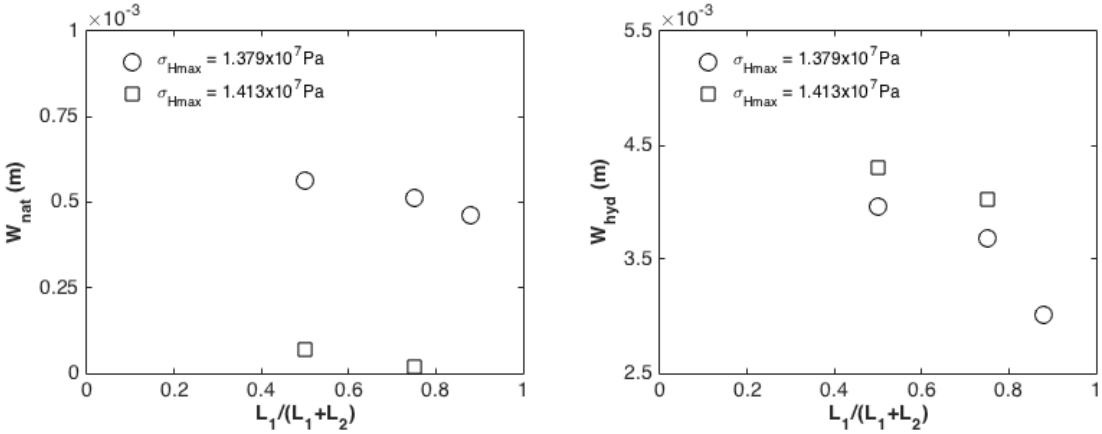

Figure 7.10. Left: Width versus position of the natural fracture for a natural fracture. Right: Width versus position of the natural fracture for a hydraulic fracture.

W_{nat} is relatively insensitive to the location of the natural fracture. There appears to be a significant difference in W_{hyd} with the position of the natural fracture, though this may be more simply attributed to the change in width with the position along the length of the hydraulic fracture. The familiar result of larger W_{nat} from smaller σ_{Hmax} resulting in smaller W_{hyd} is also apparent. The orientation of the natural fracture, θ, has been set to 75° and 90°, with all other variables held constant, to allow for comparison shown in Figure 7.11.

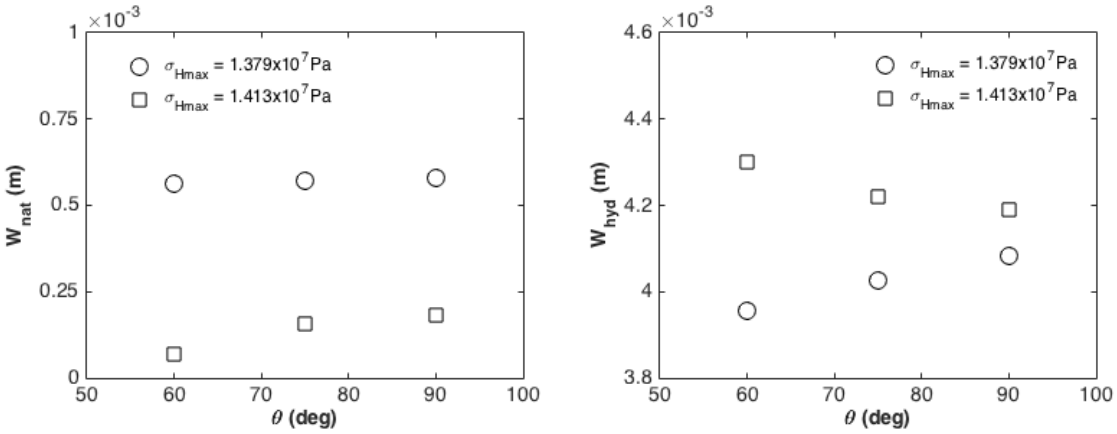

Figure 7.11. Left: Width versus natural fracture orientation for a natural fracture. Right: Width versus natural fracture orientation for a hydraulic fracture.

W_{nat} is relatively insensitive to θ. The trend with smaller σ_{Hmax} producing larger W_{nat}, which in turn results in smaller W_{hyd} is again apparent.

7.3.6 Effect of Elastic Moduli

Examining the analytical expressions for the stresses induced by the displacement discontinuity of a rectangular element, the stresses are linearly proportional to $G/(1-\nu)$. As a result the fracture width is linearly proportional to the inverse of this quantity.

7.4 Implications for Proppant Transport

Chapter 6 is a detailed particle-scale study of proppant transport in a branched slot. One conclusion determined from that study is that the width of the branch, W_2, affects the normalized proportion of proppant transported into the branch, *PTC*. Smaller W_2 results in smaller *PTC*. Many cases examined in this chapter produce a dilated natural fracture width of approximately 0.0005m. Commonly used proppant with diameter, d, of 0.00025m and 0.0004m, and a dilated natural fracture of such limited width results in a ratio d/W_{nat} of 0.5 and 0.8, respectively. The results shown in Figure 7.4 demonstrate that the *PTC* would be reduced by a factor larger than two for d/W_{nat} of 0.8 compared to 0.5,

for the proportion of fluid flowing into the branch, β, equal to 0.02. That is, a larger proportion of smaller proppant would be transported into a dilated natural fracture of the same width. It should be noted that there are many cases examined where the dilated natural fracture width is so small that common proppant sizes would be excluded simply based on size.

7.5 CONCLUSIONS

The three-dimensional displacement discontinuity method has been validated by comparison to the analytical solution for the width distribution of an infinitely long constant pressure fracture. With good agreement found, the method has been used to determine the width of a natural fracture dilated by a hydraulic fracture. In many cases of larger maximum horizontal stress, dilation does not occur. A reduction in width of the hydraulic fracture occurs as a result of natural fracture dilation.

The height of each fracture and the location and orientation of the natural fracture do not significantly effect the width of the natural fracture. The length of the natural fracture and the elastic moduli, $G/(1-\nu)$, do alter the width of the natural fracture significantly. Larger natural fracture length produces a wider fracture while larger elastic moduli reduces the width. Most cases examined in this study would result in the proppant transport efficiency into a dilated natural fracture being significantly less than one and in many cases zero due to size exclusion.

Chapter 8: Conclusions and Future Work

Through simulation, at both the particle scale and the fracture scale, aspects of proppant transport in simple and complex hydraulic fracture networks have been examined. At the small scale, the relative average velocity for proppant and fluid in a pressure driven flow, the settling velocity and the proportion of proppant transported into a branch have each been quantified. At the fracture scale, the proppant distribution in a single planar fracture has been determined using the relative proppant phase velocity determined at the small scale. The width of a dilated natural fracture has been determined, which is one significant factor controlling proppant entry.

8.1 Conclusions

The resolved CFD-DEM simulation approach (as detailed in Chapter 2) was used to determine the relative phase velocity of proppant and fluid in pressure driven slot flow. The results are presented in Chapter 3. To determine the suitability of the CFD-DEM approach to this application, verification was completed by means of comparison to the accepted solution for the translation velocity of a single particle in slot Poiseuille flow at low Reynolds number. Good agreement was found. Analysis of multiple-particle simulations demonstrated that the average particle velocity relative to the average fluid velocity was reduced with increased concentration. In addition, there was found to be a peak in the dimensionless average particle velocity at a particle diameter to slot width ratio of 0.8.

The average particle settling velocity in an open slot was quantified by the CFD-DEM approach and the results are presented in Chapter 4. The verification for this specific application was undertaken by comparison to the accepted solution for the

settling velocity of a single particle between two walls at low Reynolds number. The results of the comparison were favorable. In the absence of counter current fluid flow due to the boundary conditions imposed upon the simulation domain, the average particle settling velocity was demonstrated to increase with increasing concentration. The dependency upon particle size, density difference between the particles and the fluid and the viscosity each followed the qualitative trend predicted by Stokes' law.

The relative phase velocity of proppant and fluid in pressure driven slot flow (quantified in Chapter 3) was incorporated in UTEFRAC-3D via a correlation and presented in Chapter 5. Reduced proppant phase velocity with increased concentration leads to a reduction in propped fracture lengths. The reduction in length is greater for larger injection rates as transport by convection is a more significant transport mechanism than settling. This is one factor potentially responsible for the common discrepancy observed between propped fracture lengths predicted by simulation and those inferred from production history matching.

Chapter 6 presented results from a study of the normalized proportion of particles transported into a slot bifurcation using the CFD-DEM approach. It was demonstrated that below a critical rate of fluid flow into the branch, no particles enter the branch. It was also demonstrated that, for particular geometry, there is a critical rate above which particles form stable bridges and prevent subsequent particle transport into the branch. In between these limits, the fluid split normalized proportion of particles transported can be larger or smaller than one.

The three-dimensional displacement discontinuity method for rectangular elements has been employed to examine the width of a dilated natural fracture, with the results presented in Chapter 7. To confirm the accuracy of the approach, comparison to the analytical solution for the width distribution of an infinitely long constant pressure

fracture was made. Good agreement was found. In many cases of larger maximum horizontal stress, natural fracture dilation does not occur. Further, where dilation does occur, most cases examined in this study would result in the particle transport efficiency being significantly less than one and in many cases zero due to size exclusion.

8.2 Future Work

The resolved CFD-DEM implementation used in this work has several limitations. One such limitation is omission of the rotational component of particle velocity in the CFD representation of the system. That is, the calculation of the particle velocity given by (2.12) is simplified to (2.18) by neglecting the second term. Inclusion of this term would remove one simplification and may improve the accuracy of the results.

Another limitation, shared by all resolved CFD-DEM implementations, is the numerical expense of the method. Many simulation cases presented in this research, including all of the branched slot cases presented in Chapter 6, were run for 96 hours to produce sufficient data, see Appendix A for more detail. Several of these cases, in particular those with a small fraction of fluid flowing into the branch, would benefit from the production of more simulation data. More simulation data would reduce the range in the estimate of the particle transport coefficient (see Figure 6.3). While *Lonestar 4* was used for the computation of all cases presented in this research, *Lonestar 5* has since superseded it. Presumably this machine is faster, allowing for the production of more simulation data in the same amount of run time.

A further limitation is simulation stability, which by trial and error was found to depend upon more than the requirements of each separate simulation approach. These requirements are the Courant number for CFD and the Hertz and Raleigh times for DEM.

The number of processors used for processing the decomposed domain was limited to 12 or 24. Processors are available in multiples of 12 on *Lonestar 4*. Some cases would run successfully on 12 processors but fail on 24, while others would run on both. All cases tested failed to run successfully on 36 processors. Addressing the (as yet unknown) source of this issue would allow for much more efficient computation using a larger number of processors.

A second limitation related to stability is the number and concentration of particles than can be successfully simulated. By trial and error, a practical limit on concentration of ~0.25 was determined. The total number of particles was limited to approximately 150. The amount of simulation data produced for a given run time is dramatically reduced by larger numbers of particles. This, in turn, limits application of resolved CFD-DEM to small domains. Early in this research, the simultaneous simulation of particles settling while transported by pressure driven flow was attempted. The method was found to be unsuitable for this application as the small domains required particle re-circulation, which in turn caused a numerical artifact in the velocity of each particle as it moved from one boundary to the next. This artifact was found to be acceptable for determining the relative velocity of the proppant and fluid phases, as noted in Appendix B, but introduced unacceptable error for particle settling calculations. Unresolved CFD-DEM may provide a suitable method to apply to this problem as orders of magnitude more particles can be simulated.

Appendix A: Numerical Expense

The multiple-particle slot Poiseuille flow simulation cases presented in Chapter 3 were each run for sufficient time to produce 0.1s of simulation data. As noted in Chapter 2, a particle diameter of 0.0004m and a DEM time step of $3x10^{-8}$s have been used in the majority of simulations, including those for which the results are presented in Figure 3.11. For these simulations, a coupling interval of 20 has been used for all cases except those with *d*/*W* equal to 0.1, for which a coupling interval of 40 was used. The run time required for each of these cases is presented in Figure A1.

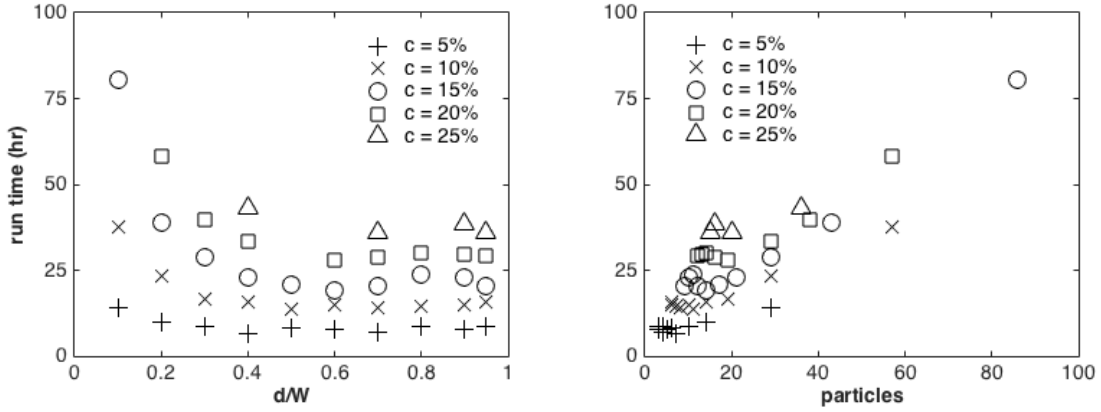

Figure A1. Left: Run time versus particle diameter to slot width ratio. Right: Run time versus number of particles.

The results shown in the left pane of Figure A1 demonstrate that smaller particle diameter to slot width ratio cases typically require larger run times. For a particular concentration, more particles are required for a case with small particle diameter to slot width ratio as the width and hence volume of the domain is larger. For a given domain size, larger concentration cases require larger run times. The right pane of Figure A1 shows that simulation cases with more particles require longer run times. For a particular number of particles, the run time required is larger for larger concentration.

The branched slot particle transport simulation cases presented in Chapter 6 were all run for 96 hours. A particle diameter of 0.0004m and a DEM time step of $3x10^{-8}$s have been used for simulation cases with results presented in Figure 6.13. A coupling interval of 100 has been used. The quantity of simulation data produced during this run time varies between simulation cases, as shown in Figure A2.

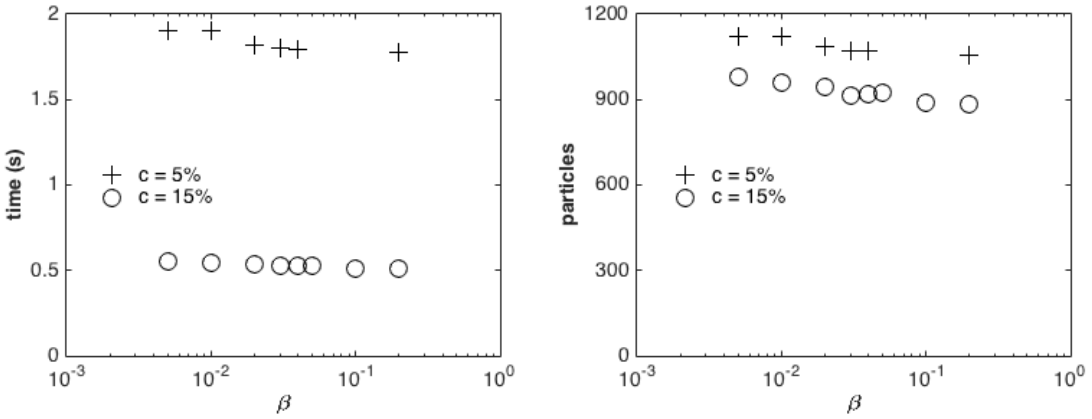

Figure A2. Left: Quantity of simulation data produced versus proportion of fluid flowing into the branch. Right: Number of particles counted by *counter 1* versus proportion of fluid flowing into the branch.

The left pane of Figure A2 demonstrates a slight dependency in quantity of simulation data produced upon proportion of fluid flowing into the branch, with more produced for smaller β. Of all independent variables examined, the most significant factor determining how much simulation data is produced is the concentration. The 5% concentration cases produced more than three times the simulation data of the 15% cases. However, examining the number of particles counted by *counter 1*, which is located prior to the intersection, the total counted during the simulation is similar between cases of different concentration.

Appendix B: Numerical Artifact

The particle translational velocity during several passes through the domain at the centerline is shown in Figure B1, for two cases, one with a particle diameter to slot width ratio of 0.1 and the other of 0.95.

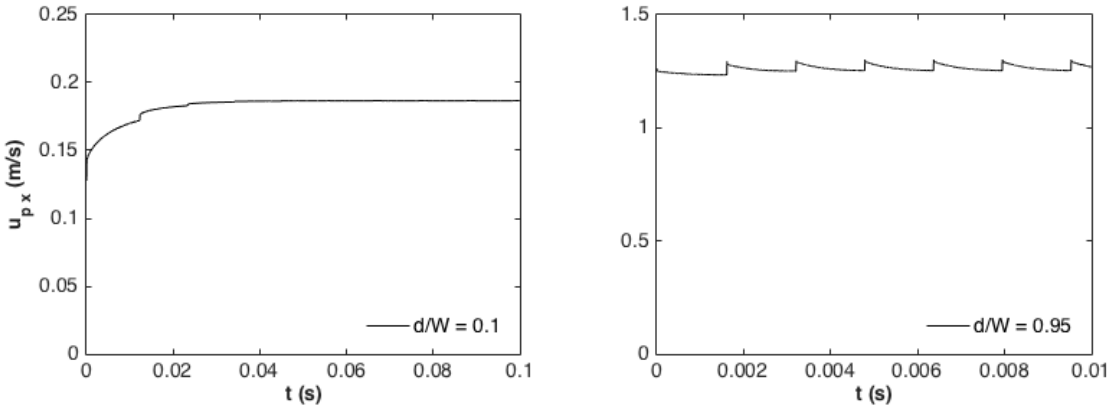

Figure B1. Left: Particle velocity transient for a particle to slot width ratio of 0.1. Right: Particle velocity transient for a particle to slot width ratio of 0.95.

There are two observations to be made. Firstly, there is a transient period as the particle accelerates from the average fluid velocity, the initial condition used. However, this is small for *d*/*W* equal to 0.1 and negligible for *d*/*W* equal to 0.95. Secondly, there is a small 'step' in the velocity as the particle passes from the *outlet* and returns at the *inlet* as a result of the boundary conditions applied. This is evident for *d*/*W* equal to 0.1 during the transient period but not during the steady state portion of the response. For *d*/*W* equal to 0.95 it is apparent during both periods and appears as a 'sawtooth' profile. Placing the DEM boundaries in the *x* coordinate direction two particle diameters inside the CFD boundaries reduced this numerical artifact when compared to using coincident boundaries. Imposition of the required CFD boundary conditions to achieve slot Poiseuille flow, combined with the particle representation in the CFD simulation produces this effect.

Simulations with a larger domain were conducted to understand the effect of this artifact upon the results. A DEM domain of 10 particle diameters in length, where a length of 5 particle diameters was used for all other simulations, was constructed. The velocity transient for a particle translating in the longer domain is shown in Figure B2.

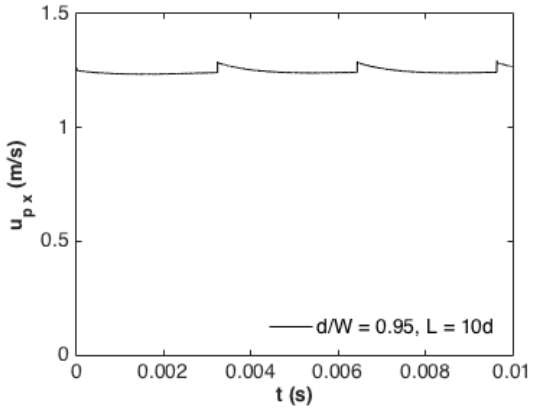

Figure B2. Particle velocity transient for a particle diameter to slot width ratio of 0.95.

Ten simulation cases were run across the range of *d*/*W*. The velocity transient for *d*/*W* equal to 0.95 is shown in Figure B2 to illustrate the case with the largest numerical artifact apparent. In the longer domain it is clear that particle does in fact reach a steady state for a significant portion of its translation through the slot. To enable reporting of translation velocity results without the numerical artifact, the average of the particle velocity was determined over the half of the domain furthest from the inlet, where the true steady state conditions are realized. These have been compared with simulation data from the smaller domain of 5*d* length. The comparison is presented in Figure B3.

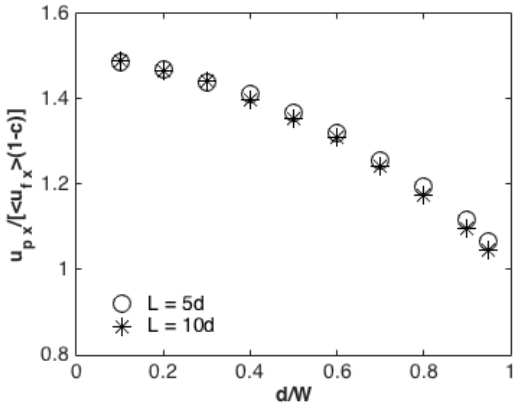

Figure B3. Particle velocity normalized by the modified average fluid velocity versus particle diameter to slot width ratio. Particle located at the center of the slot in both the small and large length domains.

Figure B3 shows that there is a small difference in the results from the two different domain sizes and different processing methods. The difference, although small, is largest for large *d*/*W*. For these cases, using a small domain and the mass counter processing method (which does not exclude the numerical artifact) results in a slightly larger particle velocity to be calculated, as would be expected from examination of the 'step' increase in velocity as the particle recirculates. Nonetheless, the effect is small and as a result the small domain and simplified data processing method has been applied in this research.

Nomenclature

A: influence coefficient matrix (Pa/m)

a: constant velocity (m/s)

B: slot half width (m)

B_1: constant

b: constant velocity (m/s)

C_L: Carter leak-off coefficient ($m/s^{0.5}$)

c: volumetric solids concentration

D: displacement discontinuity (m)

D_1: ride displacement discontinuity 1 (m)

D_2: ride displacement discontinuity 2 (m)

D_3: opening mode displacement discontinuity (m)

d: particle diameter (m)

Δd: fracture propagation (m)

E: Young's modulus (Pa)

$\boldsymbol{e}$: rate of strain tensor (1/s)

$\boldsymbol{F}_{Archimedes}$: difference between gravity and buoyancy forces (N)

$\boldsymbol{F}_{ij}$: inter-particle force between particles i and j in Lagrangian coordinate system (N)

$\boldsymbol{F}_{i\,total}$: total force acting on particle i (N)

F_t: dimensionless force coefficient

$\langle F_{t\,B} \rangle$: average dimensionless force coefficient based on Bird *et al*. (2007)

$\langle F_{t\,S} \rangle$: average dimensionless force coefficient based on Stokes' law

f: friction factor

G: shear modulus (Pa)

$\boldsymbol{g}$: acceleration due to gravity (m/s^2)

H: domain height (m)

H_1: hydraulic fracture height (m)

H_2: natural fracture height (m)

H_3: natural fracture vertical offset (m)

h: function 'h'

I_i: moment of inertia ($kg\text{-}m^2$)

K_I: Mode-I stress intensity factor ($Pa\text{-}m^{0.5}$)

K_{IC}: rock toughness ($Pa\text{-}m^{0.5}$)

k_n: normal spring coefficient (N/m)

k_t: tangential spring coefficient (N/m)

L: domain length (m)

L_1: partial length of hydraulic fracture (m)

L_2: partial length of hydraulic fracture (m)

L_3: length of natural fracture (m)

$\boldsymbol{M}_{i\ total}$: total moment acting on particle i (N-m)

m: unit conversion constant

$\dot{m}$: average particle mass rate in the x direction (kg/s)

$\dot{m}_1$: average particle mass rate at *counter 1* (kg/s)

$\dot{m}_2$: average particle mass rate at *counter 2* (kg/s)

$\dot{m}_3$: average particle mass rate at *counter 3* (kg/s)

$\dot{m}_{insert}$: insert particle mass rate (kg/s)

m_i: mass of particle i (kg)

n: fluid behavior index

$\boldsymbol{n}_{ij}$: unit normal vector between particles i and j in Lagrangian coordinate system

PTC: particle transport coefficient

p: fluid pressure (Pa)

p_{net}: net fluid pressure (Pa)

q_L: leak-off velocity (m/s)

r: distance (m)

$\boldsymbol{r}$: position vector (m)

r_{tip}: distance to fracture tip (m)

Re_0: Reynolds number

Re_p: particle Reynolds number

Re_s: slot flow Reynolds number

s: exponent

t: time (s)

$\boldsymbol{t}_{ij}$: unit tangential vector between particles i and j in Lagrangian coordinate system

tr: traction (N)

$\boldsymbol{u}_f$: fluid velocity vector (m/s)

$<u_{f\,branch}>$: average branch fluid velocity (m/s)

$<u_{f\,branch}>_0$: average branch fluid velocity at which PTC equals zero (m/s)

u_{fx}: fluid velocity in x coordinate direction (m/s)

$u_{f\,x\,max}$: maximum fluid velocity in x coordinate direction (m/s)

u_{fy}: fluid velocity in y coordinate direction (m/s)

u_{fz}: fluid velocity in z coordinate direction (m/s)

$<u_{fx}>$: average fluid velocity in x coordinate direction (m/s)

$<u_{fz}>$: average fluid velocity in z coordinate direction (m/s)

$\overrightarrow{\langle u_p \rangle}$: average proppant phase velocity vector (m/s)

$\boldsymbol{u}_p$: particle velocity vector (m/s)

$\boldsymbol{u}_{p\,point}$: velocity of a point on a particle (m/s)

$u_{p\,x}$: particle velocity in x coordinate direction (m/s)

$u_{p\,z}$: particle velocity in z coordinate direction (m/s)

$\langle u_{p\,x} \rangle$: average proppant velocity in x coordinate direction (m/s)

$\langle u_{p\,z} \rangle$: average proppant velocity in z coordinate direction (m/s)

Δu_p: relative speed (m/s)

$\left\langle \overrightarrow{\mathrm{u}_s} \right\rangle$: average slurry velocity vector (m/s)

$u_{Ganatos}$: modified Stokes' settling velocity (m/s)

$u_{Richardson\,and\,Zaki}$: settling velocity from Richardson and Zaki (1954) (m/s)

u_{Stokes}: Stokes' settling velocity (m/s)

$u_{settling}$: corrected Stokes' settling velocity (m/s)

u_*: friction velocity (m/s)

W: domain width or hydraulic fracture width (m)

W_1: main slot width (m)

W_2: branch width (m)

W_{max}: natural fracture width at mid point in height (m)

W_{nat}: maximum fracture width (m)

W_{hyd}: hydraulic fracture width at mid point in height (m)

$\boldsymbol{x}_i$: coordinates of center of gravity of particle i (m)

x_1: coordinate direction 1 in element local coordinate system (m)

x_2: coordinate direction 2 in element local coordinate system (m)

x_3: coordinate direction 3 in element local coordinate system (m)

α: stress per unit volume (Pa/m^3)

β: proportion of fluid diverted into branch

β_0: proportion of fluid diverted into branch at which *PTC* equals zero

γ: shear rate (1/s)

γ_n: normal damping coefficient (N-s/m)

γ_t: tangential damping coefficient (N-s/m)

Γ_s: particle surface

δ: overlap (m)

$\delta\Omega_{front}$: fracture front

$\delta\Omega_{perf}$: perforated interval

ζ_1: dummy variable 1

ζ_2: dummy variable 2

η: dynamic viscosity (Pa-s)

η_c: fluid consistency index (Pa-s^n)

θ: branch orientation (deg)

θ_i: angular position of particle *i* (rad)

κ : von Karman constant

μ: Newtonian viscosity (Pa-s)

ν: Poisson's ratio

ξ: scalar marker function

ρ_s: slurry density (kg/m^3)

ρ_f: fluid density (kg/m^3)

ρ_p: proppant density (kg/m^3)

σ: stress (Pa)

$\sigma_{boundary}$: boundary stress (Pa)

$\sigma_{h\ min}$: minimum horizontal stress (Pa)

$\sigma_{H\ max}$: maximum horizontal stress (Pa)

τ: deviatoric stress tensor (Pa)

Ω: domain

Ω_s: solid domain

ω: angular velocity (rad/s)

References

Altobelli, S. A., Givler, R. C. and Fukushima, E. 1991. Velocity and concentration measurements of suspensions by nuclear magnetic resonance imaging. *J. Rheol. (1978-present)* **35**: 721-734.

Asmolov, E. S. 1999. The inertial lift on a spherical particle in a plane Poiseuille flow at large channel Reynolds number. *J. Fluid Mech.* **381**: 63-87.

Beckwith, R. 2011. Proppants: Where in the World. *J. Pet. Tech.* April 36-41.

Berman, A. S. 1953. Laminar flow in channels with porous walls. *J. App. Phys.* **24**: 1232-1235.

Bird, R. B., Stewart, W. E. and Lightfoot, E. N. 2007. *Transport Phenomena*. Wiley.

Blanton, T. L. 1986. Propagation of hydraulically and dynamically induced fractures in naturally fractured reservoirs. SPE 15261, presented at the SPE/DOE unconventional gas technology symposium, Louisville, 18-21 May.

Crouch, S. L. 1976. Solution of plane elasticity problems by the displacement discontinuity method. *Int. J. Num. Meth. Eng.* **10**(2): 301-343.

Cundall, P. A. and Strack, O. D. L. 1979. A discrete numerical model for granular assemblies. *Geotechnique* **29**: 47-65.

Daneshy, A. A. 1974. Hydraulic fracture propagation in the presence of planes of weakness. SPE 4852, presented at the SPE European Spring Meeting, Amsterdam, 29-30 May.

Daneshy, A.A. 1978. Numerical Solution of Sand Transport in Hydraulic Fracturing. *J. Pet. Tech.* 132-140.

Duran, O., Andreotti, B. and Claudin, P. 2012. Numerical simulation of turbulent sediment transport, from bed load to saltation. *Phys. Fluids* **24**: 103306.

Feng, J., Hu, H. H. and Joseph, D. D. 1994. Direct simulation of initial value problems for the motion of solid bodies in a Newtonian fluid. Part 2. Couette and Poiseuille flows. *J. Fluid Mech.* **277**: 271-301.

Fortes, A. F., Joseph, D. D. and Lundgren, T. S. 1987. Nonlinear mechanics of fluidization of beds of spherical particles. *J. Fluid Mech.* **177**: 467-483.

Gallegos, T. J. and Varela, B. A. 2015. Trends in Hydraulic Fracturing Distributions and Treatment Fluids, Additives, Proppants and Water Volumes Applied to Wells Drilled in the United States from 1947 through 2010 – Data Analysis and Comparison to the Literature. United States Geological Survey Scientific Investigations Report 2014 – 5131.

Ganatos, P., Pfeffer, R. and Weinbaum, S. 1980. A strong interaction theory for the creeping motion of a sphere between plane parallel boundaries. Part 2: parallel motion. *J. Fluid Mech.* **99**: 755-783.

Goniva, C., Kloss, C., Hager, A. and Pirker, S. 2010. An open source CFD-DEM perspective. Available in *Proceedings of OpenFOAM Workshop*, June 22.

Gruesbeck, C. and Collins, R. E. 1982. Particle transport through perforations. *Soc. Pet. Eng. J.* **22**, 857-865.

Gu, H. 1987. A study of propagation of hydraulically induced fractures. Ph.D. dissertation. The University of Texas at Austin.

Hager, A., Kloss, C., Pirker, S. and Goniva, C. 2011. Efficient realization of a CFD-DEM method within an Open Source framework. Proc. Open Source International Conference 2011, Paris-Chantilly, France, November 3-4.

Hager, A., Kloss, C., Pirker, S. and Goniva, C. 2012. Parallel open source CFD-DEM for resolved particle-fluid interaction. Presented at the *Ninth International Conference on CFD in the Minerals and Process Industries*, December, 10-12.

Haynes, C. D. and Gray, K. E. 1974. Sand particle transport in perforated casing. *J. Pet. Tech.* **26**, 80-84.

Hertz, H. 1882. Ueber die beruehrung elastischer koerper (on contact between elastic bodies). English translation available in *Miscellaneous Papers*, MacMillan and Company Limited.

Ho, B. P. and Leal, L. G. 1974. Inertial migration of rigid spheres in two-dimensional unidirectional flows. *J. Fluid Mech.* **65**: 365-400.

Howard, G.C. and Fast, C.R. 1957. Optimum Fluid Characteristics for Fracture Extension. *Drilling and Production Practice* **24**, 261-270.

Hu, H. H., Joseph D. D. and Crochet, M. J. 1992. Direct simulations of fluid particle motions. *Theoret. Comput. Fluid Dynamics* **3**: 285-306.

Johnson, A. A. and Tezduyar, T. E. 1996. Simulation of multiple spheres falling in a liquid-filled tube. *Comput. Methods Appl. Mech. Engrg.* **134**: 351-373.

Johnson, A. A. and Tezduyar, T. E. 1997. 3D simulation of fluid-particle interactions with the number of particles reaching 100. *Comput. Methods Appl. Mech. Engrg.* **145**: 301-321.

Jones, R. B. 2004. Spherical particle in Poiseuille flow between planar walls. *J. Chem. Phys.* **121**: 483-500.

Jones, W. P. and Launder, B. E. 1972. The prediction of laminarization with a two-equation model of turbulence. *Int. J. Heat Mass Transfer.* **15**: 301-314.

Karnis, A., Goldsmith, H. L. and Mason, S. G. 1966. The flow of suspensions through tubes. Part 5: Inertial effects. *Can. J. Chem. Engng*. **44**: 181-193.

Kloss, C., Goniva, C., Hager, A., Amberger, S., Pirker, S. 2012. Models, algorithms and validation for opensource DEM and CFD-DEM. *Progress Comput. Fluid Dynamics, An Int. J*. **12**: 140-152.

Koch, D. L. and Hill, R. J. 2001. Inertial effects in suspension and porous-media flows. *Annu. Rev. Fluid Mech*. **33**: 619-647.

Koh, C. J., Hookham, P. and Leal, L. G. 1994. An experimental investigation of concentrated suspension flows in a rectangular channel. *J. Fluid Mech*. **266**: 1-32.

Kuriyama, K. and Mizuta, Y. 1993. Three-dimensional elastic analysis by the displacement discontinuity method with boundary division into triangular leaf elements. *Int. J. Rock Mech. Min. Sci. Geomech. Abstr*. **30**(2): 111-123.

Kossecka, E. 1971. Defects as surface distribution of double forces. *Arch. Mech*. **23**: 481-494.

Lambert, A. L., Picano, F., Breugem, W. and Brandt, L. 2013. Active suspensions in thin films: nutrient uptake and swimmer motion. *J. Fluid Mech*. **733**: 528-557.

Lamont, N. and Jessen, F. W. 1963. The effects of existing fractures in rocks on the extension of hydraulic fractures. *J. Pet. Tech*. Feb. 203-209.

Liu, Y. 2006. Settling and Hydrodynamic Retardation of Proppants in Hydraulic Fractures. PhD dissertation, The University of Texas at Austin.

Mastrojannis, E.N., Keer, L.M. and Mura, T. 1979. Stress Intensity Factor for a Plane Crack under Normal Pressure. *Int. J. Fracture* **15**, 247-258.

Maude, A. D. and Whitmore, R. L. 1958. A Generalized Theory of Sedimentation. *British J. Appl. Phys*. **9**, 477-482.

Maurin, R., Chauchat, J., Chareyre, B. and Frey, P. 2015. A minimal coupled fluid-discrete element model for bedload transport. *Phys. Fluids* **27**: 113302.

Mindlin, R. D. and Derieswicz, H. 1953. Elastic spheres in contact under varying oblique forces. *J. Appl. Mech*. **20**: 327-344.

Nolte, K.G. 1988. Fluid Flow Consideration in Hydraulic Fracturing. SPE 18537 presented at the SPE Eastern Regional Meeting, Charleston, West Virginia, 1-4 November.

Nordgren, R. P. 1972. Propagation of a vertical hydraulic fracture. SPE 3009. *Soc. Pet. Eng. J*. **12**(4): 306-314.

Olson, J. E. 2004. Predicting fracture swarms – the influence of subcritical crack growth and the crack-tip process zone on joint spacing in rock. The Initiation,

Propagation, and Arrest of Joints and Other Fractures. *Geological Society, London, Special Publications* **231**(1): 73-87.

O'Sullivan, C. and Bray, J. D. 2004. Selecting a suitable time step for discrete element simulations that use the central difference time integration scheme. *Eng. Comp.* **21**: 278-303.

Patankar, N. A., Singh, P., Joseph, D. D., Glowinski, R. and Pan, T. W. 2000. A new formulation of the distributed Lagrange multiplier / fictitious domain method for particulate flows. *Int. J. Multi. Flow* **26**: 1509-1524.

Peker, S. M. and Helvaci S. S. 2007. *Solid-Liquid Two Phase Flow*. Elsevier Science.

Pope, S. B. 2000. *Turbulent Flows*. Cambridge University Press.

Ribeiro, L.H. and Sharma, M.M. 2013. A New 3D Compositional Model for Hydraulic Fracturing with Energized Fluids. *SPE Prod. Operations* **28**, 259-267.

Richardson, J. F. and Zaki, W. N. 1954. Sedimentation and fluidization. Part 1. *Trans. Inst. Chem. Eng.* **32**: 35-53.

Rongved, L. 1957. Dislocation over a bounded plane area in an infinite solid. *J. Appl. Mech.* **24**: 252-254.

Salamon, M. D. G. 1964. Elastic analysis of displacements and stresses induced by mining of seam or roof deposits - Part IV. J. *South Africa Institute of Mining and Metallurgy* **65**: 319-338.

Segre, G. and Silberberg, A. 1962. Behavior of macroscopic rigid spheres in Poiseuille flow Part 2. Experimental results and interpretation. *J. Fluid Mech.* **14**: 136-157.

Shah, S.N. 1993. Rheological Characterization of Hydraulic Fracturing Slurries. *SPE Prod. Facilities*, May, 123-130.

Shirgaonkar, A. A., MacIver, M. A. and Patankar, N. A. 2003. A new mathematical formulation and fast algorithm for fully resolved simulation of self-propulsion. *J. Comput. Phys.* **228**: 2366-2390.

Shou, K. J. 1993. A higher order three-dimensional displacement discontinuity method with application to bonded half-space problems. Ph.D. dissertation. University of Minnesota.

Sneddon, I. N. and Elliot, H. A. 1946. The opening of a Griffith crack under internal pressure. *Quart. Appl. Math.* **IV**(3): 262-267.

Song, C., Wang, P. and Makse, H. A. 2008. A phase diagram for jammed matter. *Nature* **453**: 629-632.

Staben, M. E., Zinchenko, A. Z. and Davis, R. H. 2003. Motion of a particle between two parallel walls in low-Reynolds-number Poiseuille flow. *Phys. Fluids* **15**: 1711-1733.

Stokes, G. G. 1851. On the effect of the internal friction of fluids on the motion of pendulums. *Transactions of the Cambridge Philosophical Society* **9**: 8-106.

U.S. Energy Information Administration 2016. Crude Oil Production Data. Available online http://www.eia.gov/dnav/pet/pet_crd_crpdn_adc_mbblpd_m.htm.

U.S. Energy Information Administration 2016. Natural Gas Production Data. Available online http://www.eia.gov/dnav/ng/ng_prod_sum_a_EPG0_FGW_mmcfpd_m.htm.

U.S. Energy Information Administration 2016. Shale in the United States. Available online http://www.eia.gov/energy_in_brief/article/shale_in_the_united_states.cfm#tightoil.

U.S. Energy Information Administration 2013. Technically Recoverable Shale Oil and Shale Gas Resources. Available online https://www.eia.gov/analysis/studies/worldshalegas/archive/2013/pdf/fullreport_2013.pdf.

Versteeg, H. K. and Malalasekera, W. 1998. *An Introduction to Computational Fluid Dynamics: The Finite Volume Method*. Pearson.

Warpinski, N. R. and Teufel, L. W. 1987. Influence of geologic discontinuities on hydraulic fracture propagation. *J. Pet. Tech*. Feb. 209-220.

Weller, H. G., Tabor, G., Jasak, H. and Fureby, C. 1998. A tensorial approach to computational mechanics using object-oriented techniques. *Comp. Phys*. **12**: 620-631.

Wilcox, D. C., 1998. *Turbulence Modeling for CFD*. DCW Industries.

Wu, K. and Olson, J. E. 2014. Mechanics analysis of interaction between hydraulic and natural fractures in shale reservoirs. URTeC: 1922946, presented at the Unconventional Resources Technology Conference, Denver, Colorado, USA 25-27 August.

Yang, B. H., Wang, J., Joseph, D. D., Hu, H. H., Pan, T. W. and Glowinski, R. 2005. Migration of a sphere in tube flow. *J. Fluid Mech*. **540**: 109-131.

Zhu, H. P., Zhou, Z. Y., Yang, R. Y. and Yu, A. B. 2007. Discrete particle simulation of particulate systems: theoretical developments. *Chem. Eng. Sci*. **62**: 3378-3396.